An investigation into the electrophysiological characteristics of neurons in the *Mecp2* mosaic hippocampus

Louise Aislin Williams

BSc (Hons)

Submitted in the fulfilment of the requirements for the

Degree of Master of Science by Research

Institute of Neuroscience and Psychology

College of Medical, Veterinary and Life Sciences

University of Glasgow

Submission: March 2013

Abstract

Rett syndrome (RTT) is an X-linked neurological disorder which is caused by sporadic mutations in the gene coding for methyl-CpG-binding protein-2 (MeCP2) and which predominantly affects females (Neul *et al.*, 2010). MeCP2 is a nuclear protein that is abundant in neurons yet its exact function remains obscure. Although RTT is conventionally described as a 'neurodevelopmental' disorder there is increasing evidence that MeCP2 has more of a maintenance function (Guy *et al.*, 2011, Nguyen *et al.*, 2012). Knockout of *Mecp2* in fully adult mice results in similar symptoms to the germline RTT model even though the animals have otherwise developed normally (McGraw *et al.*, 2011, Nguyen *et al.*, 2012). In RTT females, X-chromosome inactivation leads to a MeCP2 mosaic network of cells with each cell either expressing functional MeCP2 (MeCP2+ve) or not expressing the functional protein (MeCP2-ve).

Previous studies using RTT mouse models have largely focussed on the properties of male *Mecp2*-null neurons whereas the electrophysiological properties of the female *Mecp2*$^{-/+}$ mosaic hippocampus had not been fully characterised. We aimed to assess whether the absence of MeCP2 affects intrinsic and synaptic properties of CA1 hippocampal pyramidal neurons in the context of the *Mecp2* mosaic hippocampus.

Acute hippocampal slices were prepared from *Mecp2*$^{stop/+}$ and WT mice. Whole-cell patch clamp recordings made from visually identified CA1 pyramidal cells were used to assess intrinsic cellular and synaptic properties. MeCP2 status was confirmed *post hoc* by immunocytochemistry and confocal fluorescence microscopy. A subset of mice expressing eGFP-tagged MeCP2 was also used in which eGFP indicated the MeCP2 status of recorded neurons.

Analysis of a range of active and passive electrophysiological parameters (e.g. Resting membrane potential, input resistance, membrane time constant, action potential threshold, firing rate and action potential kinetics) revealed no significant differences in intrinsic properties between MeCP2-ve and MeCP2+ve cells from heterozygous mice, or between pyramidal neurons from *Mecp2*$^{stop/+}$ and WT mice (one-way ANOVA all $P>0.05$). Similarly, no significant differences were observed with synaptic properties or short term synaptic plasticity (paired-pulse facilitation and frequency facilitation). The same was true when comparing intrinsic and synaptic grouped data (WT+ MeCP2+ve vs MeCP2-ve cells and WT vs MeCP2+ve + MeCP2-ve cells) suggesting there are no cell-autonomous or non-cell-autonomous effects in respect of the particular measured electrophysiological properties in the cohorts of mice tested.

These data suggest that lack of MeCP2 in mice which do not display any overt RTT symptoms does not affect the salient biophysical properties of individual pyramidal cells or generate significant differences in postsynaptic properties of evoked post synaptic currents in the *Mecp2* mosaic network. Clearly, the presynaptic MeCP2 status, which is unknown, will also influence responses. Given the complexity of synapses with differing combinations of pre- and postsynaptic MeCP2 status, further studies are required to address this question. In contrast to the well-characterised alterations in network long-term plasticity, the whole-cell electrophysiological properties of MeCP2+ and MeCP2- neurons had not previously been established. This study addresses that knowledge gap and provides a baseline for future investigations.

Table of Contents

List of Tables

List of Figures

Acknowledgements

My thanks to Dr Sam Booker for teaching me how to do patch clamping and immunocytochemistry. Also to Dr Rosemary Spike, Dr Shih-Min Weng, Dr Kamal Gadalla, Faye McLeod and Paul Turko for their help, support and friendship. Thanks to Dr David Hughes for help and advice on using the confocal microscope. Thanks especially to Dr Stuart Cobb for being my supervisor and for his patience and support. Thanks to Dr Mark Bailey and Prof Imre Vida for their advice, knowledge and support which has been much appreciated.
Also thanks to Prof. David Maxwell and Dr Leanne McKay for being my assessors. Finally, thanks to the Medical Research Council for funding this research.

Declaration

I hereby declare that the thesis which follows is my own composition, that it is a record of the work done by myself, except where otherwise acknowledged, and that it has not been presented in any previous application for a Higher Degree.

Louise Aislin Williams

March 2013

Abbreviations

ACSF	Artificial Cerebrospinal Fluid
AMPA	α-amino-3-hydroxy-5-methyl-4-isoxazolepropionic acid
ANOVA	Analysis of Variance
AHP	Afterhyperpolarisation
AP	Action Potential
CA1	*Cornu Ammonis* area 1
CA2	*Cornu Ammonis* area 2
CA3	*Cornu Ammonis* area 3
DAPI	4',6-diamidino-2-phenylindole
DG	Dentate Gyrus
EGTA	Ethylene Glycol Tetraacetic Acid
E/I	Excitatory/Inhibitory
EPSC	Excitatory Postsynaptic Current
EPSP	Excitatory Postsynaptic Potential
FF	Frequency Facilitation
GABA	Gamma-Aminobutyric Acid
eGFP	Enhanced Green Fluorescent Protein
HEPES	4-(2-Hydroxyethyl)-1-Piperazineethanesulfonic Acid
Het	Heterozygous
IPSC	Inhibitory Postsynaptic Current
IR-DIC	Infra-Red Differential Interference Contrast
I-V	Current-Voltage Relationship

KO	Knockout
LLP	Long Lasting Potentiation
LTD	Long Term Depression
LTP	Long Term Potentiation
MeCP2	Methyl-CpG-Binding Protein 2
NeuN	Neuronal Nuclear Antigen
NMDA	N-methyl-D-Aspartate
PB	Phosphate Buffer
PBS	Phosphate Buffered Saline
PCR	Polymerase Chain Reaction
PPF	Paired Pulse Facilitation
RMP	Resting Membrane Potential
RTT	Rett syndrome
SEM	Standard Error of the Mean
sl-m	*Stratum lacunosum-moleculare*
SNARE	Soluble NSF Attachment protein REceptor
s.o.	*Stratum oriens*
s.p.	*Stratum pyramidale*
s.r.	*Stratum radiatum*
STP	Short Term Plasticity
UV	Ultra-Violet
WT	Wild type

1 Introduction

Rett syndrome is an X-linked neurological disorder caused by mutations in *MECP2* and which predominantly affects girls since males lacking MECP2 rarely survive gestation. Females are heterozygous for *MECP2* as a consequence of X-inactivation. Rett syndrome patients initially develop normally up to 6-18 months but then suffer a regression of developmental milestones followed by stabilization. MECP2 is highly expressed in CNS neurons and is also present in most tissues. Rett syndrome symptoms vary from mild to severe and include loss of purposeful hand skills, loss of language, gait abnormalities, stereotypic hand movements, breathing abnormalities, intellectual disability, and seizures (Neul *et al*. 2010). To further understand the pathophysiology of Rett syndrome, mouse models have been created which exhibit many RTT characteristics and which have been used to study the properties of their neurons.

1.1 RTT Mice Phenotypes

Previous studies of the morphological characteristics of neurons from *Mecp2*-mutant mice have shown reduced dendritic complexity (Ballas *et al.*, 2009), higher packing density (Kishi & Macklis, 2004), reduced spine density (Fukuda *et al.*, 2005), and changes in dendritic and axonal morphology (Belichenko *et al.*, 2009b), but phenotypes are variable in RTT mouse models and across brain regions. However, intrinsic electrophysiological characteristics of presymptomatic male RTT mice have not been shown to significantly differ in comparison to WT (Dani *et al.*, 2005; Zhang *et al.*, 2008; Zhang *et al.*, 2010a; Kline *et al.*, 2010).

A common theme reported in RTT mice has been an alteration in the balance between excitatory and inhibitory circuits (E/I balance) (Dani & Nelson, 2009; Dani *et al.*, 2005; Nelson *et al.*, 2006; Chao *et al.*, 2007; Nelson *et al.*, 2011). Using optogenetic tools to selectively favour excitation of particular cell

populations, Yizhar *et al.*(2011) have recently implicated elevated E/I in the WT mouse prefrontal cortex as the cause of cellular information processing dysfunction. The dysfunction gave rise to behavioural impairment.

Loss of MeCP2 eventually leads to synaptic dysfunction which varies across brain regions and according to neurotransmitter. Extracellular recording of field excitatory postsynaptic potentials (fEPSPs) in the hippocampal CA1 region of *Mecp2*-null mice demonstrated no effect on basal excitatory synaptic transmission. However, NMDA receptor dependent LTP and LTD were significantly attenuated in symptomatic *Mecp2*-null mice compared to age-matched controls but this was not seen with presymptomatic mice. Similarly, presynaptic function (extracellular paired pulse facilitation) was significantly reduced in symptomatic animals compared to age-matched controls, but no differences seen in presymptomatic mice (Asaka *et al.*, 2006; Weng *et al.*, 2011). Early to late-symptomatic mice expressing a truncated protein (*Mecp2*$^{308/y}$) exhibited impaired learning and memory, as well as impaired synaptic plasticity (in cortical slices) (Moretti *et al.*, 2006).

That continued presence of functional MeCP2 is required for maintenance of synaptic function has been evidenced by delayed knockout of *Mecp2* in specially bred transgenic mice where floxed *Mecp2* was deleted via tamoxifen-induced recombination in adult mice (McGraw *et al.*, 2011). 10 weeks post-deletion the mice developed RTT symptoms similar to the consequence of germline KO as previously demonstrated by Guy *et al.* (2007). Thus it would appear that functional MeCP2 is necessary to maintain normality in adults irrespective of requirements of earlier developmental stages.

Extracellular and whole-cell patch recordings have revealed a reduced frequency of basal inhibitory rhythmic activity in hippocampal slices from symptomatic male *Mecp2* mutant mice compared to WT (Zhang *et al.*, 2008). Zhang *et al.* (2008) associated this property with decreased spontaneous glutamate receptor-

mediated synaptic currents in CA3 neurons. However, Zhang *et al*. (2008) observed that repetitive discharges could easily be induced, suggesting hyperexcitability.

1.2 MeCP2 Mosaicism

To date, the functional characteristics of neurons in the heterozygous female Mecp2-mosaic hippocampus have not been fully elucidated. However, a complication in the investigation of electrophysiological characteristics in females is the influence of changing estrogen levels which are likely to contribute towards variability. For example, it is known that pyramidal cell synapse formation and excitability are affected by ovarian hormones and that 17β-estradiol regulates alterations in interneuron phenotypes in the hippocampus (Nakamura & McEwen, 2005). Another potential contributor to phenotypic variability in RTT mouse models is possible non-random X-inactivation. However, different investigators at different times have yielded conflicting results in terms of skewing of MeCP2+ verses MeCP2- cells in the *Mecp2*-mosaic brain (Young & Zoghbi, 2004; Braunschweig *et al.*, 2004; Watson *et al.*, 2005; Metcalf *et al.*, 2006; Belichenko *et al.*, 2009a; Smrt *et al.*, 2011). Any skewing appears to be age-dependent (Metcalf *et al.*, 2006; Smrt *et al.*, 2011). Our own group have measured a skewing in favour of certain MeCP2+ interneurons (those expressing calbindin, calretinin and somatostatin, but not in parvalbumin-expressing cells) in the motor cortex of aged *Mecp2*$^{stop/+}$ mice, together with cell autonomous effects on interneuron morphology (Spike *et al*. 2011 - unpublished). However, the aforementioned conflicting results across different studies in respect of measuring X-inactivation ratios may arise as a consequence of applying different counting techniques or other unexplained confounding factors.

There is evidence to support cell autonomous function of MeCP2 in aminergic systems (Samaco *et al.*, 2009) and GABAergic systems (Chao *et al.*, 2010).

Conversely, non-cell autonomous effects have also been observed (Kishi & Macklis, 2010). In heterozygous females MeCP2+ neurons exhibit decreased dendritic arborization (Belichenko *et al.*, 2009b) and reduced expression of MeCP2 has been reported in MeCP2+ cells in heterozygous humans and mice (Braunschweig *et al.*, 2004). Similarly, MeCP2+ neurons express decreased tyrosine hydroxylase compared to WT in the *locus ceruleus* of heterozygous mice whilst MeCP2- neurons expressed less TH than the MeCP2+ neurons (Taneja *et al.*, 2009).

It might be expected, therefore, that differences in synaptic plasticity would be observed between MeCP2+ and MeCP2- cells in the hippocampus of heterozygous mice although any differences may only be detectable in symptomatic animals.

2 Aims of Thesis

With respect to both intrinsic and evoked synaptic properties, this thesis aims to answer the following questions:

1) Are there any detectable differences in the electrophysiological properties between MeCP2+ve and MeCP2-ve pyramidal cells in the MeCP2-mosaic hippocampus?

2) Are there any detectable differences in electrophysiological properties between pyramidal cells in the MeCP2-mosaic hippocampus and pyramidal cells in the female WT hippocampus?

The electrophysiological properties of CA1 pyramidal cells have previously been well characterised in both WT mice and also in mutant male RTT model mice. However, the corresponding properties of CA1 pyramidal cells in female RTT mice heterozygous for *Mecp2* have not previously been characterised. X-inactivation results in the mosaic expression of MeCP2 giving rise to a particular milieu where individual cells can be studied in respect of their MeCP2 status. Since functional deficits have previously been measured in cells from mutant male RTT mice (e.g. Dani *et al*. 2005; Nelson *et al*. 2006; Zhang *et al*. 2008; Asaka *et al*. 2006; Maliszewska-Cyna *et al*. 2010), it could be hypothesised that MeCP2-ve cells in heterozygous females might also exhibit functional deficits (cell autonomous effect) – either compared to MeCP2+ve cells in heterozygous females and/or in comparison to WT. Furthermore, MeCP2-ve cells could influence the properties of nearby MeCP2+ve cells (non-cell autonomous effect). However, differences between *Mecp2*-null and WT appear to arise in accordance with age of mice used and their corresponding degree of RTT symptoms.

In terms of intrinsic properties, it is hypothesized that there could be subtle changes caused by up-regulation of K^+ K_{ir}(4.1) channels and down-regulation of Nav 1.2 channels, together with effects caused by differences in cell-size, in a similar manner to that reported in *Mecp2*$^{-/y}$ locus ceruleus neurons by Zhang *et al*.(2010a).

Although Asaka *et al.* (2006) did not detect significant differences in the levels of the presynaptic proteins synaptotagmin, synaptophysin, and synaptobrevin between WT and Mecp2-mutant mice, Calfa *et al.* (2011) reported impaired synaptic vesicle density and rate of vesicle release in mutant cells. It is hypothesized that presynaptic vesicle defects in MeCP2-deficient cells could potentially result in changes to short-term plasticity and facilitation.

Using acute hippocampal slices, the aims of this study were to measure and analyse the intrinsic and evoked synaptic electrophysiological properties of identified MeCP2+ve, MeCP2-ve and WT CA1 pyramidal cells using the whole-cell patch clamp technique in both current clamp and voltage clamp modes. The research objective was to establish whether any statistically significant functional differences could be discerned between MeCP2-containing and MeCP2-deficient cells. Initially, the aim was to acquire sufficient baseline data to provide the groundwork for further study. Any such differences observed could then be related to the pathophysiology of RTT symptoms in the mouse model used, and contribute towards answering the question of whether MeCP2 deficiency affected electrophysiological properties and whether it does this in a cell autonomous or non-cell autonomous manner. It was decided to measure passive and active intrinsic properties of CA1 pyramidal cells and also their evoked synaptic properties and short-term plasticity (paired-pulse facilitation and frequency facilitation). It was appreciated that evoked synaptic properties depend on the presynaptic calcium characteristics of cells whose MeCP2 status is unknown. However, it had been intended to follow-up the evoked measurements by performing paired recordings where the presynaptic MeCP2 status could be identified. Unfortunately, this is technically challenging and was not attempted in this study.

Post hoc identification of candidate cells as pyramidal type was based on a combination of position in the CA1 pyramidal layer and morphology. The presence of MeCP2 was determined using immunostaining of fixed slices. MeCP2 protein was detected with appropriate primary and secondary antibodies, and individual recorded cells identified using biochemical staining. Immunostained cells were visualised using laser-scanning confocal microscopy. The availability of mice expressing MeCP2-eGFP fusion protein facilitated visual tracking of MeCP2 mosaicism and simplified identification of MeCP2-expressing cells. In either case, individual mice genotypes were confirmed using PCR of ear samples and this procedure was carried out independently to minimise any experimental bias.

3 Hippocampus – Essential Anatomy

This study investigated the properties of pyramidal cells in the hippocampus. WT CA1 neurons were compared to MeCP2+ve and MeCP2-ve CA1 neurons in the *Mecp2*-mosaic hippocampus. To put the study into anatomical context, a brief description of the hippocampus and its layered structure are described in this section.

In addition to numerous references in the primary literature, the structure and function of the hippocampus have been described in detail elsewhere (Andersen *et al*. 2007). However, for orientation purposes, a brief and simplified description, largely based on the above text, is given below.

The hippocampus ('hippocampal formation') is a complex 3-dimensional structure which in the rodent brain is located as shown in an MRI scan in Fig. 3-1 and a cartoon in Fig 3-2.

As can be seen in the figures, the hippocampal formations exist in both hemispheres with the hippocampi joined at the dorsal and ventral commissures. However, acute hippocampal slice preparation usually involves separating the brain hemispheres to give sets of hippocampi from each hemisphere. Fig. 3-2 visually explains the rationale behind dissecting the brain at particular angles. The remainder of this description will be limited to the cytoarchitectural structure seen in the individual acute slices.

Within a hippocampal slice there is a layered structure of major cell types and regions, the main ones of which are discussed in the next section.

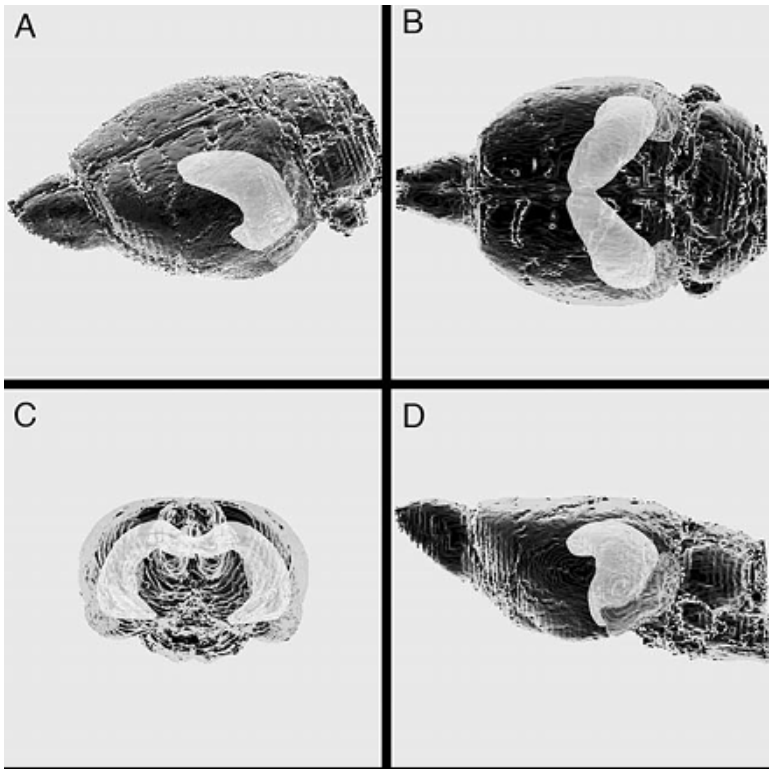

Figure 3-1 3D MRI of rat brain showing positions of hippocampi (From Andersen *et al*. 2007)

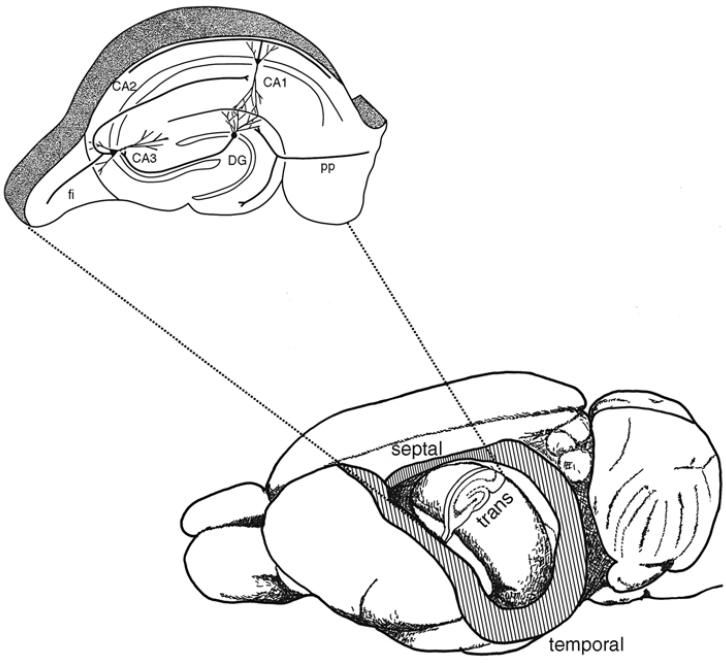

Figure 3-2 Position of hippocampal formation (in the rat) and showing a transverse hippocampal slice. DG = dentate gyrus. PP = perforant pathway. fi = fimbrium. CA1, CA2, CA3 = hippocampal regions.(From Andersen *et al*. 2007)

3.1 The Dentate Gyrus (DG)

In the transverse acute slice the DG forms an easily visible 'U'-shaped structure comprising three layers – the molecular layer, granule cell layer and the polymorphic cell layer. The granule cells are densely-packed principal cells which are the source of adult neurogenesis. Their axons form mossy fibres which synapse onto pyramidal cell dendrites in the CA3 field and these mossy fibres are the only efferent projections from the DG (Fig. 3-3). There is no direct reciprocal projection from CA3 back to the granule cells (but see Scharfman, 2007). The DG receives input from the entorhinal cortex via the perforant path which is divided into lateral and medial projections. The DG also receives inputs from the hypothalamus and brain stem.

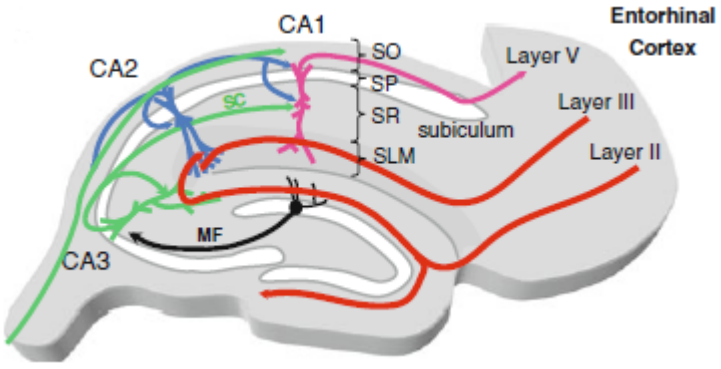

Figure 3-3 Essential anatomy of a tranverse slice through the hippocampus.

Showing pathways and regions. SC = Schaffer Collaterals; MF = Mossy Fibres. SO = stratum oriens, SP = stratum pyramidale, SR = stratum radiatum, SLM = stratum lacunosum-moleculare. Layer II, III, V – layers of the entorhinal cortex.
Adapted from Piskorowski & Chevaleyre (2012)

3.2 The CA3 Field

The CA3 is a relatively large-celled field which begins at the opening of the 'U' of the DG and comprises mostly pyramidal cells, the other principal cell type of the hippocampus. The CA3 pyramidal cells are the main input to CA1 pyramidal cells via the Schaffer collateral axons but, again, there is no reciprocal connection from CA1 to CA3.

3.3 The CA2 Field

This is a narrow zone between the distal end of CA3 and start of CA1 consisting of mostly pyramidal cells which again possess relatively large cell bodies. However, CA2 is not innervated by mossy fibres. It has been proposed that CA2 pyramidal cells form a disynaptic loop connecting input from the entorhinal cortex (EC) to CA1 pyramidal cells. Additionally, CA2 pyramidal cells exhibit a 'reversed synaptic strength rule' being strongly excited by distal dendritic EC inputs but are only weakly excited by proximal dendritic CA3 inputs (Chevaleyre & Siegelbaum, 2010).

3.4 The CA1 Field

As mentioned above, CA1 follows on from CA2 and is predominantly characterised by a pyramidal cell layer whose functional properties are the focus of this study. The CA1 pyramidal layer (*stratum pyramidale*) is relatively tightly packed compared to CA3 and CA2. Outputs from CA1 project unidirectionally into the *subiculum*. The Schaffer collateral projections from CA3 end at the border between CA1 and the *subiculum* which corresponds to a broadening out of the cell layer. The CA1 also has input from the EC via the temperoammonic pathway (Maccaferri & McBain, 1995). Although the vast majority of cells in the

pyramidal layer are pyramidal cells, a number of various types of interneuron are also found here.

The *stratum oriens* (s.o.) lies proximal to the pyramidal cell layer and is bordered by the *alveus*, a narrow region of myelinated fibres and a major route for the projection of entorhinal fibres into CA1. Fibres in the *alveus* project out of the hippocampus via the fimbria/fornix. The s.o. contains the basal dendrites of pyramidal cells together with a number of interneurons which comprise a variety of types and morphologies.

The *stratum radiatum* (s.r.) is a region immediately above the pyramidal layer in CA1/CA2. It is sparsely populated with interneurons, plus a few displaced pyramidal cells, and is the region where pyramidal cells contact the Schaffer collaterals (via their basal as well as apical dendrites). Beyond the s.r. is the *stratum lacunosum-moleculare* (s.l-m.) where apical dendrites from the pyramidal cells terminate. The s.l-m. also contains interneurons.

3.5 CA1 Pyramidal Cells

Pyramidal cells in the CA1 region of the hippocampus are the main cells of interest in this study. WT pyramidal cells have previously been comprehensively researched and described to the extent that there is a huge amount written about them in the literature.

Although the CA1 layer comprises a relatively homogenous pyramidal cell population there is nevertheless a degree of morphological and functional diversity. For example, some pyramidal neurons exhibit bifurcations in their apical dendrites and there is functional variation in terms of electrophysiological characteristics between individual CA1 pyramidal cells (Bannister & Larkman,

1995a;Spruston, 2008;Ambros-Ingerson & Holmes, 2005;Mizuseki *et al.*, 2011;Piskorowski & Chevaleyre, 2012). Many descriptive studies of CA1 pyramidal neurons have been done in the rat but the equivalent mouse cells are similar. However, clearly there are inter-species differences (Routh *et al.*, 2009) and even variability apparently caused by different genetic backgrounds within the same species (Moore *et al.*, 2011). Moreover, at least two sub-types of CA1 pyramidal cell have been identified on the basis of immunoreactivity (Szilagyi *et al.*, 2011) as well as layer-dependent firing properties (Mizuseki *et al.*, 2011). Other potential sources of variability include age and sex both of which can affect hippocampal cell properties and responses (Mori-Kawakami *et al.*, 2003;Markham *et al.*, 2005;Tombaugh *et al.*, 2005;Richwine *et al.*, 2008;Xu *et al.*, 2009). Variability is not necessarily confined directly just to neurons – a recent study has reported age-related variations in spatial distribution of astrocytes and this observation might have a secondary impact on hippocampal properties and functionality, at least in older (>=10 month) adult mice (Jinno, 2011).

In general, however, all pyramidal cells have a similar basic structure of pyramidal/ovoid-shaped soma, basal dendrites, axon, apical dendrite (which may bifurcate in the s.r.), a variable number of oblique dendrites in the s.r. and apical dendritic tuft in the s.l-m. (Fig. 3-4).

In the CA1, the main excitatory inputs arrive either proximally from CA3 via the Schaffer collaterals or distally from the entorhinal cortex via the perforant path (PP) which is also known as the temperoammonic path. Pyramidal neurons are covered with dendritic spines which are the main locations of synaptic inputs (see Fig. 3-4, inset).

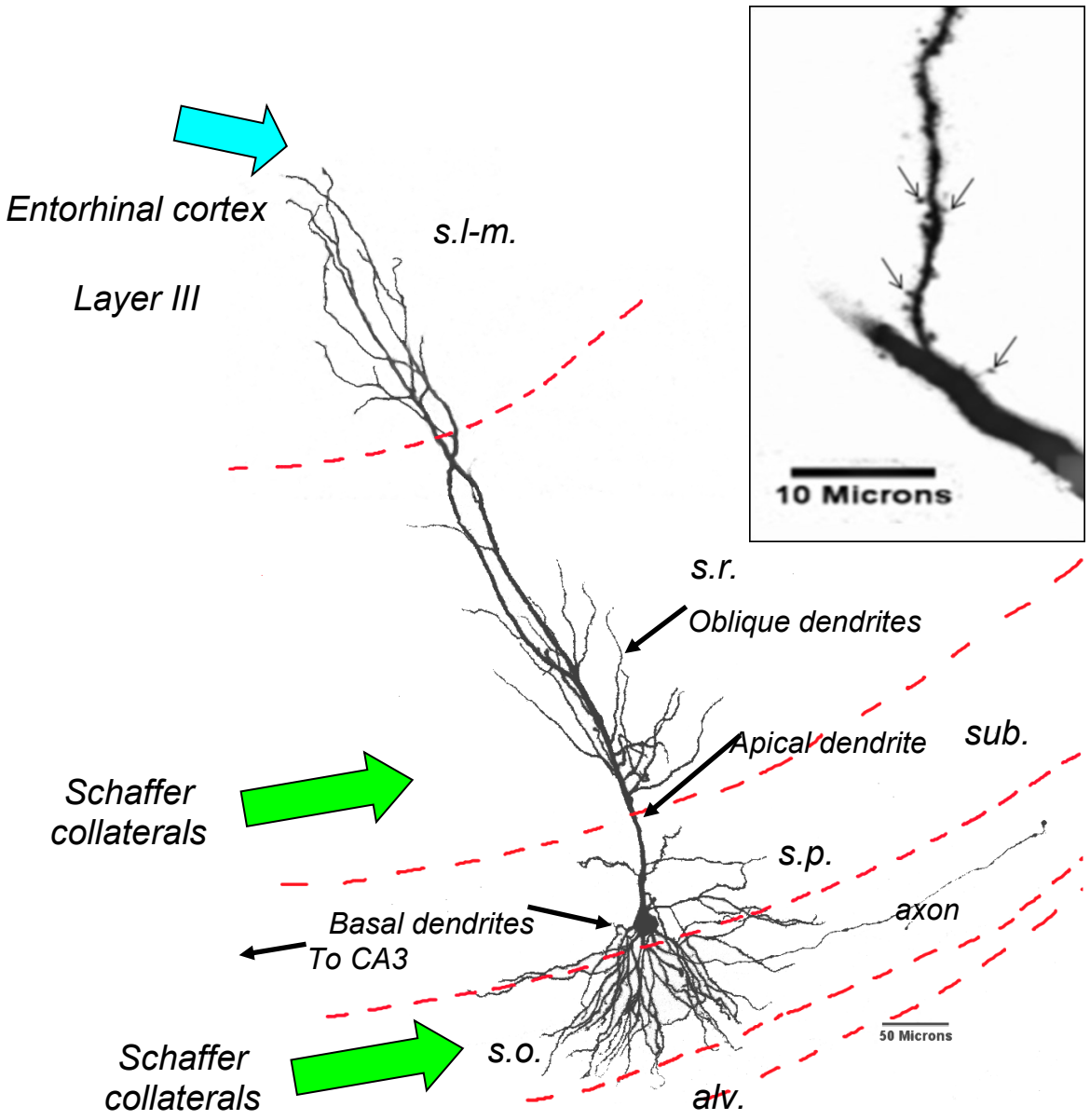

Figure 3-4 Example of a CA1 pyramidal neuron in an acute hippocampal slice from a WT mouse. The diagram shows its position in the pyramidal layer (s.p.) and the approximate locations of other hippocampal zones together with the main excitatory inputs (block arrows). The cell was recorded and filled with Biocytin. The slice was then fixed, processed and imaged in two horizontal sections on a confocal microscope using a x20 objective. Flattened confocal stacks were digitally edited to give the final image of the whole cell. Excluding the axon, the overall length of the neuron is approximately 725μm. Although only a single axon branch is shown there was another branch in the direction of CA3 but this was too faint to image reliably. Inset shows dendritic spine detail. s.l-m. = *stratum lacunosum-moleculare*, s.r. = *stratum radiatum*, s.p. = *stratum pyramidale*, s.o. = *stratum oriens*, sub. = *subiculum*. (L. Williams, 2011)

Dendritic spine distribution varies across different regions of the cell and some synapses can also be found on shafts and axon initial segments. Also spine distribution and morphology are dynamic and respond to changing stimuli, environments and circumstances, and dendritic spine changes can take place within an hour (Andersen *et al.*, 1980; Harris *et al.*, 1992; Sorra & Harris, 1993;Bannister & Larkman, 1995b; Engert & Bonhoeffer, 1999; Megias *et al.*, 2001; Konur *et al.*, 2003; Nicholson *et al.*, 2006; Katz *et al.*, 2009). The majority of spines form the locations of excitatory inputs (Megias *et al.,* 2001) but some are inhibitory receiving input from GABAergic inhibitory interneurons of which there are a number of different types. Inhibitory input mainly targets the shaft but can also target the soma, axon and dendrites. The size and number of inhibitory and excitatory synapses is normally kept in balance according to the degree of activation and where loss in number is balanced by increase in size (Bourne & Harris, 2012). Indeed, and in general, an upset in the balance between neural excitation and inhibition in the brain appears to be a marker of certain abnormal situations and disease states, including RTT (Dani *et al.*, 2005; Fernandez & Garner, 2007; Hines *et al.*, 2008; Lopantsev *et al.*, 2009; Dahlhaus *et al.*, 2010; Naylor, 2010; Yizhar *et al.*, 2011; Baroncelli *et al.*, 2011; Lewis *et al.*, 2012).

4 Electrophysiology Measurements

This section provides a background to the electrophysiological techniques used in the study together with a description of the kinds of properties and parameters that were measured.

4.1 The Patch Clamp Technique

The patch clamp technique was pioneered by Neher & Sakmann (1992) and is a methodology which enables the examination of ion channels and electrical signals in single cells. It relies on being able to form a tight seal between a pipette electrode and the cell membrane such that a very high resistance in the gigaohm range minimises leakage of the tiny currents involved. Glass pipettes containing a silver/silver chloride electrode and a conductive solution compatible with the intracellular milieu have tips with diameters of about 1μm. A variation, as used in this study, referred to as 'whole-cell patch clamp' involves rupturing the membrane whilst maintaining the gigaohm seal thus enabling the measurement of the intracellular electrical activity. It also allows the injection of current pulses and measurement of the intracellular intrinsic voltage responses. In neurons this can manifest as action potentials if the injected currents are above a depolarising threshold. Additionally, by clamping the voltage levels, the current response to neuronal signalling mechanisms can also be measured and this technique can be used to investigate single cell synaptic plasticity between presynaptic and postsynaptic connections. Voltage responses are generally in the millivolt (mV) range and current responses in the picoamp (pA) range. The technique can be applied to selected neurons in acute slices as well as to individual cells in dissociated or organotypic cultures. It can even be applied *in vivo*. However, the whole-cell patch clamp technique is technically more demanding compared to extracellular recording which is generally used to investigate network behaviour.

4.2 Passive and Active Intrinsic Properties

The use of some type of microelectrode connected to suitable electronic hardware enables the passive electrical properties of individual neurons to be ascertained. Sensitive electronic circuits combined with computer technology facilitate the detection, amplification, digitisation and recording of the tiny currents and voltages produced by single cells. Additionally, by injecting controlled hyperpolarising and depolarising current pulses into the neuron via a microelectrode, the active intrinsic responses of the cell can also be measured and recorded. Injected currents above the firing threshold of the neuron elicit action potentials. The kinetics of the action potentials can be obtained from mathematical analysis of the waveforms. These measurements allow a number of different parameters to be evaluated which, in turn, enable cells to be characterised accordingly. The characterisation of populations of normal or WT cells can provide metrics for comparison to similar populations of mutant or treated cells in order to reveal any differences. Such differences can then be investigated further, and the electrophysiological characteristics can be combined with other techniques such as immunocytochemistry plus analysis of cell morphology.

CA1 pyramidal cells have been investigated using electrophysiology by many different researchers over the years. Unfortunately, there has been no precise standard either for the reporting of electrophysiological data or for exactly how a parameter is analysed, what protocols run etc. This can make comparisons across studies rather difficult. Nevertheless, where reported, the general ranges of measured values are seen to be similar. In some cases, where there are large differences (e.g. input resistance) this may be because a different technique and/or methodology has been used to arrive at the value given. Many of the earlier twentieth century recordings used *sharp electrodes* with resistances in the region of 30-200 MΩ so those with higher values had series resistances of the same order as the input resistance of the cell which can give rise to measurement problems. Historically, experiments using sharp electrodes

reported much lower input resistances compared to those using non-sharp patch clamp electrodes. The difference has been attributed to a leakage conductance around the point of entrance of the sharp electrode (Marty & Neher, 1995 p50-51). A comparison between intrinsic properties of *Xenopus* tadpole neurons using sharp vs. whole-cell patch clamp has previously been reported (Li *et al.*, 2004). Input resistance for any kind of cell is voltage-dependent (Zaniboni *et al.*, 2005). This is because the cell membrane incorporates ion channels which result in it having the non-linear and the voltage-dependent properties of a 'leaky insulator'. The behaviour of input resistance in response to a series of hyperpolarising current pulse steps can be determined from the I-V curve generated by plotting the current values against the corresponding voltage measurements (Zaniboni *et al.*, 2005;Waters & Helmchen, 2006). Neurons typically have a relatively high input resistance, R_{in}, together with a capacitance C_m (proportional to the total surface area of the cell – including the dendrites) and the combination gives rise to a characteristic time constant, tau = R_{in} C_m. Subsequent to the formation of a gigaohm seal between the pipette tip and the cell membrane, 'breakthrough' (membrane rupture) electrically connects the internal conducting environment of the pipette with the intracellular environment of the neuron (the 'whole-cell' patch clamp configuration). The pipette itself has a resistance inversely proportional to the diameter of its tip. Additionally there is a resistance determined by the conductivity of the intracellular solution in the pipette and which varies with the intracellular solution composition (Kaczorowski *et al.*, 2007).

With breakthrough, the pipette resistance combines with intracellular elements to give an access resistance or series resistance (the electrode is in *series* with the resistance of the cell membrane relative to ground), Rs, between the inside of the cell and the chlorided silver electrode in the pipette. Rs and C_m can both give rise to measurement errors. The Rs can normally be compensated by using a bridge balance, to some extent, but never 100%. Similarly, C_m, can be somewhat compensated for but this is limited by a tendency towards instability. If oscillation suddenly takes place then large voltage fluctuations will likely cause death of the cell. Accumulation of cell debris often causes a detrimental increase in Rs during experiments. Measurement errors can be a problem

particularly in the voltage clamp configuration whence stimulus-induced changes in Rs can occur. The compensated base value of Rs is normally not a problem in current clamp since the cell is simply held at its resting membrane potential (RMP) and no current passes. But in voltage clamp the cell passes current in order to maintain its natural RMP and the amplifier will inject current to compensate. This causes a voltage to appear across the series resistance which is additive to the voltage across R_{in}. As well as requiring the compensation mentioned above, Rs also needs to be monitored for stimulus-induced changes via a test pulse to check that it doesn't go above ~30-40MΩ for voltage clamp measurements to be valid. The input resistance, R_{in}, of a pyramidal cell should normally be of the order of 100-200MΩ and can be calculated from ohm's law by injecting a preferably *small* hyperpolarising current pulse i.e. -10pA, and measuring the voltage: Rin = $V_{measured}$/10pA. Ideally, the resting input resistance is that value when no current passes but using a small amplitude current pulse is accurate enough. (See Fig. 4-1 for cell-equivalent circuit).

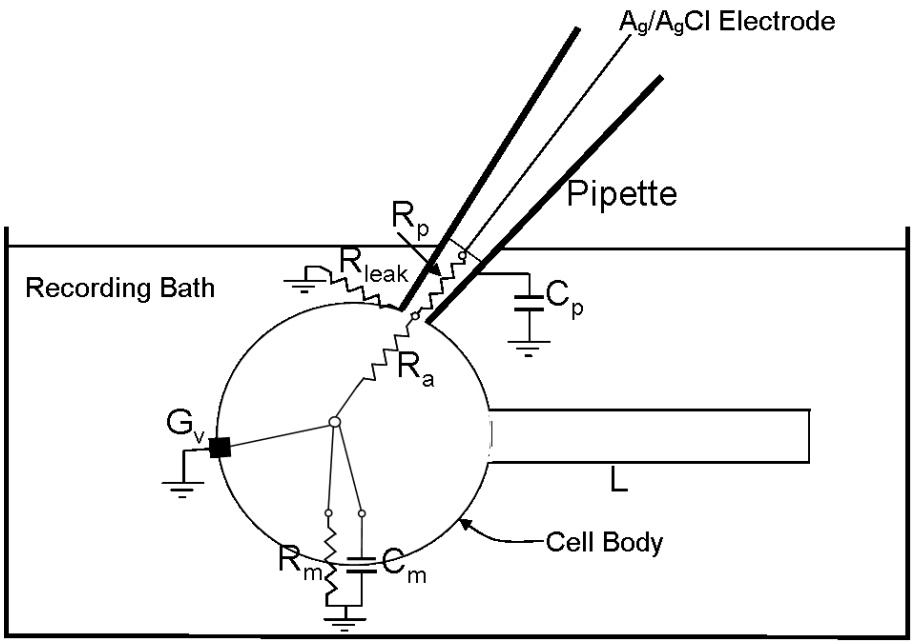

Figure 4-1 Cartoon of cell equivalent whole-cell patch clamp circuit.

L = electrotonic length of cell processes; R_p = pipette resistance; R_a = access resistance; R_{leak} = leakage resistance; R_m = membrane resistance; C_p = pipette capacitance; C_m = membrane capacitance; G_v = conductance due to voltage-dependant ion channels. (L. Williams, 2011)

Tyzio *et al*. (2003) investigated the relationships between measured values of resting membrane potential, input resistance and seal resistance of developing postnatal CA3 pyramidal cells when using whole-cell patch clamp. That study highlights the importance of a high resistance gigaohm seal since leaky seals will result in apparently depolarised membrane potential values. Tyzio *et al*. (2003) derived an equation linking the above values:

$$V'_{RMP} = V^{0}_{RMP}\frac{R_{seal} - R_{in}}{R_{seal}} + V_{seal}\frac{R_{in}}{R_{seal}}$$ … **Equation 3-1** (Adapted from Tyzio *et al*. 2003).

Where V'_{RMP} = the apparent RMP, V^{0}_{RMP} = the actual RMP, R_{seal} = the pipette seal resistance, R_{in} = the input resistance, and V_{seal} = the liquid junction potential between the solution in the pipette and the recording bath solution.

It should be apparent that R_{seal} needs to be >> R_{in}. The liquid junction potential is normally offset to null so that term can usually be ignored (as in this study) but it would be a factor in older studies which may not have had an input offset facility or where corrections were not applied. It is instructive to insert some values into the above equation. For example, assuming V^{0}_{RMP} = -65mV, R_{seal} = 10GΩ, R_{in} = 120MΩ and V_{seal} = 0mV, substituting into Equation 1 gives an apparent RMP of -64.2mV – a small affect. Changing the seal resistance down to 1 GΩ and leaving the input resistance the same, gives an apparent RMP of -57.2mV – a significant drop. Changing the seal resistance down to 500MΩ (which would be a very poor seal) reduces the apparent RMP down to only -49.4mV which would be even further reduced if the liquid junction potential was not offset. Hence to measure the RMP accurately requires a good gigaohm seal and, conversely, unexpectedly low measured RMP values may be indicative of a poor seal. It is usual for a (somewhat arbitrary) measured RMP to need to be below a cut-off value for the recorded data set to be valid and included in a study. Many

measured parameters are also temperature sensitive so it is only meaningful to compare like with like.

4.3 Measured Intrinsic Electrophysiological Parameters

The following subsections inform on the background of the passive electronic parameters that were measured in this study.

4.3.1 Resting Membrane Potential (RMP)

As described above, RMP is the potential measured after gigaohm seal formation and breakthrough into the cell. After breakthrough, the RMP can be measured and monitored during the experiment by switching to current clamp and reading the amplifier's V_m display. Subsequent current clamp recordings will generate a value for the RMP as the baseline potential at a defined section of analysed waveform. Normally a mean RMP value from multiple recordings is the value reported. Healthy pyramidal cells in acute slices have resting membrane potentials of around -60 to -70mV although cells in slices may be somewhat depolarised relative to those recorded *in vivo* (Staff *et al.*, 2000).

4.3.2 Input Resistance

The *resting* input resistance can be calculated from the steady state voltage response to a small hyperpolarising current pulse injection (-10pA) using Ohm's Law – R = V/I. An input resistance value can also be obtained from the slope of the steady state current-voltage (I-V) plot. However, the response to a -10pA pulse will cause less perturbation than the -50pA steps used to create an I-V plot.

4.3.3 Series Resistance

Also known as access resistance, this parameter is generally monitored rather than reported since it varies (usually increases) during an experiment. It is usually monitored to ensure that it stays below ~30-40MΩ for the duration of the experiment. The resistance value is the sum of the pipette resistance plus the resistance caused by the intracellular milieu. Series resistance compensation is performed prior to recording via adjustment of the bridge potentiometer on the amplifier. The value is normally less than 10MΩ at the start of an experiment but accumulation of cellular debris in the pipette tip causes it to increase. When running protocols in voltage clamp the current response to a +5mV test pulse is recorded allowing the series resistance to be calculated from Ohm's Law. The current response is visually monitored during voltage clamp experiments and the resistance can be confirmed by calculation from the mean of a number of recorded traces. For the series resistance to be less than 40MΩ the current response should not be less than 125pA. Also, it should not be seen to change by more than an allowed amount during the course of an experiment.

4.3.4 Membrane Time Constant (Tau)

The membrane time constant, tau (τ) is the time (in ms) taken for the voltage response to a small hyperpolarising current injection step to reach $\tau = 1 - 1/e$ of its final asymptotic value. This expression evaluates to ~63% of the final value. In practice, it is estimated from the rising edge of the same -10pA current pulse as used for the input resistance measurement. The measurement is done by fitting a monoexponential curve to the rising edge of the mean response to about 30 such pulses using software averaging and curve-fitting facilities. From the point of view of the cell as an electrical circuit, $\tau = R_m C_m$, where R_m = the resistance across the cell membrane and C_m is the capacitance of the cell. R_m depends on how many ion channels are open, i.e. how 'leaky' the cell is. C_m is a function of the lipid bilayer and is effectively determined by the total surface

area of the cell.

4.4 Action Potential Properties and Kinetics

The following subsections describe the active intrinsic properties that were measured in this study including the kinetic properties of action potentials.

The AP properties are measured from the voltage responses to a series of injected hyperpolarising and depolarising 500ms current pulse steps with a typical range of -250pA to +250pA and a step interval of 50pA.

4.4.1 AP Threshold

In this study, the AP threshold is the voltage relative to the baseline (which is considered as 0V in the calculations) at which the first AP is elicited on running the current step protocol. In Stimfit, base cursors are used to define a flat portion of the recording which is at RMP (the baseline) and normally located ahead of the start of the current pulse. The threshold value is determined from a point which is actually slightly above what might be the threshold as subjectively estimated by eye. The difference makes the computed threshold about 3mV higher. This is not usually a problem when comparing like with like using the same software and protocols. Stimfit computes the slope of the AP curve starting from a position marking the lower limit of the peak window set by the user (peak cursor) and takes a user-defined value for the slope. It then determines the point at which the slope is exceeded and returns this as the threshold value. In all experiments in this study the user-defined slope was set at 20mV/ms. That value essentially indicated a slope which is somewhat greater than the value of the slope at a point at where the threshold might be subjectively assigned. For example, one dataset (id 839-1, recording 10d08000.abf) gave a calculated threshold voltage of -42.8mV using a 20mV/ms slope. Halving the slope to 10mV/ms decreased the threshold to -44.2mV. Halving again to 5mV/ms gave -44.6mV and a further reduction to 3.3mV/ms gave -44.9mV. However, below a slope of 3.8mV/ms Stimfit gave false positive

threshold detections on the other hyperpolarising current injection steps (see Fig. 4-2). Clearly, the chosen slope value is a compromise since the lower values could give incorrect and false threshold values as a consequence of noise and other factors which might affect the apparent value of the slope close to the spike. With hindsight, in this study, it might have been better to have chosen a lower slope value than 20mV/ms in order to obtain a value closer to a subjectively determined value. But from the point of view of comparing values within the study it would have made little difference and the 20mV/ms slope certainly gives reproducible threshold values across different experiments (providing the AP rate of rise isn't significantly different). In any case, the AP threshold is a variable quantity and there is no true absolute value. Moreover, the measured threshold varies between AP spikes in the same recording. The first AP in a train and at the lowest current injection that elicits AP's is the one conventionally used for all AP parameter measurements since the characteristics of subsequent spikes will be modulated by the effects of previous ones. A comparison of various computational methods used to determine a measured AP threshold value has previously been investigated (Sekerli *et al.*, 2004). The biophysical origins of spike threshold variability and its relationship to modelling have recently been discussed (Platkiewicz & Brette, 2010;Platkiewicz & Brette, 2011).

4.4.2 Action Potential Amplitude

This is simply the peak amplitude of the first AP spike. In Stimfit, there is a user choice to either measure the peak relative to baseline or relative to threshold. In this study, baseline was used. Stimfit measures the peak value relative to baseline but returns the value relative to the baseline as being 0V. Stimfit also allows the user to set the number of data points for calculating the maximum value with a rolling average ('boxcar') algorithm. Hence the number of data points chosen impacts the value returned by the rolling average calculation. See Fig. 4-3 for a comparison.

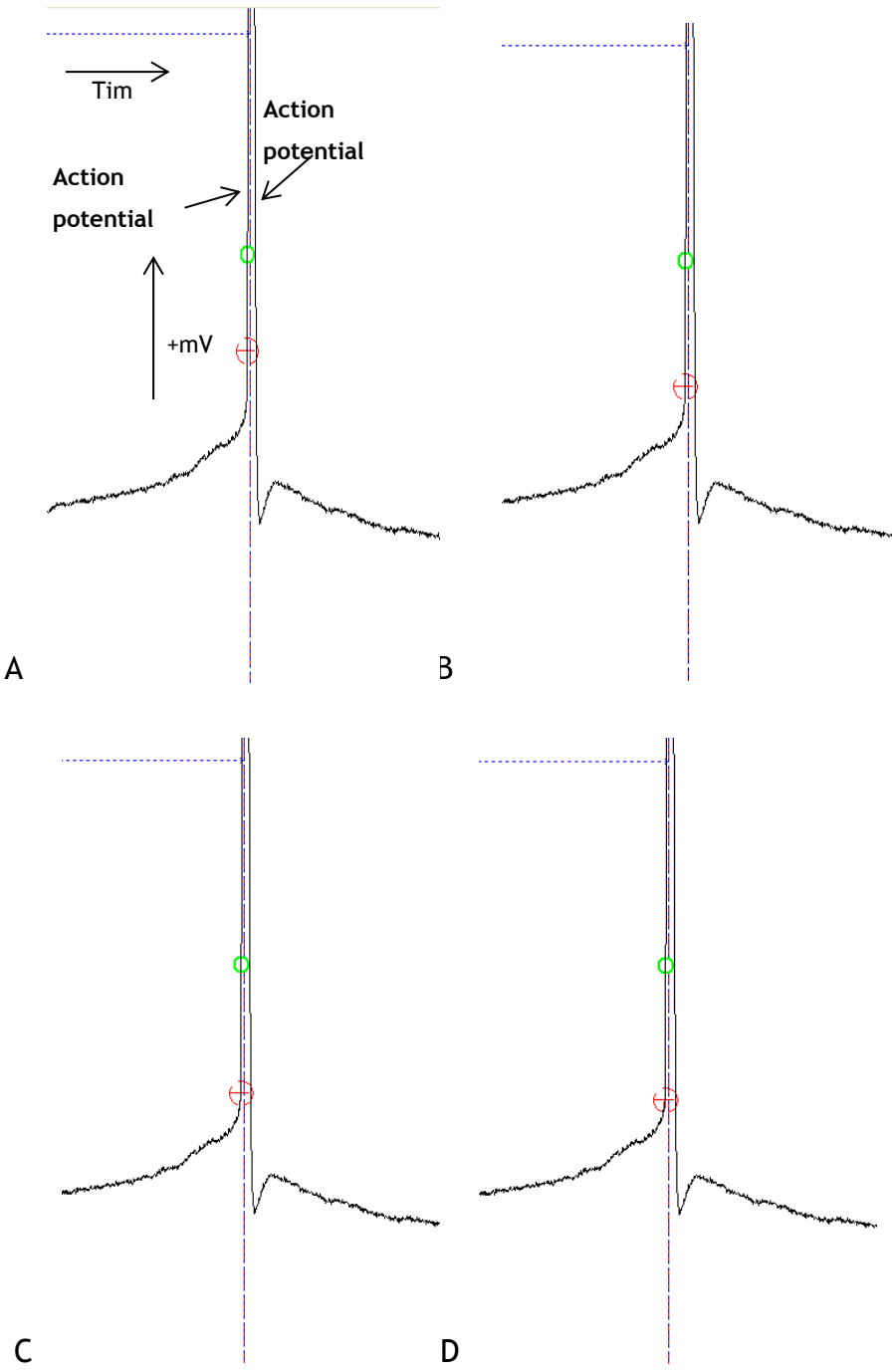

Figure 4-2 AP threshold in Stimfit. The value of calculated action potential threshold voltage values varies with user choice of slope. The Stimfit (v0.10.0) calculated threshold value is marked with a red circled crosshair. A – The default slope of 20mV/ms gives a threshold value of -42.8mV. B – At 10mV/ms the value is -44.2mV. C – At 5mV/ms the value is -44.6mV. D – At the minimum slope of 3.3mV/ms the value is -44.9mV. The green circle denotes the 20% point of the 20-80% rise time. The blue dashed line is the latency cursor. The vertical dashed line marks the position of the intersection of the calculated peak value with the x-axis.

In this study, the number of data points for amplitude calculation was set to 20. In a similar manner to threshold measurements, this is a conservative value

which returns a result significantly below a subjective choice but is robust. The number of data points could, for example, be set to 3 and this will give a close result to the subjective value but could be prone to noise errors.

4.4.3 Action Potential Duration

The duration of an action potential is generally taken as the width of the spike in ms. at half the spike's amplitude (measured relative to baseline) and is often denoted by T_{50} or $T_{1/2}$. Clearly the width measured will depend on the value determined for the amplitude. A lower apparent value for the amplitude will shift the half-amplitude position downwards and this will then return a larger apparent duration. This can be seen in the example for the amplitude determination in Fig. 4-4 where the half amplitude level is denoted by the two blue circles. The values for the spike duration are 1.016ms where the amplitude was measured as 117.01mV (3 data points), and 1.184ms for the case where the amplitude was measured as 93.82mV (20 data points). The measured duration at the lower apparent amplitude is therefore approximately 16% longer. The AP duration for the first spike at maximum current injection (+250pA) was also recorded in this study.

4.4.4 20-80% Rise Time

This is the time it takes for the action potential to reach 80% of its peak value from 20% of its peak value. The rise time can be measured either relative to the baseline or to the spike threshold. In this study, rise time was measured relative to threshold since this is more meaningful. Again, with Stimfit, the value returned will vary depending on the threshold and peak values (see Fig. 4-4). Other analysis packages, e.g. Clampfit, calculate a 10-90% rise time and this is an alternative commonly reported parameter.

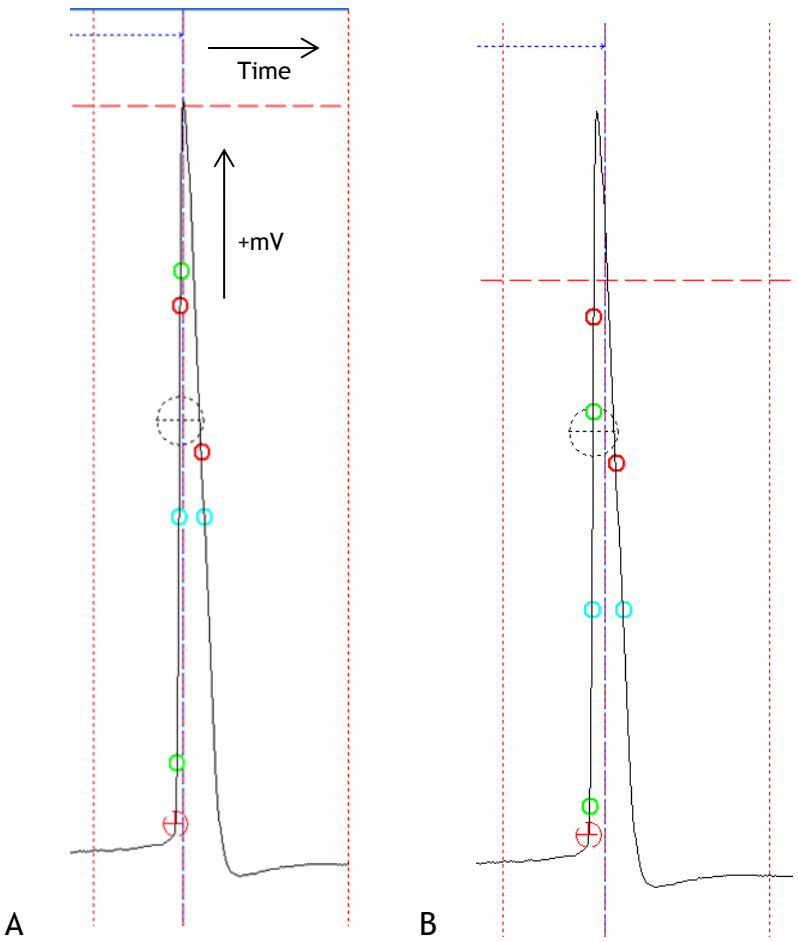

Figure 4-3 Action potential peak amplitude measurements in Stimfit. The horizontal dotted red line denotes the calculated peak amplitude. The vertical dotted red lines are the manually selected left and right peak cursors. The green circles mark the 20% of peak and 80% of peak rise time points. The red circles mark the maximum slope rise and maximum slope decay. The blue circles mark the full width at half maximum amplitude ($t_{1/2}$). The blue dotted line is the latency cursor. The vertical dashed line marks the position of the intersection of the calculated peak value with the x-axis. The red crosshair marks the position of the calculated threshold point. The large black crosshair is a manual measurement point. A - Using 3 points for the data set returns an AP amplitude of 117.01mV. B – Using 20 points returns a value of 93.82mV.

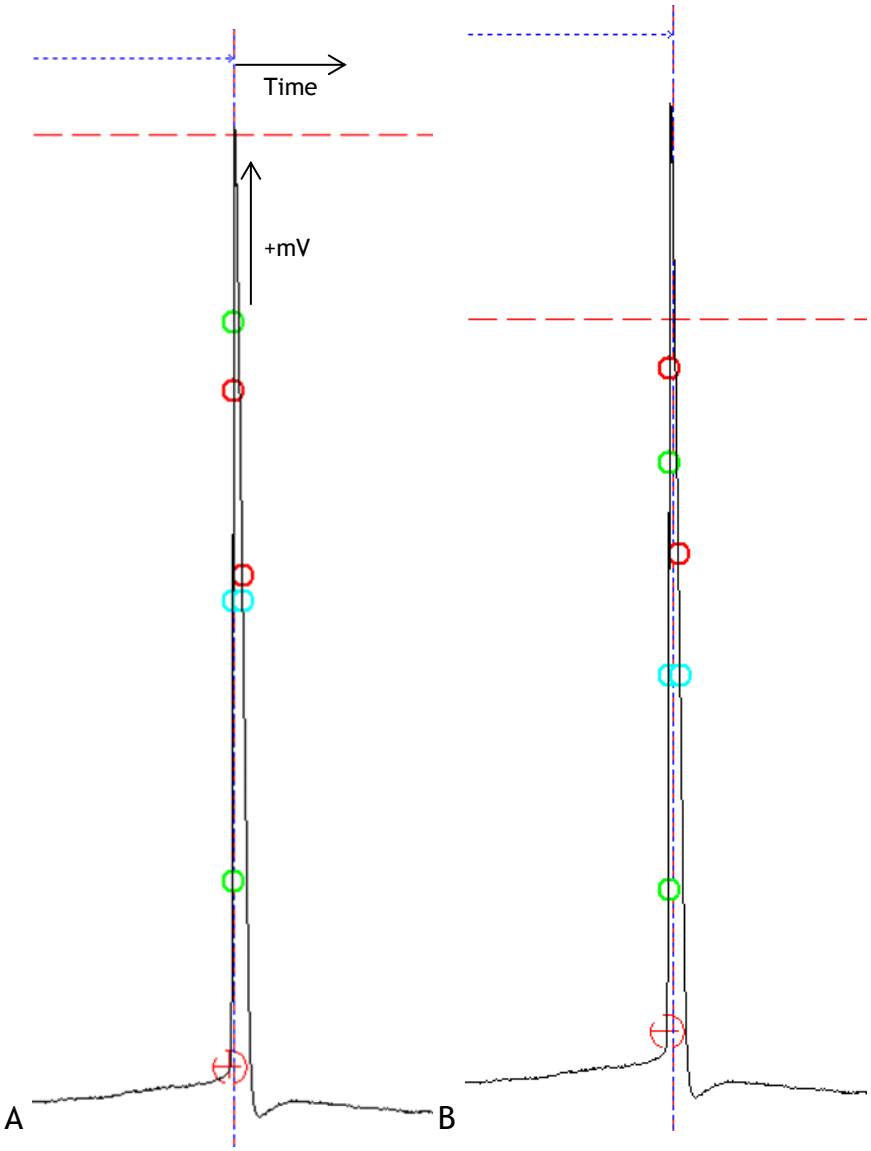

Figure 4-4 20-80% rise time measurement

Rise time measurement varies according to peak amplitude and threshold settings. The lower and upper 20-80% rise time markers are denoted by green circles. The red circles mark the maximum slope rise and maximum slope decay. The blue circles mark the full width at half maximum amplitude ($t_{1/2}$). The blue dotted line is the latency cursor. The vertical dashed line marks the position of the intersection of the calculated peak value with the x-axis. The red crosshair marks the position of the calculated threshold point. A - The rise time is calculated by Stimfit as 0.117ms using a 5mV/ms threshold slope and 3 data points to calculate the peak amplitude. B – The rise time is calculated as 0.099ms using a 20mV/ms threshold slope and 20 data points to calculate the peak amplitude.

4.4.5 Action Potential Maximum Rate of Rise and Rate of Decay

These are the respective values in mV/ms returned for the maximum slope on the rising phase and decaying phase of the spike waveform. They are both instantaneous values and neither parameter depends on the measured threshold or peak amplitude. The calculated positions of the maximum rise slope and maximum decay slope are denoted by red circles on the Stimfit figures.

4.4.6 Action Potential Firing Rate

Stimfit calculates the number of threshold crossings, and hence the number of Action Potential spikes, that occur within each 500ms current pulse step i.e. between -250pA and +250pA with 50pA steps, in this study. Obviously APs only occur above the spike threshold. The number of crossings/AP's can be plotted against current step. Using an injected current pulse width of 500ms, multiplying the number of crossings by 2 gives the number/sec. i.e. the AP spike frequency in Hz.

4.4.7 After-Hyperpolarisation Amplitude

After-hyperpolarisations (AHP's) often occur and immediately after the action potential spike. AHP's can limit the firing rate of a cell thus controlling or modulating excitability. In some cell types, such as CA1 pyramidal neurons, AHP's are also responsible for controlling spike frequency adaption. Measured values have been shown to vary according to genetic background (Moore *et al*. 2011). The magnitude of the AHP has an impact on learning and memory and also varies with age (Matthews *et al.*, 2009). AHP's are mediated by outward going potassium currents. They are characterised and distinguished by a number of different components (fast, medium and slow) according to temporal duration, kinetics, and pharmacological response but not all components are

necessarily observed. The different AHP's are mediated by different sets of Ca^{2+}-activated K^+ channels (Sah & Bekkers, 1996). Fast AHP's (fAHP's) have a short duration of perhaps 5-10ms (Fig. 4-5, B), can occur after a single AP and exhibit a characteristic negative spike appearance (Fig. 4-5, A and B). fAHP's are sometimes referred to as peak AHP's (pAHP). In contrast, medium AHP lasts for some 10-100's of milliseconds (Fig. 4-5, A and C) and is blocked by apamin (in bee venom). Slow AHP (sAHP) only occurs after spike trains and has duration in the seconds range. It is not generally observed with the 500ms pulses in current-clamp protocols used in this study.

Reduction in medium AHP (mAHP) has been linked to susceptibility to seizures and this reduction is apparently a consequence of down-regulation of small conductance Ca^{2+}-activated K^+ channels (SK channels), at least in the CA1 pyramidal cells from pilocarpine treated animals (Schulz *et al.*, 2012). They noted that there has been some controversy about whether SK channels mediate mAHP. Tzingounis *et al.* (2010), reported that a component of mAHP (and sAHP) in CA3 pyramidal neurons is mediated by KCNQ5 voltage-gated K^+ channels but loss of KCNQ5 has little effect on CA1 pyramidal cells. The details of mediation of AHP's according to channel-type is clearly complex and cell-type dependent.

Fast AHP's have been shown to reduce with learning but not ageing (Matthews *et al.*, 2009). The fAHP is mediated by large conductance, voltage-dependent BK channels and controls high frequency firing as well as early spike adaption (Storm, 1987; Gu *et al.*, 2007).

As can be seen in Fig. 4-6, the fAHP associated with the first spike has greater amplitude compared to subsequent fAHP's. In Stimfit the amplitude of AHP's is measured relative to threshold and is detected as a negative-going peak within the region manually set by the peak cursors. Hence the caveats mentioned previously in relation to the measurement of the spike threshold value apply to

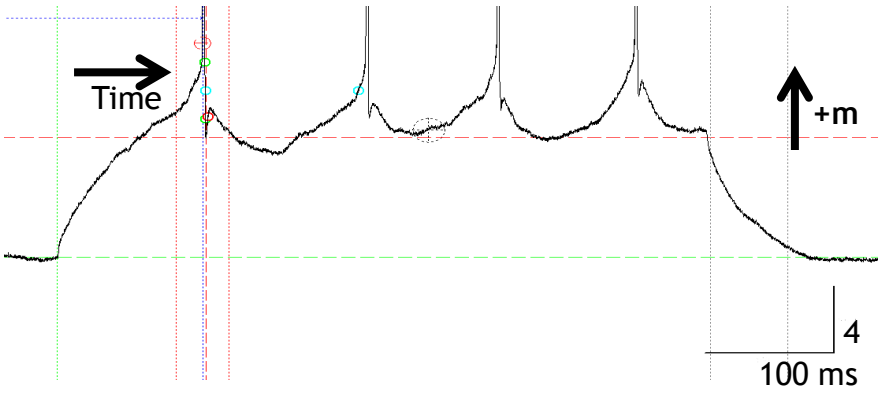

A

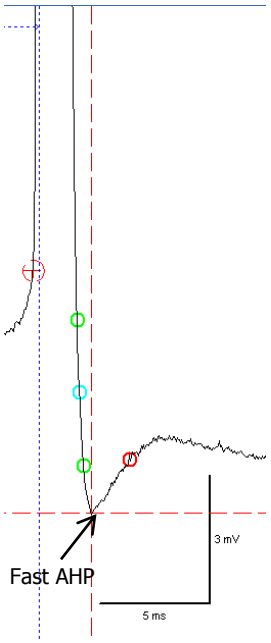

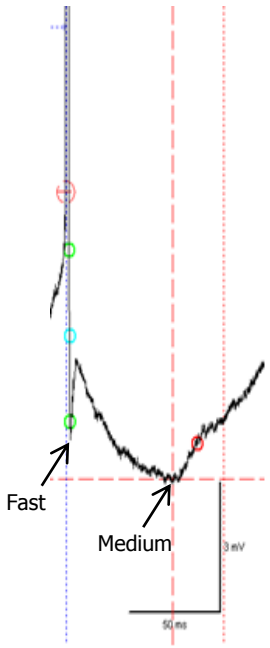

B C

Figure 4-5 The occurrence and appearance of a fast AHP. fAHPs occur immediately after the AP spike, followed by a medium AHP. **A** - The fAHP peak amplitude of the first spike is denoted by the red, horizontal dashed line intersecting with the red, vertical dashed line. Note how subsequent fAHP's exhibit reduced amplitude relative to the first. This is the same example trace as used in the previous examples and reflects a 500ms current pulse at +50pA. **B** – fAHP's have a short duration, less than 5ms in this case. **C** – mAHP's have duration of the order of 10's-100's of milliseconds. The vertical red dotted line is the right-hand peak cursor. The vertical blue dotted line marks the intersection of the latency cursor with the x-axis. The horizontal blue dotted line is the latency cursor. The vertical red dotted lines are the right and left peak cursors. The red vertical dashed line is the intersection of the peak value with the x-axis. The horizontal green dashed line marks the position of the baseline. The vertical green dotted line marks the position of the right-hand base cursor. Coloured circles and crosshair are as previously described.

subsequent AHP measurement. In the example cell, apart from the first spike AHP, the other fAHP's reduce and disappear at greater current steps but the first spike fAHP in the train remains and even increases in amplitude (Fig. 4-6).

4.5 I-V Relationship

Plotting the voltage responses to a series of hyperpolarising current steps injected via an intrinsic protocol returns the current-voltage (I-V) relationship, characteristic of the cell-type. From the recording two sets of voltage response data are analysed and plotted – the peak values and the steady state values (Fig. 4-7). The initial values at the beginning of the 500ms response are characterised by a 'sag' caused by a hyperpolarising-activated and inwardly-rectifying, non-specific cation current, I_h. The I_h is a controller of excitability in CA1 pyramidal cells (Maccaferri *et al.*, 1993) and it has recently been suggested that I_h could help counter excitotoxicity after brain trauma (Deng & Xu, 2011). The same inward rectification mechanism appears to be involved in the inhibition of CA1 pyramidal cells by at least some interneurons (Peng *et al.*, 2011) and also in the temporal precision of coincidence detection (Pavlov *et al.*, 2011).

The peak voltage values are derived from the 20-point rolling boxcar average of the section delineated by the Stimfit peak cursors shown in Fig. 4-7. The steady-state voltage values are similarly acquired from the last ~100ms of the recording, but averaging all points of the data. Normally at least 3 sets of voltage responses are used to generate mean values which are then plotted on a graph.

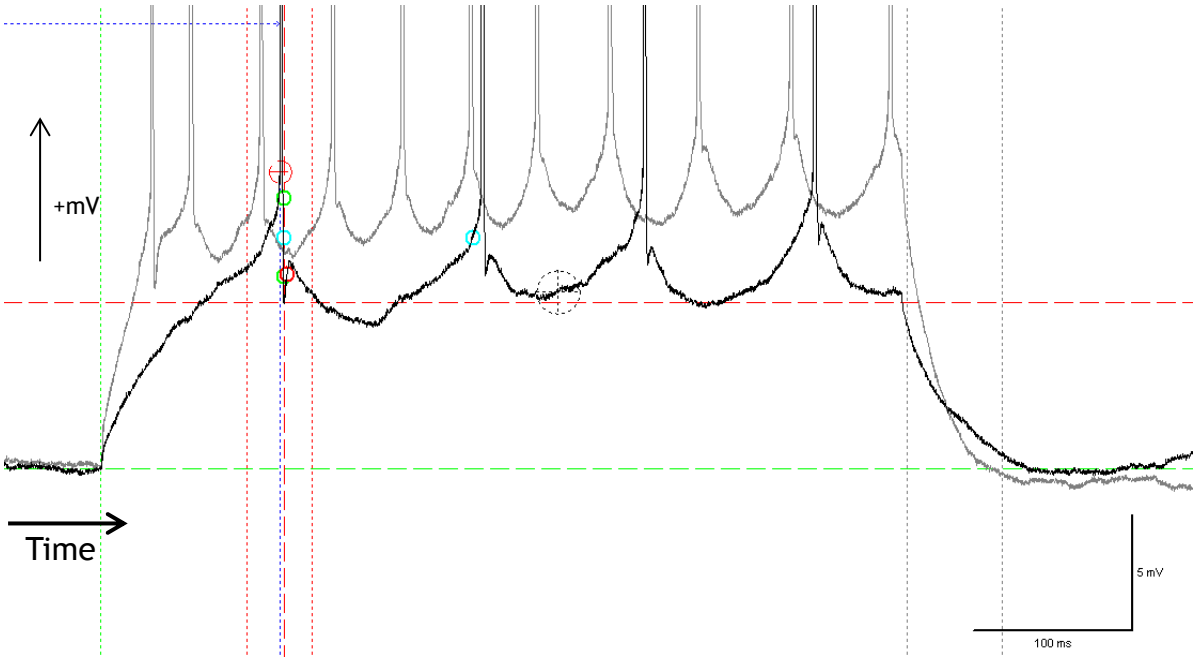

Figure 4-6 Effect of increasing current step to +100pA on AHP appearance and amplitude. The first fAHP at 100pA (grey trace) is markedly greater in amplitude compared to the trace at 50pA (black trace). However, concomitant to an increase in AP frequency, the other spikes elicited at 100pA exhibit a much reduced fAHP or even absent fAHP. Note how AP latency also decreases with increasing current injection. Coloured circles, crosshair, horizontal and vertical lines generated by Stimfit are as previously described.

4.6 Synaptic Properties of Pyramidal Cells

Stimulation of cells in the CA1 pyramidal layer orthodromically (CA3 -> CA1) via the Schaffer Collaterals evokes postsynaptic responses which can be recorded and measured using whole-cell patch clamp. In this case voltage clamp is used to hold the cell at -65mV, the approximate resting potential, and stimuli are applied via an external stimulator with an electrode located in the s.r. By employing an appropriate stimulation protocol, the somatic current response (Excitatory PostSynaptic Current – EPSC) of the cell can then be recorded.

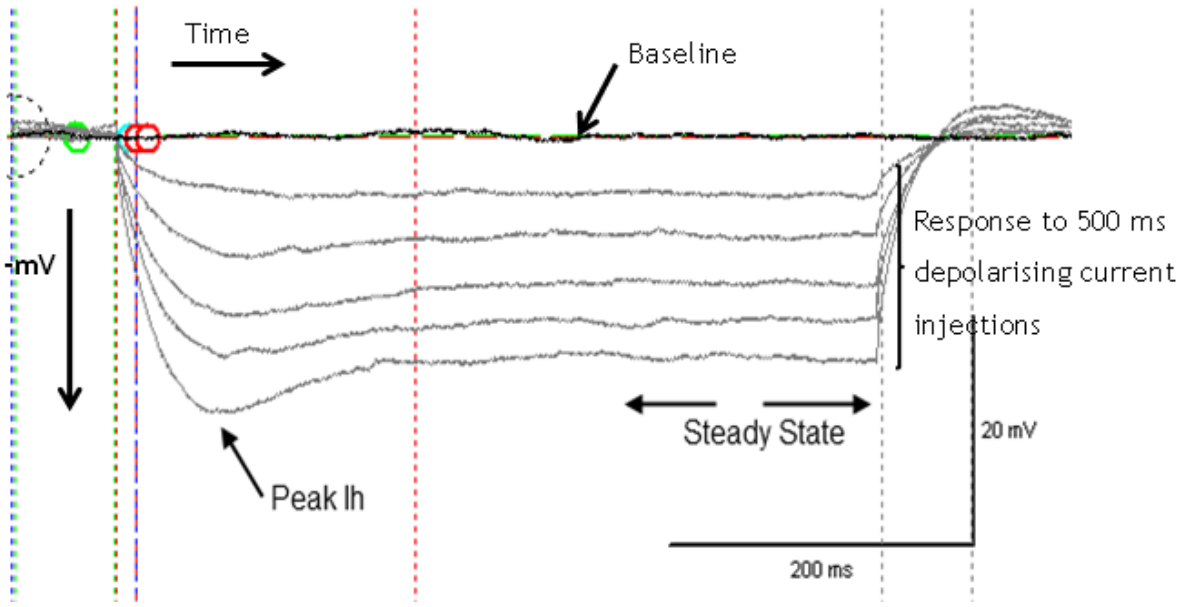

Figure 4-7 Response of CA1 pyramidal cell to current injection steps.

An injection of a series of hyperpolarising current injection steps (-250pA to 0pA, 50pA steps) showing the characteristic 'sag' at the beginning of the response followed by a 'steady state'. Coloured circles, crosshairs, horizontal and vertical lines generated by Stimfit are as previously described.

However, to obtain a purely excitatory response GABAergic inhibition needs to be blocked using appropriate concentrations of an antagonist in the bath solution e.g. bicuculline which acts on $GABA_A$ receptors. The combination of inputs from inhibitory (GABAergic) and excitatory (glutamatergic) receptors is complex.

Gasparini & Magee (2006) found that CA1 pyramidal cells have two different modes of response to synaptic input, and output from each branch is globally summed and output axonally. The mode depended on whether input was less synchronous/spatially distributed (linear integration mode), else synchronous and spatially clustered (non-linear integration mode). In the case of the former, AP output rate and timing varied linearly according to a function of the input whereas the latter produced a non-linear integration that was precisely controlled. Inputs have also been shown to contribute directly to dendritic spike

output (Katz *et al.* 2009). Dendritic spikes are voltage spike events that are generated locally in dendrites. Dendritic spikes can control whether dendritic branches are able to generate somatic AP's (Remy *et al.*, 2009).

'Synaptic plasticity' is a term used to describe the ability of synapses to change their strength in an activity-dependent manner. Such changes can be short-lived (milliseconds to seconds) – short-term plasticity (STP), or longer lasting (minutes to hours and beyond) – long-term plasticity (LTP). LTP is mostly, but not exclusively, used for describing the synaptic properties of the *network* i.e. from an extracellular standpoint. STP can be observed in the network and also, as in this study, can be observed in single neurons. (Rotman *et al.*, 2011) recently proposed that STP could function to optimise information transfer.

One observable property of STP is the phenomenon of facilitation which relates to an increased probability of neurotransmitter release after stimulation where that probability was initially <1 (Fioravante & Regehr, 2011). Hence the subsequent response is greater in amplitude than the first. The mechanism of facilitation involves Ca^{2+} although the precise details are uncertain. In their review Fioravante and Regehr, two hypotheses for facilitation are suggested. One is by the persistence of residual presynaptic Ca^{2+}, the other involves presynaptic calcium-binding proteins that limit the first response which, presumably once the binding proteins are saturated, enables more Ca^{2+} to be released. An increase in Ca^{2+} influx could mediate facilitation by raising the release probability (Zucker & Regehr, 2002). This is supported by the consequence of mutating particular calcium sensor proteins which results in reduced facilitation (Mochida *et al.*, 2008).

The converse of facilitation – depression – can also occur, leading to a second response being reduced compared to the previous one. Paired-pulse facilitation is a common way to measure STP and involves two stimulus pulses separated by a short time delay. The delay can be between 25ms and 500ms, or even up to a

second. The degree of facilitation is measured by calculating the ratio of the peak amplitudes of the 2nd to the first (conditioning) pulse on an averaged set of data for a particular cell (Fig. 4-8). In the case of measurement at the cellular level, e.g. patch clamp, the facilitation reflects the calcium dynamics of the upstream presynaptic cell rather than the downstream postsynaptic cell in which the effects are detected.

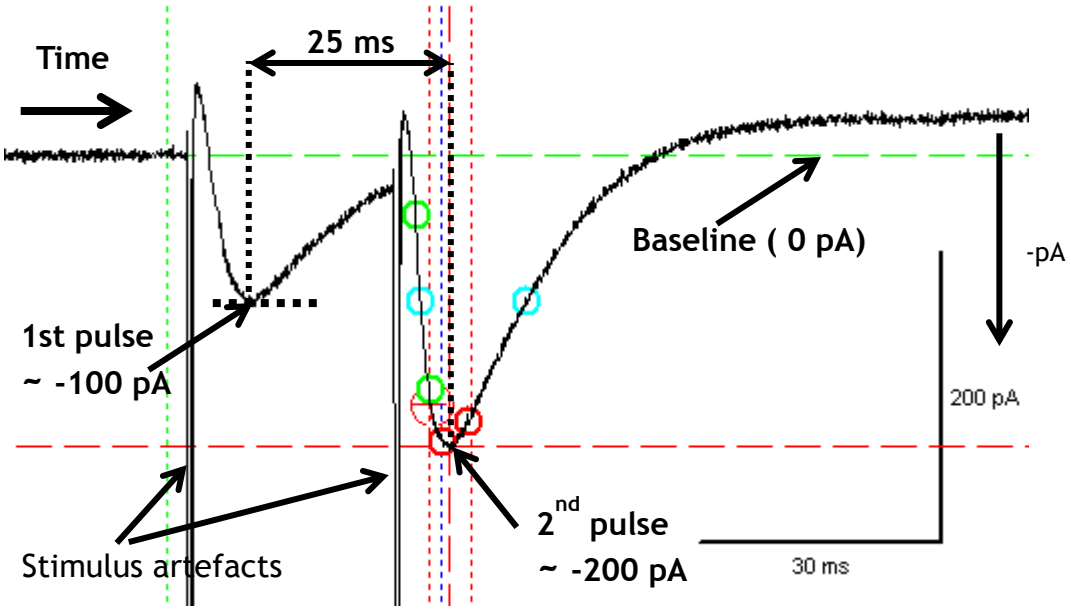

Figure 4-8 Example of paired-pulse facilitation. Data was obtained from the same WT cell used in previous examples. The diagram shows negative-going current responses to two external stimuli separated by a 25ms inter-stimulus interval. The trace shown was the average of 10 recordings with a 10 second interval between the recording of each trace. The negative-going peak of the first response is indicated by the annotated horizontal black dotted line. The peak of the second response is indicated by the Stimfit-generated horizontal red dashed line. Relative to baseline (0 pA), the second response had an amplitude of -200pA compared to -100pA for the first pulse response. Thus the paired-pulse ratio was -200/-100 = 2. Coloured circles, crosshairs, horizontal and vertical lines generated by Stimfit are as previously described.

The PPF ratio tends to decrease with increasing paired-pulse stimulation interval (Fig. 4-9 A, B and C) and the ratio is usually only ~1 at intervals of 500ms or greater. However, the ratio at 50ms interval is often (but not always) greater than at 25ms. The PPF ratio can be plotted against interval.

At the same time as measuring the peak amplitudes, the 20-80% rise time, $T_{1/2}$, and decay time constant can acquired for each peak. A data set for a number of different cells from different animals can be compiled to enable comparison between WT and mutant cells.

An extension of paired-pulse facilitation is frequency facilitation whereby the cell's response to a series of presynaptic stimuli at different frequencies is measured. In this study a train of 10 stimulus pulses at each of 5, 10, 20 and 40Hz were applied, again in voltage clamp and via the Schaffer collaterals. A series of stimuli can generate a build-up of facilitation as each pulse in a train facilitates the next (Zucker & Regehr, 2002). Klemmer *et al.* (2011) have used both PPF and a similar frequency facilitation protocol in the comparison between WT and *Fmr1* (the gene for fragile X mental retardation protein) KO mice. Interestingly, they observed a difference with subsets of both the PPF responses and the frequency facilitation responses between their WT and mutant mice.

Both facilitation and synaptic responses generally, involve mediation by two main types of excitatory (glutamatergic) receptors: α-amino-3-hydroxy-5-methyl-4-isoxazolepropionic acid (AMPA) and N-methyl-D-aspartate (NMDA) receptors. These can be differentially isolated pharmacologically and it has been demonstrated that both types of receptor contribute towards facilitation (Clark *et al.*, 1994).

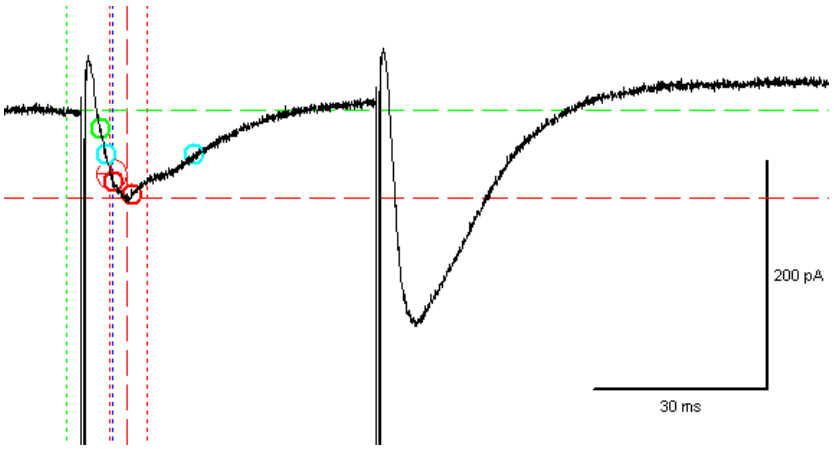

A

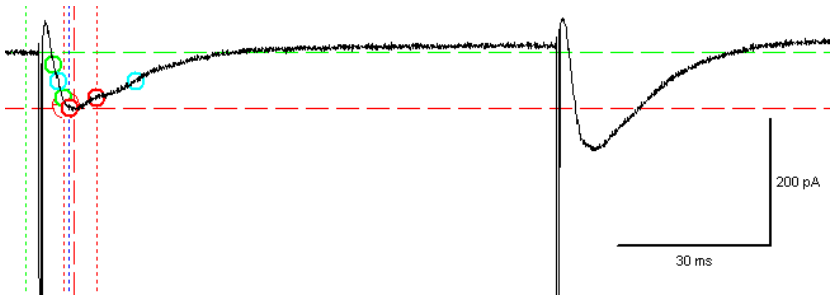

B

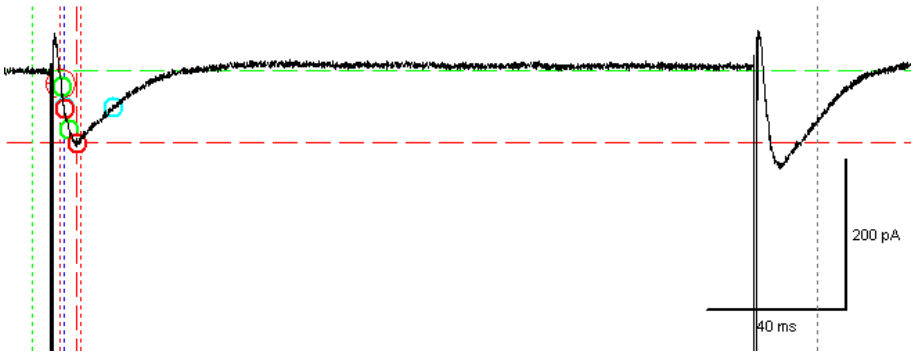

C

Figure 4-9 Facilitation generally decreases with increasing paired-pulse stimulation interval. The details of the traces are as described in Figure 4-8 but with different inter-stimulus intervals and current response amplitudes. Intervals are A – 50ms, B – 100ms and C – 200ms. Coloured circles, crosshairs, horizontal and vertical lines generated by Stimfit are as previously described.

5 MeCP2 – Background and Previous Research

This section reviews selected literature related to the general study of MeCP2.

5.1 MeCP2 and Rett Syndrome

A number of different types of mutation in the gene that encodes methyl-CpG-binding protein 2 were first identified as the cause of at least some cases of Rett syndrome by Amir *et al.* (1999). *MECP2* is located at Xq28 (Vilain *et al.*, 1996) and the protein had previously been isolated and purified from rat brain (Lewis *et al.*, 1992). Lewis *et al.* (1992) performed peptide sequencing of the protein and nucleic acid sequencing of the cDNA. They demonstrated that MeCP2 was highly abundant in the brain, preferentially binds to methylated CpGs, and is predominantly colocalised with pericentromeric heterochromatin. They also identified motifs from the deduced amino acid sequence and suggested the protein could have a transcriptional repressor role and also, because of its abundance, be involved in chromatin structure and nuclease resistance. MeCP2 is not confined to the brain/CNS and is widespread across somatic tissues, but with varying levels (Meehan *et al.*, 1992; Shahbazian *et al.*, 2002b). MeCP2 protein levels do not necessarily correlate with RNA expression. MeCP2 protein levels vary across brain regions and levels increase along with neuronal maturation (Shahbazian *et al.*, 2002b).

5.2 MeCP2 Overexpression

Whereas Rett syndrome is a consequence of loss of MeCP2 function a condition named *MECP2* Duplication syndrome has also been identified and which affects males whilst although females can also be slightly affected, they are generally asymptomatic carriers. The increased *MECP2* dosage leads to severe intellectual disability. Other characteristics can include autistic features, infantile hypotonia, spasticity, epilepsy, absence of speech, problems with walking, recurrent infections, facial dysmorphism, and other problems (Van Esch 2012).

Early death is common. Mouse models have been developed and one in which MeCP2 overexpression is restricted to neurons shows motor deficits and impaired learning and memory. The deficits were accompanied by attenuated LTP and extracellular PPF (at certain interstimulus intervals) in hippocampal slices. Increased frequencies of mEPSCs were also observed (Na *et al*. 2012).

Clearly MeCP2 is important for normal brain function and its levels of expression need to be maintained within certain limits.

5.3 MeCP2 in Astroglia and Microglia

Until quite recently MeCP2 was not thought to be present in glia but has now been shown to be expressed in glial cells, including astrocytes (Ballas *et al.*, 2009; Maezawa *et al.*, 2009) and expression in astrocytes has been confirmed with cells expressing eGFP-tagged MeCP2 (Kifayathullah *et al.*, 2010; Smrt *et al.*, 2011). With the exception of microglia, other glial cells and neurons have common origins. Microglia, however, are CNS macrophages which have their origins in embryonic yolk sac primitive macrophages (Ginhoux *et al.*, 2010). The earlier belief that MeCP2 was not expressed in astrocytes meant that this important cell type had been largely ignored in investigations of RTT pathophysiology. Ballas *et al*. (2009) reported that *Mecp2*-null astrocytes and derived astrocyte-conditioned media (ACM) exhibited a negative effect on dendritic morphology of cultured WT neurons and, conversely, WT ACM appeared to have a normalising effect on *Mecp2*-null neurons *in vitro*. Maezawa *et al*. (2009) also reported that after several weeks in culture astrocytes heterozygous for MeCP2 expressed much lower levels of MeCP2 than expected. The authors suggested this was a result of the spread of the deficient state i.e. via a non-cell autonomous influence of mutant astrocytes. They proposed that the non-cell autonomous influence could in part spread via gap junctions and that such effects were more pronounced in astrocytes than in heterozygous neurons. Additionally, they found that MeCP2-deficient astrocytes were functionally abnormal in terms of regulation of brain-derived neurotrophic factor (BDNF), pro-inflammatory cytokines and mitogen-activated protein kinases (MAPK).

However, an experiment with mutant astrocyte-conditioned media purely from astrocytes by Maezawa *et al*. (2009) did *not* show any reduction of MeCP2 expression in WT astrocytes, although their comparison was limited to a 48-hour incubation.

In a follow-up paper, (Maezawa & Jin, 2010) investigated the contribution of microglia and found that conditioned media from MeCP2-deficient microglia was toxic to dendrites and identified the factor as glutamate and the cause as excessive glutamate release. Lintas *et al*. (2012) have investigated genome-wide studies across Down's syndrome, Autism and Rett syndrome, and reported convergent relationships with 37 genes in common. They highlighted a shared dysregulation of immune response together with microglial activation and excessive glutamate release. Through the generation of WT microglia via bone marrow transplants, Derecki *et al*. (2013) have demonstrated symptom improvement in both *Mecp2*-null and *Mecp2*$^{+/-}$ female mice. The authors suggested an observed reduction in phagocytic function in Mecp2-deficient microglia could play a role in RTT pathophysiology.

Smrt *et al*. (2011) reported a lower than expected proportion of eGFP-expressing GFAP-positive astrocytes (18.84%) and S100β-positive astrocytes (<30%) compared to NeuN-positive cells (~50%) in the DG of heterozygous TgGFPX$^{+/-}$ mice but that observation has not been linked to Ballas *et al*.'s (2009) or Maezawa *et al*.'s (2009) findings. Astrocytes are an important regulator of glutamate homeostasis and normally protect neurons from glutamate toxicity (Brown, 1999) but it is not inconceivable that excessive glutamate produced by MeCP2-deficient glial cells could disrupt the normal function of astrocytes and even be toxic to them.

A potential pharmacological intervention for glutamate toxicity using the naturally-occurring pentacyclic triterpene, maslinic acid, which enhances glutamate clearance by astrocytes, is suggested by studies carried out by (Qian *et al*., 2011). It would be interesting to conduct *in vivo* trials with maslinic acid

on heterozygous RTT mice to see if any improvements in some or any RTT symptoms could be observed. Guan *et al.* (2011) recently demonstrated a reduction in focal cerebral ischaemia damage in diabetic-induced rats pre-treated intra-gastrically with maslinic acid. They determined that the neuroprotective mechanism involved glutamate clearance.

The role of glia in RTT pathophysiology is further evidenced by recent experiments involving rescue of MeCP2 in astrocytes from globally MeCP2-deficient mice (Lioy *et al.*, 2011). The re-expression of MeCP2 limited to astrocytes alone appeared to ameliorate RTT symptoms and prolonged lifespan.

To date, there do not appear to have been any studies conducted which have combined investigation of MeCP2-deficient astrocytes (or microglia) with effects on neuronal electrophysiology. However, it might be expected that reduced glutamate clearance, for example, could potentially influence synaptic responses, plasticity and excitotoxicity.

5.4 MeCP2 Influences Neuronal Morphology in a Predominantly Cell Autonomous Manner

In order to try and establish whether MeCP2 functions either cell autonomously or non-cell autonomously, Kishi & Macklis (2010) created chimeras through transplantation of layer 2/3 pyramidal neurons expressing eGFP. They transplanted various combinations – *Mecp2*-null -> WT, WT -> *Mecp2*-null, WT -> WT (control), and *Mecp2*-null -> *Mecp2*-null (control) – from donor embryos to P2-3 recipients. Recipients were perfused and sacrificed at 8 weeks, post-fixed, and cortical slices immunostained. Kishi & Macklis then performed morphometric analysis on the slices including Scholl analysis. Mecp2-null transplanted into WT showed significantly reduced dendritic complexity compared to WT transplanted into WT suggesting there is no rescue of mutant cells in the WT environment (at 8 weeks). WT neurons transplanted into mutant brains showed a slightly reduced

distal dendritic complexity indicating that there is some non-cell autonomous influence. Combined with control experiments their findings demonstrated that the predominant action of MeCP2 is cell autonomous, at least in the transplant situation. Measurements of soma size of transplanted cells in each of the 4 chimeras revealed a significant size reduction in both WT->mutant and mutant->WT compared to controls. Kishi & Macklis suggested that the apparent non-cell autonomous effects observed were consistent with the potential influence of MeCP2-deficient astroglia and also with BDNF dysregulation. They also acknowledged that the initial pre-transplantation environment of donor cells could also have a long-term influence on the post-transplanted cells.

5.5 MeCP2 and Histones

At least part of the function of MeCP2 involves influencing transcription via binding to methylated DNA and the recruitment of transcription factors.

It has long been known that MeCP2 can recruit the mSin3a and histone deacetylase (HDAC) complex to remodel chromatin in order to partially repress transcription (Jones *et al.*, 1998). MeCP2 was additionally shown to link DNA methylation to histone H3 methylation (Fuks *et al.*, 2003). DNA methylation and chromatin remodelling respond in an activity-dependent manner to control transcription (Martinowich *et al.*, 2003). A mouse model expressing a truncated MeCP2 and which recapitulated many RTT features also exhibited hypermethylation of H3 in the cerebral cortex, cerebellum and spleen (Shahbazian *et al.*, 2002a). Those brain regions also correlated with high levels of MeCP2 expression and the H3 hypermethylation varied in proportion to MeCP2 levels. MeCP2 and histone H1 can compete for chromatin binding sites and different *MECP2* mutations result in various conformations and consequently different DNA/chromatin interactions which may then relate to varying RTT phenotypes (Nikitina *et al.*, 2007).

Histone H3 methylation is involved in the consolidation of experiential memory and this is associated with increased levels of MeCP2 at certain relevant promoter sites (Gupta *et al.*, 2010).

It is known that high levels of MeCP2 are found in neuronal nuclei and that levels of expression vary in a tissue-specific manner and even between different cell types in the same tissue (Shahbazian *et al*. 2002b). MeCP2 levels appear to increase during development and maximise for a given tissue/cell-type at maturity (Shahbazian *et al*. 2002b) and there is a requirement for functional MeCP2 during this process (Singleton *et al.*, 2011). However, just as under-expression is detrimental as in RTT, so is over-expression as in experimentally induced situations (Collins *et al.*, 2004; Alvarez-Saavedra *et al.*, 2010), and in MeCP2-Duplication syndrome (Ramocki *et al.*, 2010). This indicates a requirement to control MeCP2 levels within defined limits in mature neurons. Skene *et al*. (2010) quantified MeCP2 abundance in sorted (NeuN-positive) and unsorted nuclei extracted from mature mouse brain. This gave a value of 16 x 10^6 molecules per nucleus in the NeuN-positive nuclei. This compared to 64 x 10^6 molecules/nucleus of histone H4, i.e. 32 x 10^6 nucleosomes, since there are two H4's per histone octamer. They also estimated the number of methylated CpG's at 40 x 10^6. Hence Skene *et al*. (2010) concluded that the number of MeCP2 molecules in a neuron "approaches the number of histone octamers and meCpG sites". However, their value for the number of MeCP2 molecules obtained from neuronal nuclei is an average across the brain. As it has been previously deduced (see above) that amounts of MeCP2 vary across brain regions and cell types this would suggest that some areas/cells probably do have near histone octamer / meCpG site levels but that others do not. Nevertheless, Skene *et al*. (2010) suggested that MeCP2 was present in sufficient quantities to have a global influence on chromatin state. Comparing WT to *Mecp2*-null brains and quantifying levels of H1, they measured a ~2:1 ratio of H1 between null and WT, suggesting that MeCP2 could competitively substitute for H1 in WT mice. Skene *et al*. (2010) hypothesise that MeCP2 functions to suppress "transcriptional noise" by recruiting HDAC and, by substituting for H1, performing the function of a linker histone. The rescue of mature mice which have developed without MeCP2 (Guy *et al.,* 2007) certainly argues for a MeCP2 neuronal maintenance

function (in mice) irrespective of differences in MeCP2 level across brain regions. It might be that the hypothesised suppression of transcriptional noise is only important in certain neurons/neuronal subsets/regions where the MeCP2 expression is normally high. However, phenotype interpretation is complicated by the potential somatic consequences of MeCP2 deficiency. Nevertheless, it has been observed that many individual heterozygous female RTT mice do not start to exhibit any obvious RTT symptoms until perhaps 4-6 months and this can be followed by a tendency to symptom stabilization and continued breeding even beyond 12 months of age. Mice develop much more rapidly than humans and the number of month's delay before even onset of symptoms in heterozygous mice does not correspond with the equivalent RTT human developmental stage of onset (Guy *et al.*, 2001).

Rett syndrome is caused by loss of function mutations in *MECP2* rather than a null genotype frequently studied in mouse models. In Rett syndrome, different particular mutations correlate with clinical severity and some mutations are more frequent than others giving rise to either milder or severer forms (Bebbington *et al.*, 2008; Raizis *et al.*, 2009; Psoni *et al.*, 2011). Investigations of the two human isoforms, MeCP2-e1 and MeCP2-e2 suggest that the most severe RTT phenotype is caused by mutations in the e1 isoform even though samples may be positive for MeCP2 via the e2 isoform (Saunders *et al.*, 2009; Gianakopoulos *et al.*, 2012). However, it has been recently demonstrated that expressing the e2 isoform alone can rescue Mecp2-null mice providing it is expressed at e1 levels (normally ~9x e2 levels) (Kerr *et al.*, 2012).

5.6 MeCP2 Phosphorylation

It has been shown that MeCP2 can be modified in an activity-dependent manner. Since such modifications cannot take place in neurons which lack MeCP2, it might be expected that MeCP2-ve cells would display different properties to WT or MeCP2+ve cells. Any such differences could manifest as changes in

electrophysiological properties.

Zhou *et al.* (2006) identified a brain-specific site of neuronal activity-dependent MeCP2 phosphorylation at serine 421 (S421). This finding was extended to that of S421 phosphorylation in seizure-induced synaptic activity *in vivo* in rat and mouse brains. Another site of MeCP2 phosphorylation was identified at serine 80 (S80) and it was further established that S421 and S80 are oppositely regulated dynamically (Tao *et al.*, 2009). Loss of phosphorylation at S80 was linked to a reduced association to some of the MeCP2 chromatin target sites. Tao *et al.* concluded that phosphorylation at S80 was associated with resting neurons and S421 with active ones. Recently, Li *et al.* (2011a) generated knock-in mice with point mutations at S421 (S->A) and at another phosphorylation site, S424 (S->A), so as to prevent phosphorylation at these sites. They found that this loss of phosphorylation gave rise to enhanced synaptogenesis, enhanced LTP and improved hippocampal memory compared to WT. Microdissection of the hippocampi from the knock-in mice revealed increased *Bdnf* transcription. However, Cohen *et al.* (2011) generated mice with a single knock-in point mutation at S421 (S->A) to just prevent S421 phosphorylation. In contrast to Li *et al.* (2011a) their mutant mice resulted in defective dendritic and synaptic development and the mice exhibited abnormal behavioural responses. This would suggest that the involvement of S424 phosphorylation is also an important factor but the reasons for the differences in phenotypes have yet to be explained.

6 MeCP2 and Electrophysiology

This section reviews the literature on MeCP2 which particularly relates to studies involving electrophysiology and highlights the major findings and themes that have arisen.

There have been a number of studies looking into the functional aspects of MeCP2 and which have included electrophysiological investigations across various brain regions, often combined with molecular, structural and morphological studies. Both extracellular and intracellular recording techniques have been used. Investigations have examined how a deficit in MeCP2 has influenced properties of neurons and glia in developing and adult animals. Several recurring themes have arisen which form the basis of this section. These are:

a) The balance of excitation and inhibition and GABAergic effects
b) Cell autonomous and non-cell autonomous properties
c) Transcriptional regulation

a) The balance and the proportional responses to excitation and inhibition is a fundamental property of normal, i.e. WT, oscillatory brain networks and balance is achieved over a wide range of synaptic conductances and rapidly changing activity levels, although opposing conductances do not necessarily achieve perfect correlation. Excitatory responses are predominantly glutamatergic and inhibitory ones are GABAergic. The E/I balance controls stability and sensitivity to external input. It has been demonstrated that oscillatory phase is determined by inhibitory activity in the rat hippocampus (Atallah & Scanziani 2009). Computational studies have indicated that membrane potential noise has a major impact on network oscillation frequency by affecting recovery time after inhibition (Economo and White 2012). Altered E/I balances have been observed in a number of neurological disorders such as autism spectrum disorder, schizophrenia, diabetic neuropathy, Fragile X syndrome, seizures and epilepsy, bipolar disorder, and major depressive disorder.

b) Cell autonomous effects arise as a result of only mutant cells exhibiting the abnormal phenotype and any non-mutant cells exhibit a WT phenotype and or not affected by the presence of mutant cells. Conversely, non-cell autonomous effects arise because mutant cells also influence the properties and characteristics of non-mutant cells. This can happen where mosaicism results in populations of mutant and non-mutant cells, as in RTT. It can also occur in animal models where selective knockout or knockdown of particular cell-types or where specific cell populations have been engineered.

c) 'Transcriptional regulation' is an umbrella term which encapsulates the many and varied mechanisms by which gene expression is controlled. Up-regulation can be achieved via transcriptional activators, down-regulation via transcriptional repressors. Specific genes can be up-regulated through histone acetylation by activators and down-regulated through histone deacetylation by repressors. Access by transcription factors to DNA can be controlled by histone methylation/demethylation.

Additionally, the effects of MeCP2 re-expression and symptom reversal, and some studies on various brain areas are discussed.

6.1 Shift in Excitatory/Inhibitory Balance and the Tendency towards Hyperexcitability

Most electrophysiology studies have used extracellular recording to investigate network properties. Dani *et al*. (2005) appear to be the first investigators to use whole-cell patch clamp on Mecp2-mutant mice. They bred male *Mecp2*-null animals and prepared coronal cortical sections from P30-P35 (early symptomatic) mice. Dani *et al*. (2005) first looked at spontaneous AP discharges in L5 (S1) pyramidal cells. Using a modified ACSF they observed decreased spontaneous firing rates in mutants compared to WT, both at 25°C and 31-33°C

when recording in current-clamp. They also measured spontaneous firing rates in younger, presymptomatic mice but still observed a reduced mean firing rate compared to WT although the reduction was not as great as with the symptomatic mice. They further measured intrinsic responses to depolarising current steps in regular spiking pyramidal cells from 4-5 week-old mice but found no significant difference between mutant and WT for spike threshold, input resistance, or the firing frequency vs. current step relationship. Measurements of spontaneous synaptic charge in voltage clamp revealed an increase in inhibitory and decrease in excitatory charge for 4-5 wk. mutant vs. WT mice. In the same age group they measured reduced mean peak miniature excitatory synaptic current (mEPSC) amplitudes but there was no significant difference in mean peak miniature inhibitory (mIPSC) amplitudes. Dani *et al*. (2005) concluded that there was an overall reduction in excitatory response and a shift towards increased cortical inhibitory drive in mutant mice and that this was progressive according to age/symptom degree.

6.1.1 MeCP2 Deficiency Gives Rise to Excitatory, but not Inhibitory Changes

Nelson *et al*. (2006) used whole-cell recording to investigate possible differences between *Mecp2*-null and WT neurons in dissociated hippocampal cultures made from P1 mice. Neurons were cultured for 11-14 days. They observed a significant decrease in mEPSC, but not mIPSC, frequency in *Mecp2*-null neurons compared to WT. Using immunostaining of MAP2 and synapsin revealed no difference in number of presynaptic terminals in mutant vs WT neurons. Nelson *et al*. (2006) also measured evoked responses to various stimuli. Trains of stimuli at a frequency of 10Hz resulted in short-term depression (STD) in both mutant and WT cells. They used the first two responses in the train to calculate a paired-pulse ratio. Paired-pulse responses (PPR's) were significantly lower in mutant cells at 30Hz and 10Hz frequencies. They also observed a reduction in normalised amplitude for mutant cells over the first 2 seconds of stimulation at 10Hz and a slower recovery time for mutant cells at 1Hz following the 10Hz depression. They did further experiments using a histone deacetylase inhibitor,

Trichostatin A (TSA), to treat WT cultures and observed a reduction in mEPSC frequency but no change in mIPSCs. In floxed WT cultures treated with lentivirus expressing Cre recombinase used to knockout MeCP2 they observed a significant reduction in mEPSC frequency suggesting that MeCP2 has involvement in regulatory effects on synaptic transmission.

Moretti *et al*. (2006) performed extracellular recordings on brain slices from 18-22wk *Mecp2*$^{308/y}$ mice. At CA1 they observed an apparent enhanced synaptic transmission (larger fEPSP slope) but attenuated PPF, although the comparison to WT only appeared to be significantly different at a 20ms interstimulus interval. LTP was significantly impaired at tetanic (100Hz) and at Theta burst stimulations (cf. Asaka *et al*. (2006) study using *Mecp2*-null mice above). Moretti *et al*. (2006) obtained similar results in cortical slices.

Chao *et al*. (2007) confirmed that both MeCP2 deficiency and overexpression resulted in alterations to the frequency of mEPSCs and changes in the magnitude of evoked EPSCs using autaptic (Bekkers & Stevens, 1991) hippocampal cultured neurons. The suggested mechanism was the regulation of synapse numbers which was observed via immunostaining of VGLUT1 and PSD95 to specifically evaluate glutamatergic synaptic density separate from GABAergic synaptic density. Loss of MeCP2 resulted in a 39% decrease of the colocalised glutamatergic synaptic markers (VGLUT1 and PSD95), and overexpression of MeCP2 resulted in a 60% increase in the same colocalised synaptic markers compared to WT. Chao *et al*. (2007) then investigated the situation *in vivo* using hippocampal slices from 2 week and 5 week old male mutant mice. With 2-week old mice they observed a 19% reduction in VGLUT1 in the CA1 s.r. from *Mecp2*-null mice and an increase of 80% in VGLUT1 from 2x *Mecp2* overexpressing mice compared to WT. However, by 5 weeks the levels of VGLUT1 had tended to normalise in both mutants suggesting a compensatory mechanism at work. This is, perhaps, a counterintuitive result since *Mecp2*-null mice start becoming symptomatic at about 5 weeks so it might be expected that alterations in synapse number would be more apparent at that time point. Unfortunately, Chao *et al*. (2007) did not

also investigate inhibitory characteristics in Mecp2-mutant neurons (but see Zhang *et al*. (2008) below).

6.1.2 MeCP2-deficient Hippocampus Prone to Hyperexcitability

The properties of hippocampal inhibitory circuits in symptomatic *Mecp2*-null mice were investigated using extracellular recording and whole-cell patch clamp by Zhang *et al*. (2008). They observed a reduction in the frequency of spontaneous rhythmic field potentials (SRFP) in mutant compared to WT controls but found no difference in basic intrinsic properties of hippocampal pyramidal neurons. Similarly, they found no significant difference in evoked IPSC between mutant and WT CA3 pyramidal neurons. Spontaneous excitatory activity was measured in CA3 pyramidal neurons voltage clamped at around normal resting potential (-60mV) and Zhang *et al*. (2008) were able to demonstrate a reduced basal excitatory activity. Using NBQX to block AMPA/kainate receptors and ADAC, which selectively reduces glutamate release, they measured a reversible reduction in SRFP frequency in WT hippocampal slices. Hence they suggested that it is a reduction in excitatory drive which slows the SRFP frequency in mutant slices although they did not actually establish a cause and effect in mutants. However, external stimulation (80Hz for 1 second) in the CA3 *alveus/oriens* significantly increased CA1 field EPSPs and this stimulation also appeared to induce discharges with sharp wave-like characteristics in mutant slices. No such sharp waves were observed in WT slices and Zhang *et al*. (2008) suggested that mutant slices could be stimulated to transition into a hyper-excitable state. They further measured evoked CA3 field potentials in the presence of the $GABA_A$ antagonist bicuculline and observed multiple spike waveforms and self-sustained interictal-like field potentials in mutant, but not WT, slices. Zhang *et al*. (2008) suggested that the network in mutant mice was 'primed' and susceptible to slight changes in the excitatory/inhibitory balance.

Seizures are a feature of Rett syndrome with a reported incidence of 81% (Jian *et al*. 2006), and seizure activity can be easily induced in *Mecp2*$^{stop/y}$ mice

(Mcleod et al. 2013). Seizure activity in early development, but not in adults, has been linked to dendritic spine loss and reduced expression of NR2A and PSD95 in mouse models of epilepsy. These findings suggest seizure activity can interrupt synapse development with consequent long-lasting effects on learning and memory (Swann et al. 2007). A deficit in MeCP2 could possibly result in such seizure activity via disruption of synaptic maintenance functions at the molecular level leading to hyperexcitability.

6.1.3 Hyperexcitability in Mutant Hippocampus Linked to CA3 and GABAergic Impairment

Calfa *et al*. (2011a) performed extracellular CA1 recordings on hippocampal slices from P16-P55 hemizygous male mice stimulating Schaffer collaterals. They reported a larger fESP input/output vs. stimulus intensity slope in mutant slices compared to WT, and PPRs were significantly reduced in mutants at 10, 20, 50 and 100ms interstimulus intervals. Voltage-Sensitive Dye imaging (VSD) indicated that the CA1 in mutant slices is both hyperexcitable and more sensitive to 4-aminopyridine (4-AP), an epileptogenic agent. This excitability is lost if CA1 is disconnected from CA3 and can be reduced to similar levels to WT with application of 50μM Adenosine. Using quantitative electron microscopy Calfa *et al*. (2011a) measured fewer docked vesicles at active sites in spine and shaft synapses. They concluded that observed network hyperactivity in mutant slices originated in CA3 and they suggested this was due to CA3 GABAergic impairment.

6.1.4 KO of Histone Deacetylases

Using dissociated hippocampal cell cultures Nelson *et al*. (2011) investigated the electrophysiological properties of *Mecp2*-null and lentivirus-mediated knockout of histone deacetylases *Hdac1* and *Hdac2*. Nelson *et al*. (2011) investigated short-term plasticity by measuring PPF ratios using whole-cell patch clamp across a range of stimulus frequencies (20Hz – 1Hz). Paired-pulse stimuli were

applied via bath electrodes in 2-3 week old cultures. Evoked EPSCs and IPSCs were recorded with appropriate pharmacological blockades to isolate the responses. Compared to WT, *Mecp2*-null cells gave significantly reduced PPRs at 50, 100 and 200ms interstimulus intervals. There were no significant differences compared to WT for IPSC PPRs, supporting the hypothesis that MeCP2 is an excitatory regulator. For *Hdac1* and *Hdac2* KO cells, PPRs were reduced at 50 and 100ms intervals with also no significant differences for IPSC PPRs compared to WT. Nelson *et al*. (2011) measured EPSC amplitudes for trains of 5 stimuli at 2, 5 and 10Hz. Mean EPSC amplitudes were reduced at all 3 stimulus frequencies for the *Mecp2*-null cells. For *Hdac1* KO there were no significant differences in EPSC amplitudes compared to controls. For *Hdac2* KO cells there was a significant increase in EPSC amplitudes compared to control cells. However, in this case the control amplitudes were themselves much lower than those in the other previous comparisons and it appears the lower control amplitudes could have been a reason for the *Hdac2* KO significance. Nelson *et al*. (2011) did not suggest why the control amplitudes were so much lower. Also, the authors did not normalise the responses to the first EPSC in the train in any of their experiments. Nelson *et al*. (2011) performed a further experiment in which they stimulated cells at 10Hz and recorded the EPSC and IPSC responses over the first 2 seconds. In this case they *did* normalise the subsequent responses to the first EPSC in the train. Only the *Mecp2*-null cells showed a reduced response (depression) and which was significantly different from the controls but only in the first second of the pulse train. The equivalent experiment measuring IPSCs showed no difference between any of the mutants and controls. It was perhaps unfortunate that they did not extend their stimulation protocols to higher frequencies/shorter interstimulus intervals which might have been more likely to highlight any differences. The authors concluded that their results supported the hypothesis that deficits in MeCP2 resulted in a greater excitatory drive thus causing a shift in the excitatory/inhibitory balance. However, it has to be noted that the hippocampal architecture and network is not present in dissociated cultures so perhaps that particular *milieu* may not be so suitable for investigating excitatory/inhibitory relationships.

6.1.5 RNAi Knockdown of MeCP2 Gives Rise to Reduced Excitatory Drive

Using RNA interference, Wood *et al*. (2009) an intrauterine electroporation protocol produced mice with a sparsely knocked-down eGFP-tagged phenotype (*Mecp2*^{kd}) of motor cortex L2/3 pyramidal cells with about 15% expressing GFP. In cortical slices from 3-4 week knockdown mice, intrinsic electrophysiological properties between pairs of knockdown and WT cells did not reveal any overt differences. Using laser scanning photostimulation (LSPS) of caged glutamate they observed a reduced excitatory input confined to a L3/5A -> L2/3 pathway which was not accompanied by any deficit in inhibitory pathways. In a follow-up study (Wood & Shepherd, 2010), similar findings were reported in comparisons between presymptomatic *Mecp2*-null and WT mice.

6.1.6 Increased Synaptic Excitability as a Consequence of MeCP2 Overexpression

Collins *et al*. (2004) overexpressed MeCP2 in mice (FVB strain) via cloning using a P1 bacteriophage artificial chromosome incorporating the entire human *MECP2* genomic locus. 6 founders were generated and 5 out of 6 bred which gave rise to 5 different lines. The resulting phenotype developed progressive neurologic dysfunction which varied in severity according to higher levels of MeCP2 overexpression observed across different mouse lines. Age of onset of symptoms also varied and mice died prematurely. Extracellular recordings of acute hippocampal slices from one transgenic mouse line (Tg1) showed *increased* short-term synaptic plasticity (PPF) compared to WT littermates. LTP was also enhanced. Collins *et al*. (2004) created double mutants by breeding the Tg1 overexpressing mice with *Mecp2*$^{+/null}$ (Bird strain). The double mutants survived to at least 33 weeks and appeared to express a WT phenotype. Tg1 mice also sometimes exhibited clonic seizures from 20 weeks and EEG recordings were abnormal at times when no seizures were apparent.

6.2 MeCP2 Deficiency Associated with GABAergic Circuit Dysfunction

6.2.1 MeCP2 KO in GABAergic Neurons Results in RTT-like Phenotype

Transgenic mice with MeCP2 KO specific to GABAergic neurons have been produced and investigated (Chao *et al*. 2010). They had observed that WT cortical GABAergic neurons expressed approximately 50% more MeCP2 than non-GABAergic neurons suggesting that MeCP2 is particularly important in GABAergic cells. They used a bacterial artificial chromosome (BAC) containing the *Viaat* promoter to target Cre expression in GABAergic neurons. *Viaat* mice were bred with *Mecp2*$^{flox/+}$ mice to produce *Viaat-Mecp2*$^{-/y}$ mice which expressed very little Mecp2 in GABAergic neurons. *Viaat-Mecp2*$^{-/y}$ mice developed apparently normally for the first 5 weeks but then began exhibiting RTT-like symptoms which became progressively more severe. Recordings of mIPSCs from L2/3 and striatal neurons in acute slices from *Viaat-Mecp2*$^{-/y}$ mice showed reduced amplitude and charge but similar frequency to controls. mEPSCs were similar in all three respects in comparison to controls. They did not specify the ages of the mice used. 9-week old *Viaat-Mecp2*$^{-/y}$ mice were not observed to suffer seizures but EEG recordings were abnormal compared to controls. Extracellular recordings of hippocampal slices from 11-13 week old *Viaat-Mecp2*$^{-/y}$ mice showed a reduction in theta-burst induced LTP and alteration in saturation characteristics compared to controls. The authors suggested that MeCP2 deficiency in GABAergic neurons plays a central role in the pathogenesis of RTT. However, this conclusion may be an oversimplification and it may be that MeCP2 deficiency in any brain cell type could eventually lead to RTT-like symptoms – presumably via disruption of cellular maintenance functions. More detailed information on exactly how MeCP2 functions in neurons is required.

6.2.2 Mecp2-null Brainstem Exhibits GABAergic Dysfunction

GABAergic synaptic dysfunction has been observed in the brainstems of early postnatal *Mecp2*-null mice (Medrihan *et al.*, 2008). Acute slices containing the ventrolateral medulla (encompassing the respiratory control network) were used to measure pharmacologically-isolated spontaneous IPSCs in mutant and WT controls using whole-cell patch clamp of unspecified cells. IPSC amplitude and frequency were reduced in mutant cells but, in contrast, isolated spontaneous EPSC amplitude and frequency were increased in mutant slices. The authors then used TTX to isolate post from presynaptic currents and curve fitting to distinguish between GABAergic and glycinergic synaptic activity. They found that GABA-mediated synaptic events (mIPSCs) were reduced by 50% in mutant slices. In the presence of strychnine to suppress glycinergic activity and TTX to block AP's they measured a reduction in frequency but not amplitude of GABAergic mIPSCs in mutant slices. Analysis of waveforms revealed that decay time was shorter in mutants compared to WT. They further measured a reduction in expression of $GABA_A$ receptor subunits and of the vesicular GABA transporter, VIAAT, compared to WT controls. Unfortunately, Medrihan *et al*. (2008) did not also include symptomatic mice in their study and do not appear to have followed up their findings.

6.2.3 GABAergic Thalamic Circuit Properties in Presymptomatic Mice

Zhang *et al*. (2010b) investigated the properties of the GABAergic circuits in acute brain slices of the thalamus – the ventrobasal complex (VB) and the reticular nucleus (RTN) – from presymptomatic P6-P26 *Mecp2*-null mice. They used whole-cell patch clamp to measure intrinsic properties of VB and RTN cells, and pharmacologically isolated IPSPs. Stimulation in the RTN was used to evoke VB IPSPs. *Mecp2*-null neurons from P14-P16 mice gave significantly fewer mIPSCs in the VB compared to WT although there were no differences in peak amplitudes or waveform characteristics. By contrast, the RTN showed a greater

number of mIPSCs – 60% more than WT, but again no changes in peak amplitudes or waveform characteristics. There were no differences for evoked paired pulse ratios at 50 and 100ms interval for mutant VB neurons compared to WT. There was an increased variation for mutant RTN neurons but again no difference in PPRs compared to WT. Zhang *et al*. (2010b) did observe differences with respect to unitary evoked IPSC's with cumulative amplitudes shifted to the left for VB mutant neurons, and to the right for RTN mutant neurons compared to WT. They did not observe any differences in intrinsic properties of P15-P17 mutant RTN neurons compared to WT. VGAT immunostaining showed fewer stained puncta in mutant VB neurons compared to WT from P15-P17 mice.

6.3 Stem Cells from RTT Patients: MeCP2 Influences Glutamatergic Synapse Number

Although mouse models of RTT have proved a very useful research tool, and symptomatic mice recapitulate many RTT characteristics, the mouse models are not identical to the human syndrome. (Marchetto *et al.*, 2010) have developed a model based on fibroblast stem cells taken from RTT patients and expressing different *MECP2* mutations. Such induced pluripotent stem cells (iPSCs) have the ability to generate neural progenitor cells (NPCs) which can proliferate and demonstrate X-inactivation thus giving rise to MeCP2 mosaicism. After differentiating cell cultures for 8 weeks, Marchetto *et al*. (2010) used immunostaining to show that generated neurons had a reduced glutamatergic synapse number which they were able to attribute to MeCP2-deficiency. They also observed morphological changes in RTT neurons compared to WT. In common with mutant mouse neurons, RTT neurons had reduced spine density and smaller soma. Treatment with IGF1 resulted in increased synapse number. Also, it was observed that RTT cells expressing a nonsense mutation (Q244X/C730T – one particular MeCP2 mutation found in 1% of Rett patients) could be treated with an aminoglycoside antibiotic such as gentamicin which inhibit ribosomal proofreading and force a readthrough of the premature stop codon. With a low gentamicin dose the treatment resulted in an increase in

glutamatergic synapses after one week. RTT Neurons which had been differentiated for at least 6 weeks showed reduced frequency and amplitude of spontaneous EPSCs compared to WT but no changes in sIPSCs.

6.4 MeCP2 Influences NMDA Receptor Subunit Expression

N-methyl-D-aspartate receptors (NMDARs) play a key role in excitatory synaptic transmission and NMDAR dysfunction is implicated in a number of neurological diseases including Alzheimer's disease and schizophrenia. There are a number of different NMDAR subtypes whose properties are determined by the subunit composition of the receptors (Cull-Candy *et al*. 2001; Paoletti and Neyton, 2007). Selected relevant literature is reviewed below.

Asaka *et al*. (2006) investigated CA1 hippocampal network responses using extracellular recording of acute slices from presymptomatic (3-5 wk) and symptomatic (6-10 wk) *Mecp2*-null male mice in comparison to WT littermates. They dissected the slices to disconnect CA3 from CA1 to prevent epileptiform activity. They observed a significant reduction in tetanic stimulus-induced LTP magnitude in mutant mice over 6 wks of age compared to WT controls.

Immunoblots revealed no change in AMPA receptor (GluR1 and GluR2) prevalence compared to WT, and similarly no significant difference for one NMDA receptor (NR1 == GluN1) but they did measure a decrease in NR2A (==GluN2A) and an increase in NR2B (==GluN2B) prevalence. They did not observe any difference in tetanic stimulation-induced LTP between mutant and WT controls in presymptomatic mice. Low-frequency (Theta range – 5Hz) stimulation did not elicit LTP in symptomatic mutant mice with no difference in LTP response between presymptomatic mutant and WT. Extracellular PPF showed no difference between presymptomatic mutant and WT mice across a range of interstimulus intervals (50, 100, 150, 200, 250ms). Symptomatic mutant mice showed a marked reduction in PPF ratio at 50ms and 100ms compared to WT.

However, PPF ratios for the WT were larger at 50ms and especially at 100ms relative to the previous presymptomatic comparison.

A more recent investigation by the same research group measured the prevalence of NMDA receptor subunits, GluN1 and GluN2A, and found a reduction of the subunit proteins compared to WT in *synaptic membranes* isolated from whole brains taken from 70-90 day *Mecp2*-null mice. There was also a reduction in PSD95 in the synaptic membranes but prevalence of the NMDA receptor subunit GluN2B was unchanged (Maliszewska-Cyna *et al.*, 2010). GluN1 appears to have a role in secondary dendrite formation in the developing hippocampus (Henle *et al.*, 2011). Using a selective GluN2A antagonist (NVP), pyramidal neurons in acute brain slices containing the amygdala from WT SD rats failed to achieve LTP induction when stimulated in the thalamic medial geniculate nucleus. However, blockade of GluN2B receptors did not prevent LTP induction. Conversely, blocking GluN2B prevented LTD induction but blocking GluN2A did not prevent LTD suggesting selective roles for the subunits (Dalton *et al.*, 2012).

6.4.1 Differential Expression of NMDA Receptor Subunits and Altered Postsynaptic Kinetics

Bellone & Nicoll (2007) observed the activity-dependent ability of WT rat neonatal (P2-9) NMDAR subunits to switch between GluN2A (NR2A) and GluN2B (NR2B). LTP induction appeared to cause a swap of GluN2B subunits by GluN2A subunits. This swap was apparently able to be reversed by depotentiating with low-frequency stimulation. However, this ability appeared to be lost in older animals (P16-21) and the change was accompanied by a shift to predominantly GluN2A receptor subunits. The changes in prevalence between the subunit types was accompanied by altered postsynaptic kinetics with the immature GluN2B-containing receptors exhibiting a slower EPSC decay compared to GluN2A receptors. The GluN2B-selective antagonist Ifenprodil causes a larger decrease in time constant in immature animals compared to older ones. Interestingly, the

results reported by Asaka *et al*. (2006) (see above) in respect of symptomatic *Mecp2*-null mice suggest that the MeCP2 deficiency causes a switch back from the prevalence of GluN2A subunits associated with normal mature mice to a prevalence of the immature GluN2B subunits. A similar situation has been reported for the visual cortex (Lee *et al.*, 2008) where suppression of neuronal activity by TTX (tetrodotoxin) caused an increase in NR2B/GluN2B NMDA receptor subunits. It was shown that activity-dependent GluN2B expression is mediated by MeCP2 i.e. MeCP2 normally represses GluN2B expression. Yang *et al*. (2011) have recently investigated the molecular regulation of GluN2A and 2B subunits in WT rats and mice. They found that the relative contributions of the different subunits are regulated by G-protein-coupled receptors. Lee *et al*. (2008) also observed that increase in GluN2B expression occurred independently of BDNF levels but expression of GluN1 and GluN2A was blocked through inhibition of BDNF signalling.

Li *et al*. (2011b) recently investigated the contribution of GluN receptor subunits to CA3-CA1 synaptic plasticity. Comparing responses in hippocampal slices from GluN2A$^{-/-}$ transgenic mice to WT they reported a reduced maximum GluN EPSC amplitude in the mutant slices. Also, they were able to induce long-lasting potentiation (LLP) in WT slices but not in mutants. Long-lasting potentiation was defined as potentiation lasting more than 30 mins. Blocking GluN2B receptor subunits with the highly selective antagonist Ro 25–6981 in WT rat slices resulted only in a short-term potentiation but LLP is required to maintain LTP. Hence Li *et al*. (2011b) deduced that both GluN2A and GluN2B receptor subunits were required for LLP.

The distribution of NMDA receptors across the brains of 2-week and 7-week old Mecp2-null, heterozygous, and WT mice has recently been investigated by Blue *et al*. (2011) using autoradiography of H^3-labelled CGP-39653, an NMDA receptor ligand. They found significant variations between genotypes, ages and across brain regions. Het mice showed more variability of NMDA receptor density in comparison to either WT or null mice such that no significant differences were

reported between WT and Het. This result was in contrast to their previous measurements in post-mortem brains from RTT patients (Blue *et al.*, 1999). In null mice, Blue *et al*. (2011) reported a 'bimodal pattern' with NMDA receptor densities decreased at 7 weeks but increased at 2 weeks, compared to WT and which was apparently similar to that previously seen in the brains from RTT patients. Additionally, they measured protein expression of GluN1/NR1 in 1, 2 and 7-week old WT and *Mecp2*-null mice using Western blots. The only significant difference was an increased GluN1 level in Mecp2-null mice at 2 weeks but this had converged back to the WT level by 7 weeks. Unfortunately, Blue *et al*. (2011) did not look at GluN2 subunits.

6.5 Electrophysiology and RTT Mouse Model Symptom Reversal

It has been demonstrated that symptoms developed by RTT mice can be reversed following expression of MeCP2 in mice in which it had previously been prevented from being expressed. As well as the symptom rescue, LTP was normalised. This rescue of symptomatic RTT mice is discussed below.

Guy *et al*. (2007) published a seminal paper on the reversal of RTT symptoms in mice. Male symptomatic mice bred with a modified estrogen receptor fusion Cre (Cre-ER) and a lox-stop cassette to silence MeCP2 expression (*Mecp2*$^{\text{lox-stopy/y}}$, *cre-ER*) were rescued by cassette deletion using tamoxifen injections to activate Cre thus allowing expression of MeCP2. Male mutants even with advanced symptoms were also rescued and had much extended lifespans (over 17 weeks). Similarly, symptomatic heterozygous female conditional *Stop* mice were also progressively rescued. No significant differences in LTP were observed between presymptomatic and WT female littermates but LTP responses were reduced in symptomatic females. However, after sustained rescue via tamoxifen injections the LTP responses from previously symptomatic heterozygous females became indistinguishable from WT controls.

Hence, in mice, the apparent negative developmental effects of MeCP2 deficiency do not prevent the rescue of symptomatic adults. This provides more evidence that argues for a mainly neuronal/cellular maintenance function for MeCP2. Guy *et al*. (2007) reiterate that the time to symptom onset is much more similar in real-time (4-12 months in heterozygous female mice, 6-12 months in human females) than the corresponding developmental timepoints. This suggests that, when performing electrophysiological measurements, the symptom status of RTT model mice is more important than their absolute age.

Robinson *et al*. (2012) have performed further and more quantitative assessments of RTT symptom reversal which included measuring the degree of reversal of structural deficits observed in cortical neurons.

6.5.1 Hippocampal LTP Deficits in Symptomatic Mice Partially Rescued by Memantine

RTT symptoms can also be partially rescued using pharmacological intervention with the Alzheimer's drug, memantine. Weng *et al*.(2011) recently measured induced LTP (Stimulation of 100 pulses at 100Hz) in acute hippocampal slices from presymptomatic 4 week-old, and symptomatic 12-15 week-old, *Mecp2*$^{stop/y}$ mice compared to WT controls. There were no significant differences between presymptomatic and WT controls but slices from symptomatic mice gave a significantly reduced LTP. Again, there were no significant differences in extracellular paired-pulse facilitation between presymptomatic and WT using a 50ms interstimulus interval. However, slices from symptomatic mice showed a significant LTP deficit. Mutant slices from strongly symptomatic mice also displayed altered LTP saturation characteristics consequent from repeated high frequency stimulations (HFS), and tending towards depression. An intermediate HFS response was also seen in slices from mildly symptomatic mutant mice. PTP was also similarly impaired in a symptom-dependent fashion compared to WT. Acute treatment of mutant slices from strongly symptomatic mice with the novel Alzheimer's Disease drug memantine (1μM) partially reversed the PTP and LTP

deficits. However, systematic treatment of *Mecp2*$^{stop/y}$ mice (30mg/Kg/day, oral) from onset of symptoms did not appear to result in symptom improvement or increased longevity. Memantine is a low affinity NMDA receptor antagonist but also acts on other receptors and is a dopaminergic (D_2) agonist (Rammes *et al.*, 2001; Seeman *et al.*, 2008). Memantine has been shown to be neuroprotective and to improve cognitive function and learning in AD models (Minkeviciene *et al.*, 2008; Minkeviciene *et al.*, 2004; Nyakas *et al.*, 2011), and has been clinically approved for use in moderate to serious Alzheimer's Disease. However, dosage is quite critical and also depends on method of administration (Parsons *et al.*, 2007).

6.6 Effects of MeCP2 Deficiency in Various Brain Regions

Although the subject of this study is the hippocampus, the electrophysiological properties of neurons in various other brain regions have been studied in RTT mice. It is useful to make comparisons, and a review of a selection from the literature follows.

6.6.1 Locus ceruleus Neurons in Heterozygous RTT Mice

Taneja *et al.* (2009) examined the electrophysiology of neurons in the *locus ceruleus* (LC) in acute slices from P26-P28 mice using whole-cell patch clamp. *Mecp2*-null neurons showed a higher AP firing frequency for the same current injection compared to WT. This is one of the few studies which have included heterozygous female Mecp2$^{+/-}$ mice. They found that plots of firing frequency against current for MeCP2+ve cells were comparable to WT and those for MeCP2-ve were comparable to *Mecp2*-null cells. This is a surprising result since the heterozygous mice were young and presymptomatic. The result, though, argues for a cell autonomous effect for MeCP2 and possibly also a region-specific function since differences in heterozygous compared to WT had not previously been observed in presymptomatic mice across other brain regions.

6.6.2 MeCP2, Locus Ceruleus and Biogenic Amines

The *locus ceruleus* (LC) region was investigated by Zhang *et al*. (2010a) and also by Roux *et al*. (2010). The LC is situated in the brainstem and is the principal noradrenergic (NA) site innervating rostral and caudal brain regions. The LC-NA has been identified as acting as a neuromodulatory system which can modulate autistic symptoms via febrigenesis (Mehler & Purpura, 2009). Tyrosine hydroxylase (TH) is the rate-limiting enzyme in the synthesis of NA, and Roux *et al*. (2010) measured the levels of TH in the LCs of developing RTT male and adult (10-15 month) female heterozygous mice using quantitative RT-PCR and immunological techniques. Using RT-PCR they observed a progressive reduction of TH mRNA in the dissected out pons containing the LC taken from *Mecp2*-null mice: -36% at P10, -47% at P30, and -42% at P50; -44% in adult $Mecp2^{+/-}$ compared to WT. These deficits were accompanied by changes in TH immunostaining in the LC in *Mecp2*-null at P30 and P50, and in the heterozygous females. However, reductions in staining intensity and reductions in TH+ve neuron numbers reached significance only in P50 *Mecp2*-null mice with no clear deficits in the (symptomatic) heterozygous females. However, levels of mRNA expression do not necessarily correlate with actual protein levels. It would seem unlikely that there is a simple relationship between the presence/absence of MeCP2 and corresponding levels of expression of TH/NA.

Zhang *et al*. (2010a) investigated the intrinsic electrophysiological properties of LC neurons in acute pontine brain slices from 3-4 week old *Mecp2*-null mice. The mice were bred to specifically express eGFP in the LC neurons. Using whole-cell current clamp there was no significant difference in RMP between the null and WT controls. Zhang *et al*. (2010a) did measure a stronger inward rectification in null mice which the authors thought was probably due to $K_{ir}4.1$ overexpression. Using quantitative RT-PCR they did indeed identify significantly increased expression of $K_{ir}4.1$ and also TASK1 and TASK3 channels. (TASK = 2-pore domain weakly inward-rectifying K^+ channel (TWIK)-like acid-sensitive K^+ channel). There

was no significant difference between null and WT in respect of input resistance but a smaller membrane time constant in null cells suggested a smaller surface area and this was confirmed by measurement. Analysis of AP properties revealed no significant differences in AP amplitude or decay time. But there was a significant increase in AP rise time, $T_{1/2,}$ and a significant reduction in AP threshold in the null mice compared to WT. The alterations in AP kinetics appeared to correlate with a decrease in the mRNA expression of $Na_{v1.2}$ but not $Na_{v1.1}$ compared to WT. Amplitude of mAHPs was reduced in null compared to WT. Zhang *et al*. (2010a) observed two types of cells – those with mAHP alone and those with an additional fAHP component. They designated the two types as Type A and Type B respectively. Null Type A cells showed a higher spontaneous firing frequency than null Type B cells and a higher firing frequency than WT Type A cells. Using evoked AP's they did not observe any overall difference in spike frequency adaption between null and WT LC cells.

The effects of loss of MeCP2 in aminergic neurons have been investigated by Samaco *et al*. (2009). They found a decrease in the levels of a dopamine metabolite, homovanillic acid (HVA), and in a serotonin metabolite, 5-hydroxyindoleacetic acid (5-HIAA) in CSF from RTT patients compared to controls. Levels in patients varied according to particular mutations, and patients with severe RTT had greater reductions than with mildly affected patients.

Samaco *et al*. (2009) also measured reductions in dopamine (DA), serotonin (5-HT), and norepinephrine (NE) (== noradrenaline, NA) in *Mecp2*-null mice brains compared to controls. Conditional KO mice bred with MeCP2-deficiency in TH expressing cells (DA/NA-ergic) or in PET1 (PC12 *ets* factor 1 – a marker for 5-HT, serotinergic) expressing cells produced mice with specific behavioural phenotypes. Unfortunately, Samaco *et al*. (2009) did not report any electrophysiological data on the KO mice.

Santos *et al.*(2010) also measured altered levels of DA, 5-HT and NA/NE across various brain regions in *Mecp2*-null mice compared to WT. At 3 weeks of age levels of NE and 5-HT were significantly lower mainly in the prefrontal and motor cortices. By 8 weeks relative deficits of NE, DA, and 5-HT were also seen in the cerebellum and hippocampus. The deficits appeared to correlate with abnormal motor phenotypes and the authors suggested the null mice reflected the ataxia seen in RTT patients and that the deregulation of monoamines is a contributor to the progressive motor pathophysiology of RTT. Isoda *et al.*(2010) observed a significant loss of fibres immunoreactive to 5-HT innervating the hippocampus by P56 in *Mecp2*-null mice.

Recently it has been shown that a combination of DA and 5-HT signalling can regulate the s421 phosphorylation of MeCP2 in a region and cell-specific manner (Hutchinson *et al.*, 2012). It could be hypothesised that the deficit of MeCP2 in heterozygous female mice, and similarly in female RTT patients, could lead to dysregulation of DA and 5-HT, in turn negatively affecting the phosphorylation of the functional MeCP2 that is present in heterozygous brain, thus reinforcing a dysfunction in respect of what would normally be activity-induced responses. If this were the case it would highlight a potential problem in using acute brain slices for electrophysiology if the slices have their aminergic innervations cut. This complex interaction could be the explanation of conflicting reports concerning the relationship between MeCP2 expression and BDNF expression (Qiu & Cheng, 2010).

Symptomatic female heterozygous RTT mice frequently exhibit characteristic respiratory defects such as apnoea (apnea). Apneas in RTT mice have been associated with NA deficits Viemari et al. (2005). Abdala *et al.*(2010) have used treatment with a combination of GABA reuptake inhibitor and Serotonin 1A agonist to reduce the incidence of apnoea to that of WT mice.

6.6.3 Cell Autonomous Defects in Substantia nigra from Heterozygous Females

Cell autonomous defects have been reported in s*ubstantia nigra* (SN) dopaminergic neurons in MeCP2-ve cells (Gantz *et al.*, 2011). They compared presymptomatic (P16-P30) heterozygous *Mecp2*$^{+/-}$ females with symptomatic (P169-P519) *Mecp2*$^{+/-}$ females and also to age-matched WT mice. Electrophysiology of acute brain slices containing SN neurons revealed differences between MeCP2+ve and MeCP2-ve DA cells. MeCP2 status was determined by *post hoc* immunostaining. There was an age-related decline in electrical capacitance for both Het and WT cells. The capacitance of MeCP2+ve cells was not significantly different to WT in both age groups but MeCP2-ve cells showed a reduced value and were smaller across both age groups. Gantz *et al*.'s (2011) morphological analysis showed a smaller dendritic arbour in MeCP2-ve cells. Input resistance increased with age for both Het+ and WT cells but MeCP2-ve cells had greater input resistance in both age groups. Iontopheric application of dopamine hydrochloride was used to induce D_2 receptor activated outward currents. There was no significant difference between dopamine currents normalised to capacitance in comparisons between WT and MeCP2+ve cells across both age groups. However, the dopamine current was significantly reduced in MeCP2-ve cells from symptomatic females. Gantz *et al*. (2011) also measured dopamine release which was reduced in the symptomatic *Mecp2*$^{+/-}$ mice.

6.6.4 Cortical L5 Pyramidal Neurons

Measurements of up to four synaptically connected cortical L5 pyramidal neurons in acute coronal brain slices from *Mecp2*-null and WT controls were performed by Dani & Nelson (2009). LTP magnitude was similar in P16-P21 null and WT mice. There were also no significant LTP differences in P26-P29 mice but the authors were unable to perform the protocols in older mice. They found no

significant differences in baseline synaptic transmission in 3-4 week old mice. In P26-P29 null mice they observed reduced mean baseline evoked EPSP amplitude for *Mecp2*-null compared to WT for monosynaptic connections between pyramidal cells. Using a train of 5 stimulation pulses at 20Hz there was no significant differences between null and WT controls. However, Dani &Nelson (2009) calculated a reduced quantal content by analysing the inverse square of the coefficient of variation relative to the change in mean EPSP amplitude for the first two EPSPs in the train in null compared to WT. However, quantal properties are known to be highly variable and the variability can arise for a number of different reasons (Stricker *et al.*, 1996; Bekkers & Clements, 1999; Franks *et al.*, 2003; Sargent *et al.*, 2005; Ikeda *et al.*, 2008). Dani & Nelson (2009) did not report the methods or detail of their quantal analysis but stated that GABAergic responses were not blocked. It is possible that non-blocking of GABA could have contributed to the apparent variability in quantal content in null slices, if GABAergic responses were different in null compared to WT. Dani & Nelson (2009) also reported a significantly reduced connection probability (CP) in P26-P29 null compared to WT for pairs of L5 pyramidal neurons (10.1%, WT; 5.3%, null). This suggests that a deficit in MeCP2 could give rise to a reduced excitatory connectivity.

7 Materials and Methods

This section describes the animals, materials, equipment, software, acute hippocampal slice preparation, electrophysiology experiments and other methods used in this study.

7.1 Mice

A colony of transgenic mice was maintained in the University of Glasgow Central Research Facility by breeding male WT Balb/c and female heterozygous *Mecp2*$^{Stop/+}$ mice on a C57BL/6 background (*Mecp2*^{tm2Bird}, Jackson Laboratories stock No. 006849). In the 'stop' mice, one of the endogenous *Mecp2* alleles is silenced by a targeted stop cassette (Guy *et al*. 2007). Litters therefore consisted of a mix of females heterozygous for MeCP2, WT females, hemizygous males and WT males. Only female *Mecp2*$^{Stop/+}$ and *Mecp2*$^{+/+}$ (WT) were used in this study and *Mecp2* genotypes were independently confirmed by standard PCR/gel electrophoresis performed by Dr Shih-Min Weng and as described previously (http://jaxmice.jax.org/protocolsdb/f?p=116:1:2176575767593405; Guy *et al*. 2007)

At the time of weaning (around 21 days) pups were ear punched and moved to separate cages. Ear-punch patterns provided a means of identification and the labelled tissue samples were used as a source of DNA for the PCR genotyping. Ear samples were stored at -20°C prior to the subsequent DNA extraction.

A substantial subset of mice included in this study was bred to express a functional MeCP2- eGFP fusion protein. (*Mecp2*$^{tm3.1Bird}$, Jackson Laboratories stock No. 014610). Male WT MeCP2-eGFP C57/bl mice were mated with female heterozygous *Mecp2*$^{Stop/+}$ mice bred from the above main colony. Female progeny

used were either WT MeCP2$^{eGFP+/+}$ or heterozygous MeCP2$^{eGFP-/+}$. *Mecp2* genotypes were confirmed by standard PCR as above.

All PCR/genotyping was performed independently by Dr Shi-Min Weng, Institute of Neuroscience and Psychology, University of Glasgow.

All mice were housed in littermate groups and maintained on a 12 hour light/dark cycle with food and water *ad libitum*. Experiments were carried out in accordance with the European Communities Council Directive (86/609/EEC) and a project licence with local ethical approval under the UK Animals (Scientific Procedures) Act (1986).

7.2 Solutions

All solutions were prepared using high-purity, double-deionised water. Recording ACSF was freshly prepared on the day of use and consisted of (in mM): NaCl (125), KCl (2.5), $NaHCO_3$ (25.0), NaH_2PO_4.2H2O (1.25), Glucose (25.0), Ascorbate (1.0), Pyruvate (1.0), $MgCl_2$ (1.0) and $CaCl_2$ (2.0). A sucrose-based ACSF was used for slice cutting and acute slice storage, and consisted of (in mM): NaCl (87.0), KCl (2.5), $NaHC0_3$ (25.0), $NaH_2PO4.2H_2O$ (1.25), Glucose (25.0), Sucrose (75.0), Ascorbate (1.0), Pyruvate (1.0), $MgCl_2$ (7.0) and $CaCl_2$ (0.5).

Intracellular pipette solution consisted of (in mM): K Gluconate (130.0), KCl (10.0), $MgCl_2$ (2.0), EGTA (10.0), HEPES (10.0), Na_2ATP (2.0), Na_2GTP (0.3), Na_2Phosphocreatine (1.0), and Biocytin (0.1%). The pH was set to 7.30 and osmolality confirmed to be in the range 300-312mOsm using a calibrated Gonotec Osmomat-030 freezing-point osmometer. The high energy phosphates tend to breakdown in solution at room temperature. Hence these ingredients are added to the aqueous mix last and the solution preparation has to be completed rapidly thereafter. The time from addition of the high energy phosphates to

aliquoting (~1.5mL in Eppendorf tubes) and freezing at -20°C was kept to no more than 20 minutes. Frozen intracellular solution can be kept for several months at -20°C. Aliquots are completely defrosted at 0°C just prior to use in experiments but is kept on ice for the duration.

7.3 Electrophysiology Equipment and Setup

This section lists the equipment hardware used to perform the patch clamping and recording.

7.3.1 Electrophysiology Rig

List of equipment:

Dell PC

Molecular Devices Digidata 1440A Digitiser (ADC/DAC)

Brownlee Precision Model 440 4-channel amplifier and signal conditioner

Molecular Devices Axoclamp 2B current/voltage clamp electrophysiology amplifier

Quest Scientific 'Humbug' 50/60Hz noise eliminators

NPI Electronic TC-20 Temperature Controller

Micromanipulators

Sutter MP-225 micromanipulator with Molecular Devices HS-2A x0.1LU Headstage

Burleigh TS-5000-150 micromanipulator

Burleigh 'Gibraltar' platform and manual X-Y stage (mounted on an anti-vibration table)

Imaging System

Olympus BX50WI microscope with Olympus LUMPlan FI/IR x40 water immersion objective and a x10 or x4 low power objective. The microscope was also fitted with DIC, UV attachment and filters.

Hamamatsu camera head and C2400 analogue camera controller

Hitachi monochrome analogue monitor VM1720K

Miscellaneous

NPI TC-20 inline heating element and temperature controller

Gilson minipuls 3 pump

Digitimer DS2 Isolated Stimulator

World Precision Instruments PM015D pressure monitor

CHY FireMate Company Model 500A K/J Digital Thermometer

7.3.2 Other Specialised Equipment

Leica VT1200S Vibratome

Campden Instruments 752m Vibroslice

Sutter P-97 Flaming/Brown micropipette puller

Fig. 7-1 shows how instruments and devices are interconnected

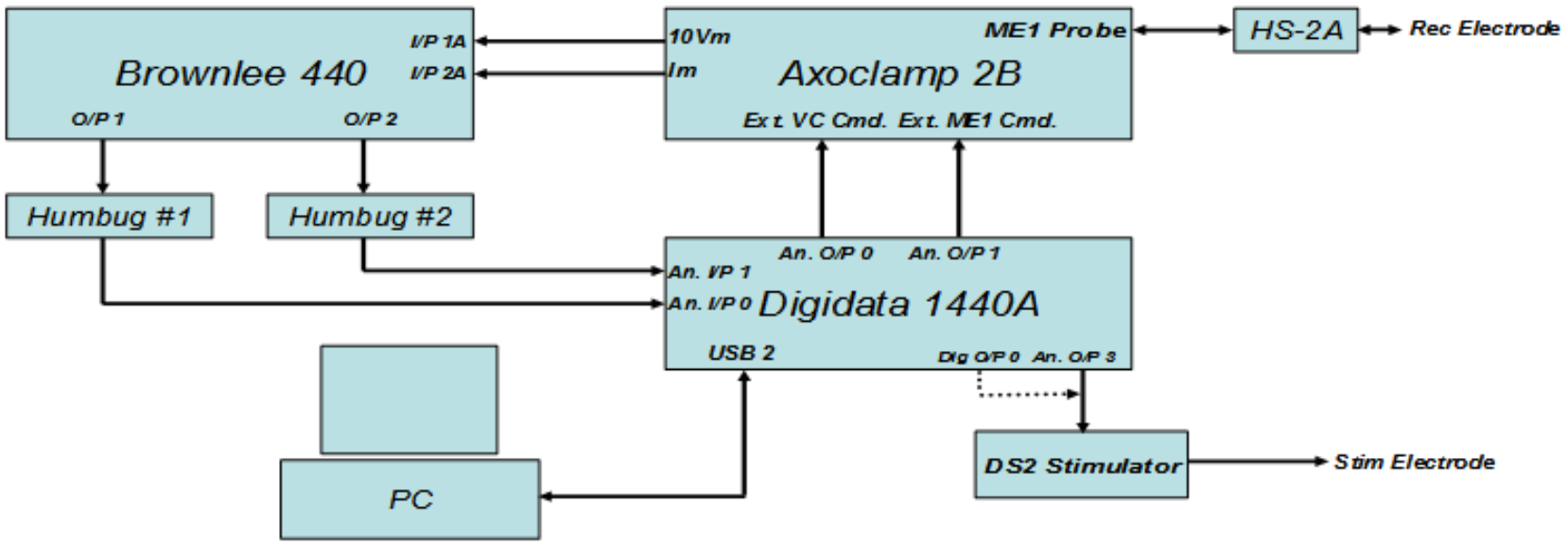

Figure 7-1 Electrophysiology Rig Connections. The recording electrode is mounted on an HS-2A headstage. This connects bidirectionally to an Axoclamp 2B electrophysiology amplifier. A Brownlee 440 amplifier and signal conditioner accepts inputs from the Axoclamp 2B and outputs to the Digidata 1440 A/D digitiser via two Humbugs which attenuate 50Hz interference. Digital inputs to the Digidata 1440 from the PC via a USB connection are converted to analogue outputs which are fed to the Axoclamp 2B. The PC runs pClamp software which is used for recording data and for controlling the Axoclamp 2B. Outputs from the Digidata are also used to control the external stimulation box, DS2.

7.4 Brain Dissection and Slice Preparation

Essentially the method used in all experiments was as described previously by Bischofberger *et al.* (2006) but with the aim of optimising access to the CA1 region. The steps were as follows:

Prior to sacrifice, any mice older than about 40 days were given pure oxygen under slight pressure in a closed tank for about 4 minutes and the animal quickly removed and immediately sacrificed. The oxygen treatment was given as a precaution in case the hippocampi of older mice were more susceptible to ischaemia/hypoxia.

Aliquots of sucrose ACSF were partly pre-frozen by storing at -80°C for approximately 20 mins. The semi-frozen solution was then made into a 'slush' with the aid of a hand-held electric homogeniser. The slush was 'carbogenated' - bubbled with carbogen (95% O_2, 5% CO_2) - for approximately 15 minutes prior to use.

Mice were humanely euthanized by cervical dislocation and in accordance with Schedule 1 of the Animals (Scientific Procedures) Act 1986. Immediately following cervical dislocation the animal was decapitated with a single sharp scissor cut. Holding the head by the snout, the skin was pulled back over the skull and excess flesh cut from the base of the skull to expose the foramen magnum. After entering via the foramen magnum, small lateral scissor cuts were made in the skull either side of the foramen. Then a sagittal cut from caudal to frontal was made starting at the foramen. Finally, medial lateral cuts were

made in the frontal skull plates, just behind the eyes. This procedure allowed the parietal and occipital skull plates to be easily peeled back intact using a pair of curved forceps thus exposing the brain. The brain was cooled *in situ* with oxygenated ice-cold sucrose ACSF from a wide-mouth bulb pipette. This had the advantage of chilling the brain prior to removal and making the brain tissue firmer. The sucrose in the ACSF enabled the solution to have the correct osmolality without a high level of sodium ions. The sucrose ACSF also had low calcium to prevent excitotoxicity. The brain was then removed whole using a small spatula with rounded-tip which was inserted under the brain from rostral to caudal, cutting through the optic nerves and the whole brain gently dropped into ice-cold carbogenated sucrose ACSF prepared from the 'slush'. The time from cervical dislocation to placing the removed brain into the sucrose ACSF was less than a minute in order to minimise hippocampal damage caused by hypoxia. The brain was allowed to cool for approximately 3 minutes and then transferred to a Petri dish which contained sufficient carbogenated ice-cold sucrose ACSF to almost cover the brain.

The brain was then dissected with a pre-cooled scalpel. The cerebellum was cut away then the hemispheres separated with a single, clean sagittal cut through the corpus callosum, ensuring the blade cut vertically through the brain. Each hemisphere was then gently rolled onto its cut side with the aid of a paintbrush. Finally, a 'magic cut' was made tangential to the dorsal surface of each hemisphere so as to remove about 15% of the brain tissue. For optimal access to CA1 pyramidal cells the cut was made at an inward angle of approximately 10 degrees to the lateral plane.

The pre-cooled vibratome cutting base was coated with cooled Superglue (Loctite Precision, Mfr Part No. 577093) on the spots to be used to hold the hemispheres. Each hemisphere was then transferred out of the Petri dish using the flat of the scalpel blade. Excess liquid was removed by briefly contacting the edge of blade to some absorbent tissue. Each hemisphere was then gently

dropped onto the Superglue to firmly adhere them to the base ready for cutting. As soon as the hemispheres were on the glue spots, ice-cold sucrose ACSF was applied to keep them cool and to prevent any excess glue from 'running up' the tissue ensuring no more than 10 seconds elapsed between applications prior to transferring the mounted hemispheres to the cutting bath. The bath held ice-cold oxygenated sucrose ACSF containing sucrose ACSF ice. There was always a mix of sucrose ACSF ice and solution in the bath to ensure the temperature of the hemispheres was not allowed to rise above 0°C. There can be some advantage in gluing then slicing one hemisphere at a time. However, this inevitably would take longer.

The Leica 1200S vibratome was calibrated using a fresh razor blade just prior to use. Any ice crystals in front of the blade were removed using a small paintbrush. 300μm sections were cut but only 3-4 of the sections through the hippocampus proper are usable for recording.

As each section was cut it was turned over. The surface originally on the underside is the best one for whole-cell recording and, once turned, the surface orientation needs to be maintained. The slice was trimmed with a mounted bent hypodermic needle to remove forebrain. It was then transferred to a holding chamber. Holding chambers contained sucrose ACSF bubbled with 'carbogen' (95% O_2, 5% CO_2) and were maintained at 35°C in a water bath. Slices were recovered at 35°C for 30 minutes and then the holding chambers removed from the water bath to room temperature prior to recording.

7.5 Electrophysiology Software

Electrophysiology data acquisition software was used for recording and monitoring of electrophysiology experiments: pClamp v10.2.0.16 (Clampex module for recording). Molecular Devices, Inc. Sunnyvale, Ca. (http://www.moleculardevices.com/Products/Software/pCLAMP.html)

A separate electrophysiology data analysis software package was used for *post hoc* analysis: Stimfit v0.10 open source software by Christoph Schmidt-Hieber (http://code.google.com/p/stimfit).

All software was run on PCs running the Microsoft Windows XP (service pack 3) operating system. Microsoft Corp. USA (www.microsoft.com)

7.6 Electrophysiology Experiments

This subsection describes the procedures used to manage, manipulate and record cells from the prepared acute brain slices.

Acute hippocampal slices (300µm thickness) were individually transferred to the recording chamber with the aid of a wide-mouthed pipette and continually superfused with ACSF saturated with carbogen (95% O_2, 5% CO_2) at a flow rate of 3-4 mL/min. and maintained at a temperature of 30-32°C with the aid of an in-line heater. A temperature of below 37°C was used since acute slices survive better at the slightly lower temperatures (Bischofberger *et al.* 2006). Bath temperature was monitored with a digital thermometer. The ACSF was bubbled with the carbogen via a filter candle for at least 30 minutes prior to the start of an experiment. Slices were held in place in the recording bath using a platinum ring strung with 4-5 teased-out strands of dental floss. The transferred slice was allowed to equilibrate for 10 minutes prior to recording. It is important to

ensure that all sucrose-containing solution is flushed away since the presence of sucrose can create difficulties when patching Bischofberger *et al*. (2006). Slices were visualised using infra-red differential interference contrast (IR-DIC) microscopy with Köhler illumination supported by a video camera and monitor. This gives improved resolution (Stuart *et al*. 1993). The microscope with recording bath and micromanipulators are mounted on an anti-vibration table which is pumped-up with compressed air just before starting experiments. Pre-washed borosilicate glass capillary pipettes (2mm outside diameter, 1mm inside diameter, Hilgenberg, GmbH) were pulled to give a tip diameter of approximately 1µm which corresponded to a resistance in the range 2.5-3.5MΩ in use. Recording electrodes were backfilled with intracellular solution containing 0.1% Biocytin, and stimulus pipettes filled with 2M NaCl. A fresh recording pipette was used for each patch clamp attempt. Silver electrode wires were chlorided electrolytically daily prior to the start of experiments. A stimulus pipette was positioned just below the slice surface in the *stratum radiatum* close to CA1, towards CA3 and in close proximity to the Schaffer collaterals. Putative pyramidal cells were visually identified, usually at the border of the *stratum pyramidale* and *stratum oriens* and at a depth of between 20-50 µm below the surface. Although somas are more visible just below the surface it is likely that such cells have severed dendrites as a consequence of the cutting process. Below 50 µm cells are less distinct and harder to patch. The intracellular solution in the recording pipette was maintained under slight internal pressure with the aid of a syringe, three-way taps and flexible tubing connected to the pipette holder. Immediately before entering the recording bath the pressure was set to approximately 0.4psi (28mbar). This prevented any debris from blocking the pipette tip and aided bringing the pipette tip towards a target cell by clearing the way ahead. On the Axoclamp 2B amplifier and in voltage clamp the input offset control, bridge control and holding position control were all set to 0V at start. The pClamp/Clampex membrane test program module was run and the pipette tip lowered into the bath. The membrane test generates a train of 5mV, 20ms square pulses and the timebase was adjusted to display a single such pulse on the screen. The input offset control was adjusted to give a Vm of 0V with the pipette fully immersed. This was to zero the pipette

tip potential. The pipette tip resistance was measured in voltage clamp and the value recorded.

As a target cell was approached the pressure was increased to approximately 0.7 psi and the higher pressure creates a small dimple in the cell membrane. The pressure was then released. At the same time the holding position was adjusted to apply approximately -20mV. This aids seal formation. Sometimes applying a slight negative pressure through very gentle sucking also helps seal formation. If the seal-formation is successful, a tight gigaohm seal (>1 GΩ) should form at the soma with the tip of the recording electrode. Simultaneously the holding potential can be quickly but smoothly adjusted down to -65mV. The square wave collapses as a consequence of the very high resistance, and fast capacitative transients caused by the pipette capacitance are seen at what were the leading and trailing edges of the square wave. At this point, the pipette capacitance was compensated by adjusting the Axoclamp 2B capacitance neutralisation control. The aim is to minimize the amplitudes of the transient spikes but this has to be done carefully in order to avoid electronic oscillation in the headstage which could destroy the seal/cell.

Breakthrough of the cell-attached configuration was achieved through several short negative pressure pulses generated by a very gentle sucking action in order to rupture the cell membrane. Once a whole-cell configuration is achieved large capacitative transients with a relatively slow decay are displayed. In whole-cell mode, the resting membrane potential (V_m) of the cell was measured together with access resistance (Rs). Cells were only recorded if the initial V_m was less than -50mV and Rs < 30MΩ. Capacitance and series resistance were compensated as far as possible. Signals were sampled at 20kHz and low-pass (Bessel) filtered electronically via the Axoclamp 2B and again via the Brownlee 440 signal conditioner, both using a 10kHz cut-off. Additionally a 1Hz high-pass filter was employed via the Axoclamp 2B. 'Humbug' 50Hz filters were positioned between the output of the Brownlee 440 and the analogue input of the DigiData 1440a

data acquisition unit.

In current clamp, cells were injected with a series of hyperpolarising and depolarizing 500ms duration current pulses in the range -250 to +250pA, step 50pA, and which elicited action potentials above threshold. Analysed recordings (average of 3) were used to construct I-V graphs and tables of passive and active intrinsic parameters. A second current clamp protocol consisted of a -10pA, 500ms pulse. The voltage response averaged over 30 pulses was used to calculate input resistance and membrane time constant (Tau).

In voltage clamp, external stimulation via a DS2 external isolated stimulator was used to evoke postsynaptic current responses under the control of several protocols: variable interval paired stimulation pulses (25-500ms pulse intervals) were used to measure paired pulse facilitation (PPF) and variable frequency stimulus pulse trains (10 pulses across each of ranges 5-40Hz) for frequency facilitation. Voltage clamp protocols incorporated a 5mV, 25ms test pulse injection after the stimulation pulses and which was used to monitor Rs.

The DS2 was triggered via software control using protocols written with pClamp. A stimulus pipette, connected to the stimulation box, was placed just under the slice surface in the *stratum radiatum* in order to contact the Schaffer Collaterals orthodromically. Membrane potential was held at -65mV. Paired pulse interstimulus intervals were 25, 50,100, 200 and 500ms. Trains of 10 frequency facilitation protocol pulses were at 5, 10, 20 and 40Hz. Stimulus intensity was adjusted so as not to saturate the response. The external stimulus box control was first adjusted to just elicit a response to the first pulse and then the stimulus intensity was increased in order to obtain robust paired-pulse facilitation with the 25ms interval. This setting was not altered between applications of the two protocols for the same cell. In both protocols at least 10 traces were recorded at each interval or frequency with 10 seconds between traces to allow for recovery. At time of analysis the average of the 10 traces was

taken. All the cell types exhibited facilitation with both protocols. Hand drawn diagrams were made showing the orientation of the slice and approximate location of the recorded cell. This was to facilitate location of the recorded cell when it was later examined under fluorescence microscopy. Figure 7-2 illustrates an example of a sketch of a slice. It shows the approximate locations of the stimulation and recording electrodes as seen under low power in A) and the orientation of the slice as seen by eye in B).

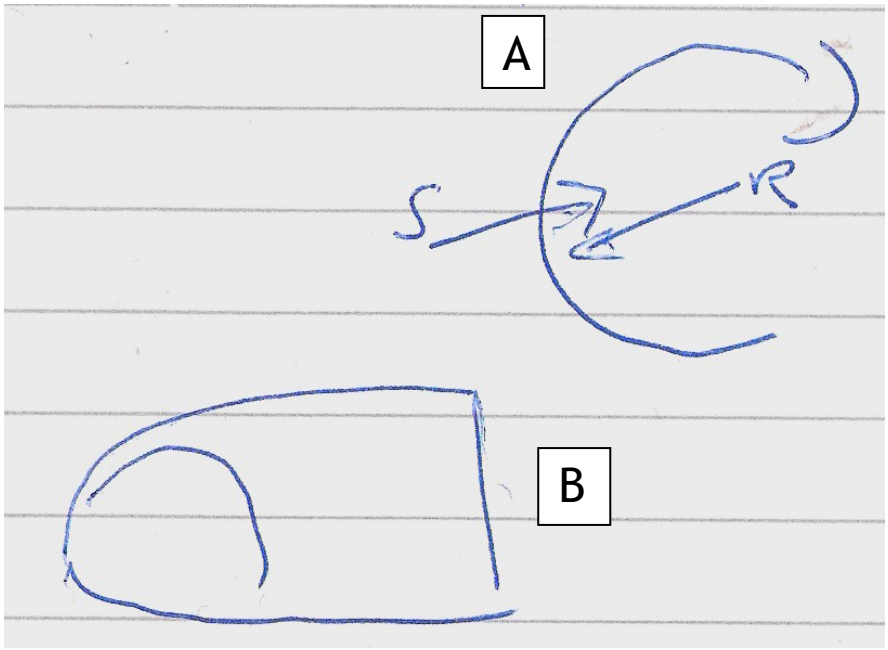

Figure 7-2 Example of sketch of recorded hippocampal slice (taken from Lab Book). **A**) shows the appearance of the slice under lower power where 'S' and 'R' denote the approximate positions (in the CA1) of the stimulation and recording electrodes, respectively. The curve at top right represents the dentate gyrus. **B**) is a sketch of the slice as seen by the naked eye and shows the orientation of the slice.

After all recordings of a cell were completed, an outside-out patch was formed. This was to ensure that the membrane of the recorded cell was sealed so that the cell remained viable prior to fixing. The outside-out patch was achieved by gradually and carefully withdrawing the pipette in a combined horizontal and upward direction using the micromanipulator whilst monitoring the membrane

test display. As soon as the cell started to reseal, as evidenced by the collapse of the capacitative transients, the holding potential was increased to -40mV and the pipette could then be fully retracted. After experiments the slice was removed from the recording bath with a wide-mouthed pipette and placed in a vial containing oxygenated ACSF. With a minimum of carry-over, the slice was then rapidly transferred to 4% formaldehyde in 0.1M PB kept at 4°C again using a wide-mouthed pipette. It was found that improved MeCP2 immunostaining was obtained if fixation time was limited to ~1-4hr. After this fixation period slices were transferred to 0.1M PB containing 0.05% sodium azide as a preservative and stored at +4°C.

Examples of Clampex recording protocols can be found in Appendix 1.

7.7 Immunohistochemistry

Hippocampal slices were prepared for fluorescence microscopy by immunostaining with appropriate combinations of primary and secondary antibodies.

The primary antibodies used were:

1) Polyclonal rabbit anti-MeCP2 (Millipore, cat no. 07-013)
2) Monoclonal mouse anti-NeuN (Millipore, cat no. MAB377)

Secondary Antibodies used were:

1) Goat anti-rabbit Alexafluor 488 (Invitrogen, cat no. A-11008)
2) Goat anti-mouse Alexafluor 546 (Invitrogen, cat no. A-11030)
3) Streptavidin Alexa Fluor 647 conjugate (Invitrogen, cat no. S21374)

Stock primary and secondary antibody solutions were made up as per the suppliers' instructions at a concentration of 1mg/mL in 0.1MPB, pH 7.3. The working primary and secondary antibodies were used at a 1:500 dilution of the stocks. The Avidin-647 was used at a dilution of 1:1000 of the stock.

The steps for primary and secondary immunostaining of the fixed hippocampal slices were as follows:

Primaries:

1) 3 x 20min washes in 0.1M PB
2) 3 x 15min washes in 0.1M PBS
3) Blocking for 1 hour at RT. The blocking solution contained 10% normal goat serum (NGS), 0.3% Triton X100, 0.05% sodium azide made up to a working volume with 0.1M PBS.
4) Application of primary antibodies for 1 hour at RT and then for 2-3 days at +4°C. The working solution consisted of 5% NGS, 0.3% Triton X-100, 0.05% sodium azide, primary antibody, and made up to volume with 0.1M PBS to give a final primary antibody concentration of 1:500. Slices were in multi-well plates sealed with Parafilm to prevent evaporation.
5) 4 x 20min rinses in 0.1M PBS then

Secondaries:

6) Application of secondary antibodies overnight at +4°C then for 1 hour at RT. Working solutions consisted of secondaries, 3% NGS, 0.1% Triton X-100, 0.05% sodium azide made up to volume with 0.1M PBS.
7) 1 x 15min rinse in 0.1M PBS
8) 2 x 20min rinses in 0.1M PB
9) 1 x 90min rinse in 0.1M PB

Slices were mounted under cover slips on glass microscope slides with Vectashield™ mounting medium and the cover slips sealed with an opaque nail varnish. In some cases either the mounting medium used contained a DAPI nuclear stain or the final rinse contained DAPI. Immunostaining protocols varied according to mouse genotype. For most WT mice the presence of MeCP2 was assumed, so primary anti-MeCP2 and corresponding secondary were not used. Similarly, in the case of slices from MeCP2-eGFP mice there was no requirement to immunostain for MeCP2. Prepared slides were wrapped in foil and stored in the dark at +4°C short-term and -20°C long-term.

High power (x40 obj.) images were used to confirm the recorded cell's MeCP2 status either from Alexa Fluor 488 nuclear staining or from the presence of nuclear MeCP2-eGFP.

7.8 Confocal Imaging

Slices were subsequently imaged on a laser-scanning confocal fluorescence microscope (Bio-Rad Radiance 2100, LaserSharp 2000 software). Recorded cells were filled with Biocytin and hence cytoplasmically marked with the Alexa Fluor 647 conjugate. These cells were located initially at x10 and then using a x20 objective. In general, a triple channel method was used which allows control of power output of each of the three lasers (Green λ = 488nm, Red λ = 543nm, and far red λ = 637nm). The far-red channel was pseudocoloured blue. To facilitate the location of a recorded cell the 488nm and 543nm channels were initially switched off and only the 637nm photomultiplier used. Low power (x20 obj.) triple label method images were then obtained to gauge the overall morphology and confirm the cell type of Biocytin filled cells. Image stacks using 5μm steps at 166lps scanning speed were prepared starting from just below to just above the soma of the cell of interest. This was achieved by employing the automated Z-series acquisition focus motor option. Lambda strobing which sequentially

excites the target line by line with each individual laser source was employed to prevent bleed-through. In general, the minimum laser intensity was used that gave a sufficiently bright image for each wavelength whilst minimising bleaching. The auto iris optimisation control was used to get the best laser iris adjustment. Gain and offset were manually adjusted to give the best brightness and contrast. High power (x40 oil immersion objective) images were used to confirm the recorded cell's nuclear MeCP2 status either from Alexa Fluor 488 nuclear staining or from the presence of nuclear MeCP2-eGFP. In this case Z-series image stacks were obtained with 1 or 2µm steps. Image stacks acquired for neuronal reconstruction purposes were made at x20 and using a 1µm step. In some cases the separate blue laser diode option (405nm) was used for exciting DAPI which enabled imaging of all cell nuclei.

7.9 Statistical Analyses

Three standard statistical tests were performed according to the type of data sets being compared. A t-test was used to compare the means of two groups to determine whether they came from the same sampling distribution of means. This was an appropriate test to compare mean values of a parameter between two groups of data such as, for example, WT and the combination of MeCP2+ve and MeCP2-ve. Analysis of variance (ANOVA) was used to compare the means of two or more groups to determine whether they arose from the same sampling distribution. This was an appropriate test to compare mean values of a parameter between three groups of data such as WT, MeCP2+ve and MeCP2-ve. Multivariate analysis of variance was used to compare two or more vectors of means to determine whether they came from the same sampling distribution. This was an appropriate test to use where the data could be treated as a vector of values such as that derived from the multiple data points across paired-pulse stimulation intervals and also for the frequency facilitation data which consisted of values obtained from trains of 10 stimuli. Most of the statistical analyses were performed using GraphPad Prism v5.03 (GraphPad Software Inc., CA, USA)

running under Microsoft Windows 7. This package was also used for producing the data graphs. The MANOVAs of the synaptic data involving vectors (PPF and Frequency Facilitation) were performed with the open-source ‘R‘ programming environment (http://www.r-project.org/) using the 2.14.0 version. External library packages were downloaded via the Comprehensive R Archive Network (CRAN). The other analyses using GraphPad Prism were either one-way ANOVA or t-tests.

Statistical tests usually assume that data belongs to a Gaussian distribution and that variances are equal. With the ‘R’ analyses testing for normality was performed using an Anderson-Darling algorithm. Data sets which failed the test for normality were corrected by applying a Yeo-Johnson power transform followed by re-testing for normality. With the GraphPad Prism analyses normality and variance testing (Bartlett’s test for equal variances) was performed using the built-in column statistics option together with post hoc comparisons, e.g. Tukey’s Multiple Comparison Test. Where necessary, appropriate transforms were applied to the data in order to achieve normality and equality of variance. In some cases, data sets were skewed by the presence of one or more outliers. Identified outliers were excluded from analyses. Where normality and equality of variance could not be achieved non-parametric analyses were applied. Statistical comparisons were made between data from WT, HetP and HetN cells treating them as three groups. Additionally, comparisons were made between the composite of WT + HetP cells with HetN cells and also between WT and the composite of HetP + HetN cells.

Significance was based on an alpha of 0.05 and this metric was used throughout. Also, ‘p-values’ are reported to 2 decimal places.

8 Results

The purpose of the study was to first measure the passive and active intrinsic properties of individual CA1 pyramidal neurons from heterozygous *Mecp2*$^{Stop/+}$ mice and WT mice controls using the whole-cell patch clamp technique. The short-term plasticity characteristics and evoked synaptic properties of the same cells were then also measured as part of the same experiment. All recorded cells were filled with Biocytin and post-hoc stained with Avidin-647. This enabled all recorded cells to be imaged and confirmed as pyramidal type through their morphology and location in the CA1 region using laser-scanning confocal microscopy at 637nm. The MeCP2 status of cells from *Mecp2*$^{Stop/+}$ mice were identified using either post-hoc immunostaining of MeCP2 or by using the presence/absence of MeCP2-eGFP when viewed under the confocal microscope at 488nm. This enabled the recorded data to be classified, analysed and subjected to statistical tests in order to identify any significant differences between WT, MeCP2+ve and MeCP2-ve cells. Although the acquired data is limited, it is the first study which compares the intracellular and evoked synaptic properties of individual identified MeCP2+ve and MeCP2-ve CA1 pyramidal cells in the *Mecp2*-mosaic hippocampus. The data provides a baseline for further study and complements other studies performed using extracellular recording techniques and studies which have examined *Mecp2*$^{+/-}$ cells in other brain regions or in cell culture.

A total of 14 cells from WT mice and 32 cells from *Mecp2*$^{Stop/+}$ mice were recorded. Of the 32 cells from the *Mecp2*$^{Stop/+}$ mice, 10 were deemed positive for MeCP2 and 12 were deemed negative for MeCP2. Unfortunately, the MeCP2 status of the remaining 10 cells from *Mecp2*$^{Stop/+}$ mice (non-eGFP) could not be assigned a MeCP2 status with certainty because of poor immunostaining and had to be excluded from the analysis. A few other cells were recorded but were identified as non-pyramidal cell types so were also excluded. Pyramidal cell type identification was confirmed based on: A) Soma position, i.e. in or close to the

pyramidal layer. B) Soma shape i.e. triangular when stained. C) Dendritic morphology: a basal dendritic tuft in the *stratum oriens* comprising 3-5 main dendrites. A single, thick apical dendrite is present which may bifurcate in the *stratum radiatum*, and which extends into the *stratum lacunosum-moleculare*. A variable number of oblique dendrites are also seen in the *stratum radiatum*. D) If visible, a single axon, which may show subsequent branching, projecting into the *alveus*. E) Under high power a high density of dendritic spines are visible. See Fig.3-4 earlier and reference Megias *et al*. (2001).

8.1 Number and Age of Mice Used in Experiments

8.1.1 Onset of Symptoms and Phenotypes of Mecp2$^{stop/+}$ Mice

Guy *et al*. (2001) and Guy *et al*. (2007) have reported the phenotype progression in RTT mice. Heterozygous female mice start developing RTT-like symptoms across a wide time span of 4 to 12 months of age which overlaps with Rett syndrome. By 9 months of age about half of a cohort will show unambiguous symptoms. These include hind limb clasping, inertia, breathing difficulties, tremor, abnormal gait, and general condition. Some female RTT mice are also observed to become obese. The heterozygous female phenotype progression contrasts with that of Mecp2-null males where overt symptom onset occurs at approximately 6 weeks of age with death inevitable by at most 20 weeks with most dying at 12-15 weeks. Guy *et al*. (2007) developed a formal method of symptom score profiling (based on symptom absent, present or severe). However, whether or not a particular mouse shows RTT symptoms can sometimes be difficult to judge. In the absence of overt symptoms the judgment of whether or not a mouse is symptomatic requires skill and experience, and needs to be performed by a third party in order to avoid experimental bias. In this study the majority of mice used belonged to a pre-symptomatic age group and formal symptom assessment was not carried out. None of the older mice used exhibited any overt symptoms such as hind-limb clasping.

8.1.2 Selection of Mice

Ideally, it is recommended to use age-matched littermates and WT controls in experiments. However, because of breeding difficulties this was not possible. Table 8-1 lists the summary numbers and ages of the mice and cells used. In general there was one cell from each animal but in some cases more than one cell from the same animal was used. 'HetP' is used as a label for cells from heterozygous mice that were determined to be positive for MeCP2. Similarly, 'HetN' is used for MeCP2-ve cells. The age data are plotted as a scatterplot in Fig. 8-1. There was one Het mouse aged 302 days that clearly stands out. However, performing a non-parametric two-tailed t-test does not show an overall significant difference in mice ages (Mann-Whitney, p=0.11). Excluding the 302-day Het mouse does not make a great difference (Mann-Whitney, p=0.17). There were another 4 Het mice which were aged between 124-149 days. Excluding those mice from the age analysis changes the p-value to 0.75. Similarly, comparing the ages of Het-derived cells does not give a significant difference between HetP and HetN (Mann-Whitney, p=0.11). It is noted that although age differences between genotypes are not statistically significant, p-values are nevertheless quite low.

	WT mice	Het mice	WT cells	HetP cells	HetN cells
Total number	14	18	14	10	12
Min. age (days)	33	32	33	35	32
Max. age (days)	63	302	63	125	302
Median age (days)	42	59.5	42	49.5	114
Mean age (days)	45.1	82.5	45.1	62.5	126

Table 8-1 List of the summary age data of mice/cells used in experiments

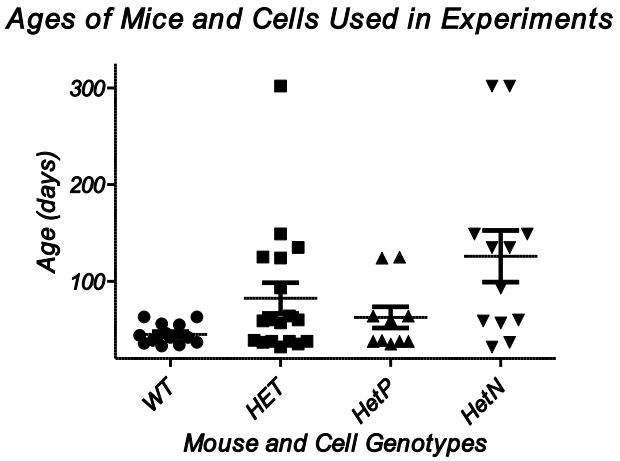

Figure 8-1 Scatter plot comparing mice/cell ages by genotype. The heterozygous cohort includes 4 mice with ages in the range 124-149 days, and 1 mouse aged 302 days. However, a non-parametric test indicates no significant difference in median age between the groups (Mann-Whitney, p=0.11). Similarly there is no significant difference between the ages of HetP compared to HetN cells (Mann-Whitney, p=0.11)

In a previously published study, comparisons between the intrinsic electrophysiological properties of mouse CA1 pyramidal cells from young adult (11-17 weeks) and older (76-110 weeks) sample groups showed a significant difference only in respect of a modest increase in AHP amplitude in the older animals. There were no significant differences observed in other intrinsic properties (Shelbourne *et al*. 2007). Ageing effects on LTP and LTD have been reported for rat CA1 but that study classified young adults as 1-12 months and aged ones as 22-24 months (Kumar *et al*. 2007).

Hence, since the oldest mouse in this study was less than 44 weeks, it is not thought that the age of mice used in this study would have an impact on electrophysiological properties independent of MeCP2-deficiency.

In summary, there were 14 cells from 14 WT mice, 10 HetP cells from 9 animals and 12 HetN cells from 9 animals (18 heterozygous animals total). Since it was not always possible to maintain cell/slice viability there were fewer cells recorded with synaptic protocols compared to intrinsic measurements.

8.2 CA1 Pyramidal Neurons - Passive and Active Intrinsic Properties

Putative pyramidal cells were chosen which were either in the CA1 pyramidal layer or in the *stratum oriens* and closely proximal to the pyramidal layer. Individual cells were subjected to whole-cell patch clamp and the passive membrane properties recorded and a diagram made showing the approximate location of the recorded cell.

The active intrinsic properties were obtained through the current-clamp injection of 500ms duration hyperpolarizing and depolarizing current steps. These were in the range -250pA to +250pA with a step value of 50pA. The range chosen was observed to give a robust response. The procedure was repeated 3 times to give 3 sets of voltage responses from which intrinsic parameter mean values could be calculated via analysis in Stimfit. Summary mean values ±SEM for all intrinsic parameters by cell type are given in Table 8-2. For each parameter the mean ±SEM was plotted graphically and the raw intrinsic data was analysed statistically to see whether any differences could be detected between cell types.

Some representative examples of current-clamp responses in individual cells can be found in Appendix 2.

The peak and steady state responses at each hyperpolarizing current step were used to obtain the current-voltage values which were plotted on graphs. The plots gave good straight line fits for both steady state and peak measurements. The slopes were different between steady state and peak, with peak values

giving a steeper slope as a consequence of I_h ('sag'). This was true across all three cell types (WT, HetP, HetN).

Intrinsic properties:	Wild type	HetP	HetN
Resting membrane potential (mV)	-61.7 ± 1.6	-60.8 ± 1.4	-62.2 ± 1.92
Input resistance (MΩ)	125.8± 10.6	143.8 ± 14.3	159.1 ± 13.1
Membrane time constant (ms)	31.4 ± 2.5	26.7 ± 1.8	26.4 ± 3.0
AP Threshold (mV)	-37.7 ± 0.7	-36.6 ± 1.5	-38.1 ± 1.1
AP Amplitude (mV)	84.2 ± 2.7	83.6 ± 1.7	86.4 ± 1.9
AP 20-80% rise time (ms)	0.077± 0.005	0.077 ± 0.004	0.086 ± 0.004
AP ½ height duration (ms)	1.04 ± 0.06	1.05 ± 0.02	1.15 ± 0.06
AP Maximal rise rate (mV/ms)	586.5 ± 24.5	583.6 ± 25.5	546.1 ± 39.4
AP Maximal decay rate (mV/ms)	106.0 ± 4.9	101.1 ± 3.3	97.3 ± 4.3
Medium AHP amplitude (mV)	-10.2 ± 0.8	-9.4 ± 0.7	-10.2 ± 0.8
Peak I-V Slope (mV/pA)	0.117 ± 0.007	0.129 ± 0.010	0.145 ± 0.013
Steady State I-V Slope (mV/pA)	0.099 ± 0.006	0.098 ± 0.006	0.114 ±0.007
Max AP Discharge Rate (Hz)	33.1 ± 3.1	35.8 ± 2.9	35.3 ± 3.3
Frequency-Current Slope	0.136 ± 0.006	0.138 ± 0.003	0.145 ± 0.008

Table 8-2 Summary of key biophysical properties for WT, heterozygous MeCP2+ve (HetP) and heterozygous MeCP2-ve (HetN) pyramidal cells in hippocampal area CA1. The values for I-V slopes differ from the values for input resistance since the latter is based on a -10pA pulse injection. All values are mean ± SEM. WT n= 12-4, HetP n=9-10, HetN n=11-12.

From the Stimfit analysis the relationship between depolarizing current step and action potential discharge frequency was also obtained and plotted. The frequency in Hz was simply calculated by multiplying the number of action potentials counted during the injected 500ms current pulse for each step between 0pA and +250pA. The maximum AP frequency was the discharge rate at +250pA. Linear regression was used to obtain the slopes of the summary frequency-current plots.

The voltage response to a -10pA current step was also obtained, and in this case 30 traces were recorded in order to construct an average trace which would

smooth out the inevitable noise at this low level. The averaged -10pA current step recording was used to obtain the resting input resistance via Ohm's Law and also to ascertain the membrane time constant (Tau) via curve fitting of the rising edge using Stimfit. Current-voltage slopes also return a value which expresses input resistance. However, the -10pA method was preferred since it causes a negligible inward rectification and measures the change in membrane resistance from rest. A monoexponential curve was fitted and this was done by estimating the time taken for the curve to decay by approximately 63% i.e. the time taken to decay to 1-1/e of its final value. The estimated value is used to place a second cursor which marks the region of the curve to fit the monoexponential.

The statistical analysis for each intrinsic parameter is presented below.

8.2.1 Intrinsic Properties – Resting Membrane Potential (RMP)

Fig. 8-2 shows the plot of RMP ±SEM values for each cell type. There was no purpose in applying any statistical analysis to RMP data since cells were selected such that RMP was within tight limits, hence mean values ±SEM were very similar (WT -61.7 ± 1.6mV, HetP -60.8 ±1.3mV, HetN -62.2 ± 1.84mV).

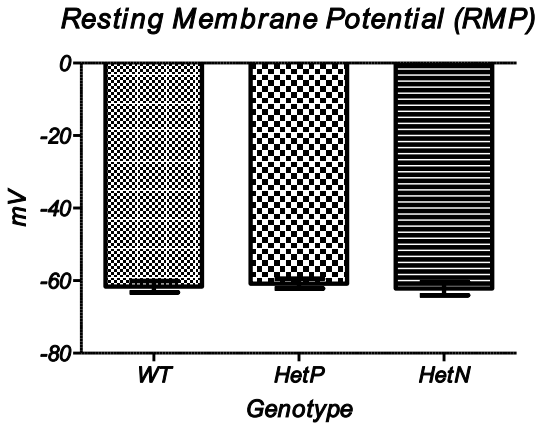

Figure 8-2 Plot of mean RMP ±SEM for each cell type. Resting membrane potentials are very similar across cell types. (WT n=14, HetP n=10, HetN n=12)

8.2.2 Intrinsic Properties – Input Resistance

Fig. 8-3 shows plots of mean values of input resistance in megohms ±SEM for each cell type and grouped data for WT+HetP and HetP+HetN. The data passed the D'Agostino and Pearson normality test ($p>0.05$) and groups had similar coefficients of variation. There were no significant differences between cell types (one-way ANOVA, $p=0.16$ with Tukey's post hoc comparisons ($p>0.05$) or grouped data unpaired t-tests, $p>0.05$). Table 8-3 summarises the analysis. It is noted that, although not significant, p-values were quite low. This was attributed to the Het cells mean input resistances being slightly higher than WT. Mean values ±SEM were WT 125.8 ± 10.6MΩ, HetP 143.8 ± 14.3MΩ, HetN 159.1 ± 13.1MΩ.

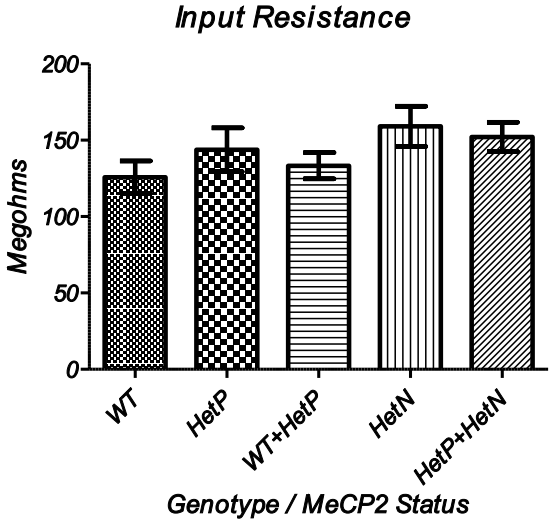

Figure 8-3 Plot of mean input resistance ±SEM for each cell type and comparisons include WT+HetP and HetP+HetN. There were no significant differences between groups ($p>0.05$ for all comparisons)(WT n=14, HetP n=10, HetN n=12)

Table 8-3 Input resistance statistics. (WT n=14, HetP n=10, HetN n=12)

Comparison	ANOVA/t-test	F-test	Bartlett's	Tukey	Sig.
WT v HetP v HetN	p=0.16		p=0.87	p>=0.05	ns
(WT+HetP) v HetN	p=0.10	p=0.72			ns
WT v (HetP+HetN)	P=0.08	p=0.65			ns

8.2.3 Intrinsic Properties – Membrane Time Constant

Fig. 8-4 shows plots of the mean membrane time constant for each cell type and grouped data. The data passed the D'Agostino and Pearson normality test but there was unequal variance caused by the HetN data. Inspection revealed an unusually low value of 11.47ms and this was treated as an outlier and removed. Mean values ±SEM were WT 31.4 ± 2.5ms, HetP 26.7 ± 1.8ms, HetN 26.4 ± 3.0ms. There were no significant differences between cell types (one-way ANOVA, p=0.29 with Tukey's post hoc comparisons (p>0.05) or grouped data unpaired t-tests, p>0.05). Table 8-4 summarises the analysis.

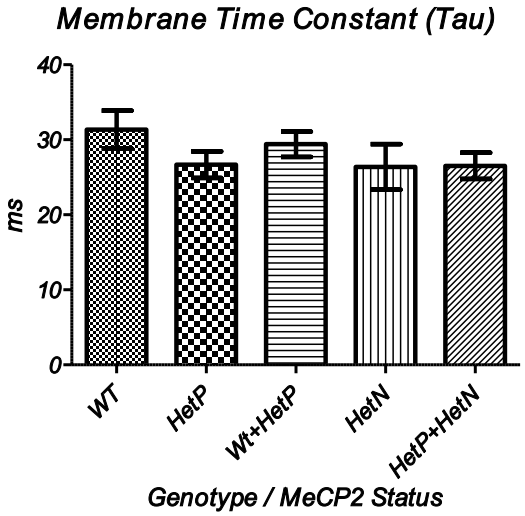

Figure 8-4 Plot of mean membrane time constants ±SEM for each cell type and comparisons include WT+HetP and HetP+HetN. An outlier was excluded from the HetN data. There were no significant differences between groups (p>0.05 for all comparisons) (WT n=14, HetP n=10, HetN n=11)

Table 8-4 Membrane time constant statistics (WT n=14, HetP n=10, HetN n=11)

Comparison	ANOVA/t-test	F-test	Bartlett's	Tukey	Sig.
WT v HetP v HetN	p=0.29		p=0.20	p>0.05	ns
(WT+HetP) v HetN	p=0.36	p=0.41			ns
WT v (HetP+HetN)	P=0.11	p=0.51			ns

8.2.4 Intrinsic Properties – Action Potential Threshold

Fig. 8-5 shows plots of the mean action potential threshold values for each cell type and grouped data. The data did not initially pass the D'Agostino and Pearson normality test. Both the HetN and HetP datasets contained unusually low threshold values of -53.36mV and -47.44mV respectively. Both values were deemed outliers and excluded. The data then passed the normality test and coefficients of variation were not significantly different. Mean values ±SEM were WT -37.7 ± 0.7mV, HetP -36.6 ± 1.5mV, HetN -38.1 ± 1.1mV.There were no significant differences between cell types (one-way ANOVA, p=0.61 with Tukey's post hoc comparisons (p>0.05) or grouped data unpaired t-tests, p>0.05). Table 8-5 summarises the analysis.

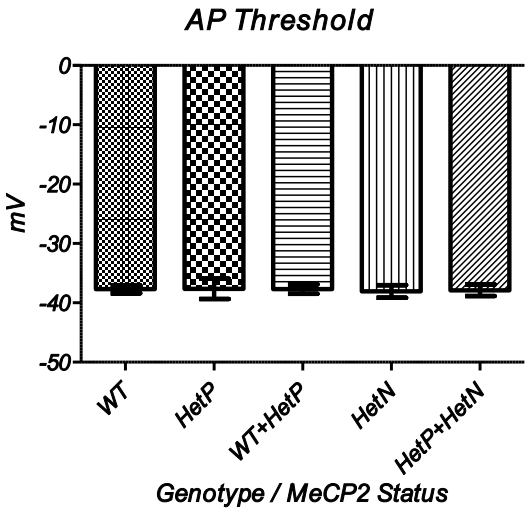

Figure 8-5 Plot of mean membrane time constants ±SEM for each cell type and comparisons include WT+HetP and HetP+HetN. Outliers were excluded from the HetN and HetP data. There were no significant differences between groups (p>0.05 for all comparisons) (WT n=14, HetP n=9, HetN n=11)

Table 8-5 Action potential threshold statistics (WT n=14, HetP n=9, HetN n=11)

Comparison	ANOVA/t-test	F-test	Bartlett's	Tukey	Sig.
WT v HetP v HetN	p=0.61		P=0.22	p>=0.05	ns
(WT+HetP) v HetN	p=0.77	p=0.78			ns
WT v (HetP+HetN)	P=0.81	p=0.12			ns

8.2.5 Intrinsic Properties – Action Potential Amplitude

Fig. 8-6 shows plots of the mean action potential amplitude values for each cell type and grouped data. Although the data passed the D'Agostini and Pearson normality test ($p>0.05$) there was some inequality of variances. The WT group included an amplitude value of 102.55mV which was deemed an outlier and excluded from the analysis improving the variance between groups. Mean values ±SEM were WT 84.2 ± 2.7mV, HetP 83.6 ± 1.7mV, HetN 86.4 ± 1.9mV. There were no significant differences between cell types (one-way ANOVA, $p=0.44$ with Tukey's post hoc comparisons ($p>0.05$) or grouped data unpaired t-tests, $p>0.05$). Table 8-6 summarises the analysis.

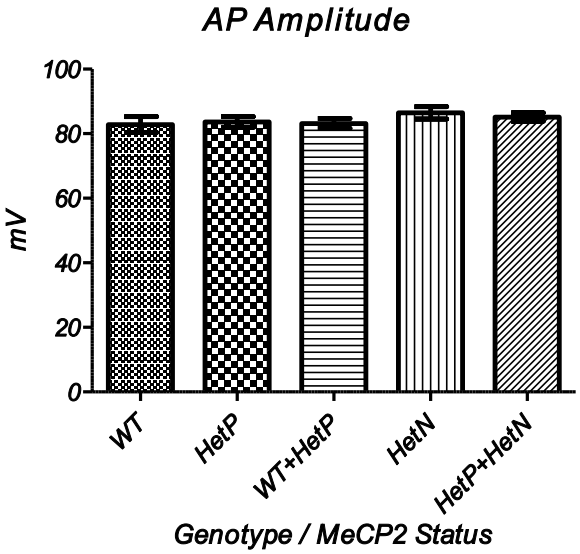

Figure 8-6 Plot of mean action potential amplitudes ±SEM for each cell type and comparisons include WT+HetP and HetP+HetN. An outlier was excluded from the WT data. There were no significant differences between groups ($p>0.05$ for all comparisons) (WT n=13, HetP n=10, HetN n=12)

Table 8-6 Action potential amplitude statistics (WT n=13, HetP n=10, HetN n=12)

Comparison	ANOVA/t-test	F-test	Bartlett's	Tukey	Sig.
WT v HetP v HetN	p=0.44		0.25	p>=0.05	ns
(WT+HetP) v HetN	p=0.21	p=0.72			ns
WT v (HetP+HetN)	P=0.37	p=0.12			ns

8.2.6 Intrinsic Properties – Action Potential 20-80% Rise Time

Fig. 8-7 shows plots of the mean action potential 20-80% rise time values for each cell type and grouped data. The data initially failed the D'Agostino and Pearson normality test. The WT group included two rather large values of 0.12ms and 0.17ms which were deemed outliers and excluded. The HetN group included a large value of 0.17ms and this was also excluded. The data sets were then transformed logarithmically and subsequently passed tests for normality and variance. Mean values ±SEM were WT 0.077 ± 0.005ms, HetP 0.077 ± 0.004ms, HetN 0.086 ± 0.004ms. There were no significant differences between cell types (one-way ANOVA, p=0.24 with Tukey's post hoc comparisons (p>0.05) or grouped data unpaired t-tests, p>0.05). Table 8-7 summarises the analysis.

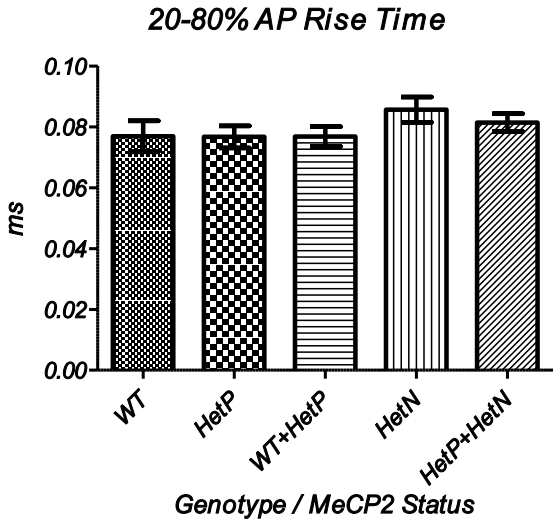

Figure 8-7 Plot of mean action potential 20-80% rise time ±SEM for each cell type and comparisons include WT+HetP and HetP+HetN. Outliers were excluded from the WT and HetN data. There were no significant differences between groups (p>0.05 for all comparisons) (WT n=12, HetP n=10, HetN n=11)

Table 8-7 Action potential 20-80% rise time statistics (WT n=12, HetP n=10, HetN n=11)

Comparison	ANOVA/t-test	F-test	Bartlett's	Tukey	Sig.
WT v HetP v HetN	p=0.24		0.42	p>=0.05	ns
(WT+HetP) v HetN	p=0.09	p=0.48			ns
WT v (HetP+HetN)	P=0.31	p=0.22			ns

8.2.7 Intrinsic Properties – Action Potential Half-Height Duration

Fig. 8-8 shows plots of the mean action potential half-height duration values for each cell type and grouped data. The data did not pass the D'Agostino and Pearson normality test. There were no candidate outliers and the failure to fit a Gaussian distribution was probably because of the closeness of values. In this case, it was decided to perform non-parametric tests (Kruskal-Wallis one-way ANOVA with Dunn's Multiple Comparison Test and the Mann-Whitney U t-test). Mean values ±SEM were WT 1.04 ± 0.06ms, HetP 1.05 ± 0.02ms, HetN 1.15 ± 0.06ms. There were no significant differences between cell types (one-way ANOVA, p=0.27 with Dunn's multiple comparisons (p>0.05) or grouped data Mann-Whitney U t-tests, p>0.05). Table 8-8 summarises the analysis.

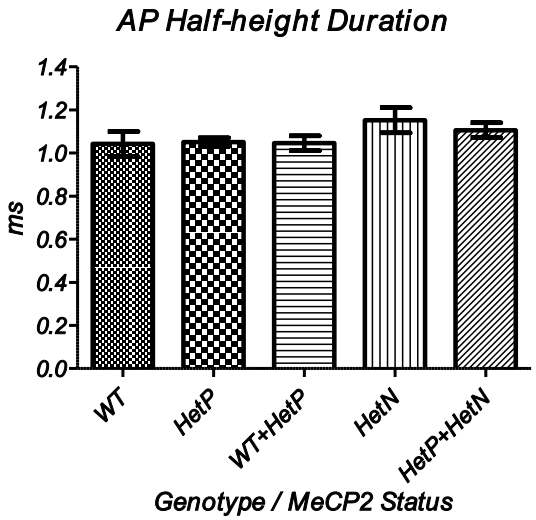

Figure 8-8 Plot of mean action potential half-height duration ±SEM for each cell type and comparisons include WT+HetP and HetP+HetN. There were no significant differences between groups (p>0.05 for all comparisons) (WT n=14, HetP n=10, HetN n=12)

Table 8-8 Action potential half-height duration statistics (WT n=14, HetP n=10, HetN n=12)

Comparison	KW/t-test	Medians	Dunn's	Sig.
WT v HetP v HetN	p=0.27		p>0.05	ns
(WT+HetP) v HetN	p=0.11	p>=0.05		ns
WT v (HetP+HetN)	P=0.28	p>=0.05		ns

8.2.8 Intrinsic Properties – Action Potential Maximum Slope Rise

Fig. 8-9 shows plots of the mean action potential maximum slope rise values for each cell type and grouped data. An unusually high value (875.04mV/ms) and an unusually low value (241.33mV/ms) were observed in the WT data and excluded as outliers. Mean values were WT 586.5 ± 24.5mV/ms, HetP 583.6 ± 25.5mV/ms, HetN 546.1 ± 39.4mV/ms. Although the data set passed the D'Agostino and Pearson normality test there were some differences in variance. It was decided to perform a Kruskal-Wallis non-parametric ANOVA with Dunn's multiple comparisons and Mann-Whitney U t-test. There were no significant differences between cell types (Kruskal-Wallis ANOVA, p=0.59) or grouped data (Mann-Whitney U, p>0.05). Table 8-9 summarises the analysis.

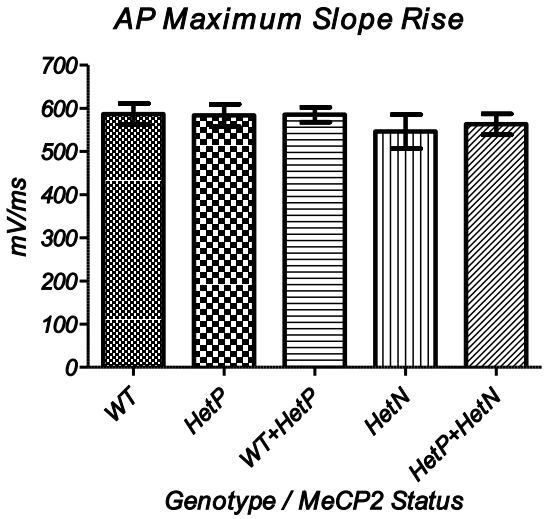

Figure 8-9 Plot of mean action potential maximum slope rise ±SEM for each cell type and comparisons include WT+HetP and HetP+HetN. Outliers were excluded from the WT data. There were no significant differences between groups (p>0.05 for all comparisons) (WT n=12, HetP n=10, HetN n=12)

Table 8-9 Action potential max slope rise statistics (WT n=12, HetP n=10, HetN n=12)

Comparison	ANOVA/t-test	Dunn's	Medians	Sig.
WT v HetP v HetN	p=0.59	p>=0.05		ns
(WT+HetP) v HetN	p=0.50		p>=0.05	ns
WT v (HetP+HetN)	P=0.60		p>=0.05	ns

8.2.9 Intrinsic Properties – Action Potential Maximum Slope Decay

Fig. 8-10 shows plots of the mean action potential maximum slope decay values for each cell type and grouped data. The WT data had one unusually high slope decay value of 158.45 together with an unusually low value of 52.16.The HetN data had an unusually low value of 59.73. All those values were deemed outliers and excluded from analysis. The adjusted data passed the D'Agostino and Pearson normality test and there were no significant differences in variance. Mean values ±SEM were WT 106.0 ± 4.9mV/ms, HetP 101.1 ± 3.3mV/ms, HetN 97.3 ± 4.3mV/ms. There were no significant differences between cell types (one-way ANOVA, p=0.35 with Tukey's post hoc comparisons (p>0.05) or grouped data unpaired t-tests, p>0.05). Table 8-10 summarises the analysis.

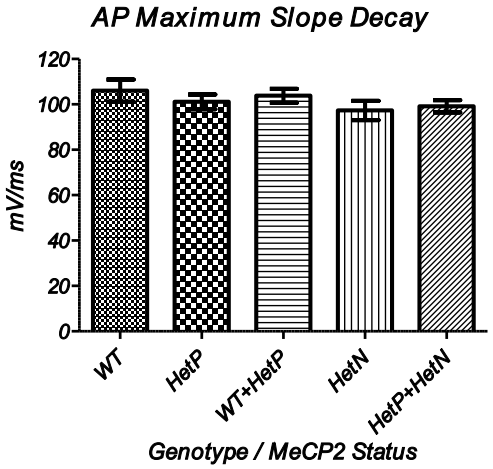

Figure 8-10 Plot of mean action potential maximum slope decay ±SEM for each cell type and comparisons include WT+HetP and HetP+HetN. Outliers were excluded from the WT and HetN data. There were no significant differences between groups (p>0.05 for all comparisons) (WT n=12, HetP n=10, HetN n=11)

Table 8-10 Action potential max slope decay statistics (WT n=12, HetP n=10, HetN n=11)

Comparison	ANOVA/t-test	F-test	Bartlett's	Tukey	Sig.
WT v HetP v HetN	p=0.35		0.33	p>=0.05	ns
(WT+HetP) v HetN	p=0.23	p=1.00			ns
WT v (HetP+HetN)	P=0.19	p=0.20			ns

8.2.10 Intrinsic Properties – Medium After-hyperpolarisation Amplitudes

Fig. 8-11 shows plots of the mean after-hyperpolarisation amplitude values for each cell type and grouped data. The WT data had one unusually low amplitude (-22.56mV) and was excluded from the analysis. The data passed the D'Agostino and Pearson normality test and there were no significant differences in variance. Mean values ±SEM were WT -10.2 ± 0.8mV, HetP -9.4 ± 0.7mV, HetN -10.2 ± 0.8mV. There were no significant differences between cell types (one-way ANOVA, p=0.77 with Tukey's post hoc comparisons (p>0.05) or grouped data unpaired t-tests, p>0.05). Table 8-11 summarises the analysis.

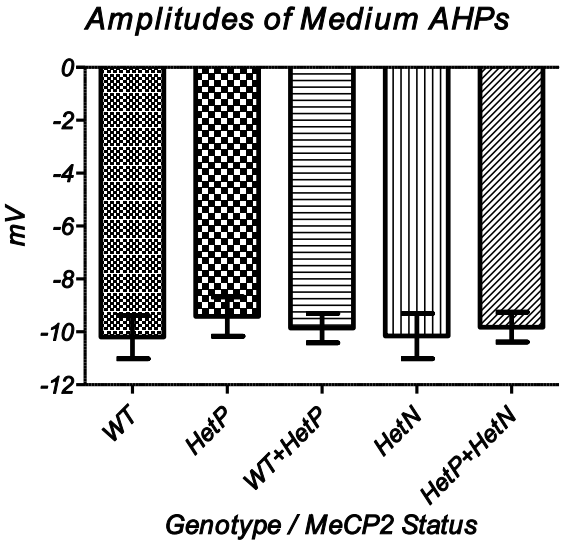

Figure 8-11 Plot of mean after-hyperpolarisation amplitudes ±SEM for each cell type and comparisons include WT+HetP and HetP+HetN. An outlier was excluded from the WT data. There were no significant differences between groups (p>0.05 for all comparisons) (WT n=13, HetP n=10, HetN n=12)

Table 8-11 Medium AHP amplitude statistics (WT n=13, HetP n=10, HetN n=12)

Comparison	ANOVA/ t-test	F-test	Bartlett's	Tukey	Sig.
WT v HetP v HetN	p=0.77		0.75	p>=0.05	ns
(WT+HetP) v HetN	p=0.76	p=0.65			ns
WT v (HetP+HetN)	P=0.70	p=0.67			ns

8.2.11 Intrinsic Properties – Peak Current-Voltage Relationship

Fig. 8-12 shows plots of the mean peak I-V values for each cell type and grouped data. The data set passed the D'Agostino and Pearson normality test. Mean values were WT 0.117 ± 0.007mV/pA, HetP 0.129 ± 0.010mV/pA, HetN 0.145 ± 0.013mV/pA. There was some difference in variance between groups and the variance was reduced by applying a logarithmic transform. There were no significant differences between cell types (one-way ANOVA, p=0.17 with Tukey's post hoc comparisons (p>0.05) or grouped data unpaired t-tests, p>0.05). Table 8-12 summarises the analysis.

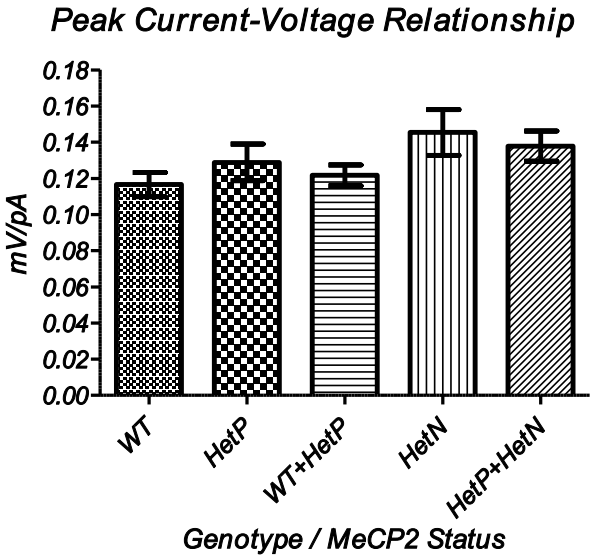

Figure 8-12 Plot of mean peak current-voltage relationship ±SEM for each cell type and comparisons include WT+HetP and HetP+HetN. There were no significant differences between groups (p>0.05 for all comparisons) (WT n=14, HetP n=10, HetN n=12)

Table 8-12 Peak Current-Voltage relationship statistics (WT n=14, HetP n=10, HetN n=12)

Comparison	ANOVA/t-test	F-test	Bartlett's	Tukey	Sig.
WT v HetP v HetN	p=0.17		0.42	p>=0.05	ns
(WT+HetP) v HetN	p=0.10	p=0.17			ns
WT v (HetP+HetN)	P=0.10	p=0.37			ns

8.2.12 Intrinsic Properties – Steady State Current-Voltage Relationship

Fig. 8-13 shows plots of the mean steady-state I-V values for each cell type and grouped data. The data contained several rather high values (0.1824mV/pA in the HetP data and 0.1926mV/pA in the HetN data) which were deemed outliers and excluded. The data passed the D'Agostino and Pearson normality test. The mean values ±SEM were WT 0.099 ± 0.006mV/pA, HetP 0.098 ± 0.006mV/pA, HetN 0.114 ± 0.007mV/pA. There were no significant differences between cell types (one-way ANOVA, p=0.17 with Tukey's post hoc comparisons (p>0.05) or grouped data unpaired t-tests, p>0.05). Table 8-13 summarises the analysis.

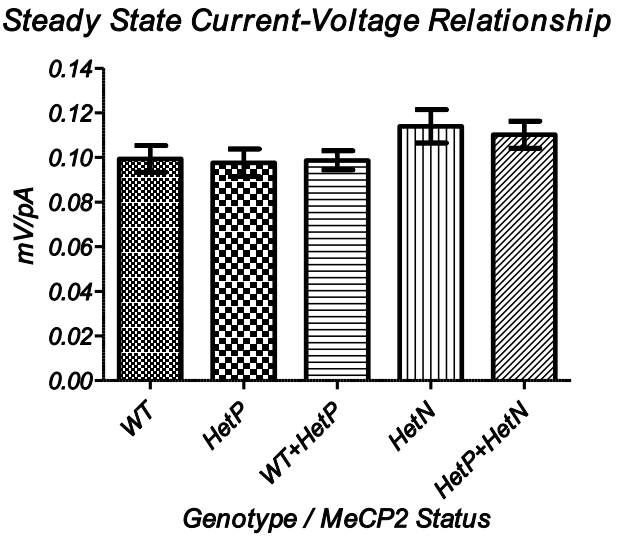

Figure 8-13 Plot of mean steady-state current-voltage relationship ±SEM for each cell type and comparisons include WT+HetP and HetP+HetN. Outliers were excluded from the HetP and HetN data. There were no significant differences between groups (p>0.05 for all comparisons) (WT n=14, HetP n=9, HetN n=11)

Table 8-13 Steady-state current-voltage relationship statistics (WT n=14, HetP n=9, HetN n=11)

Comparison	ANOVA/t-test	F-test	Bartlett's	Tukey	Sig.
WT v HetP v HetN	p=0.19		0.71	p>=0.05	ns
(WT+HetP) v HetN	p=0.07	p=0.44			ns
WT v (HetP+HetN)	P=0.23	p=0.40			ns

8.2.13 Intrinsic Properties – Maximum Action Potential Spike Discharge Frequency

Fig. 8-14 shows plots of the mean AP spike frequency values for each cell type and grouped data. The data set passed the normality test and variances were not significantly different. Mean values ±SEM were WT 33.1 ± 3.1Hz, HetP 35.8 ± 2.9Hz, HetN 35.3 ± 3.3Hz. There were no significant differences between cell types (one-way ANOVA, p=0.82 with Tukey's post hoc comparisons (p>0.05) or grouped data unpaired t-tests, p>0.05). Table 8-14 summarises the analysis.

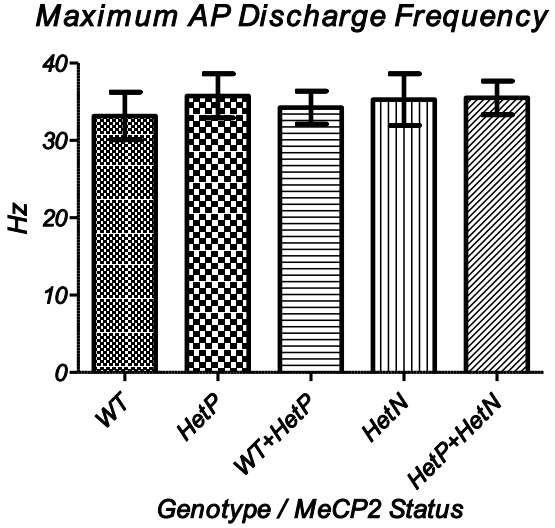

Figure 8-14 Plot of mean maximum AP discharge frequency ±SEM for each cell type and comparisons include WT+HetP and HetP+HetN. There were no significant differences between groups (p>0.05 for all comparisons) (WT n=14, HetP n=10, HetN n=12)

Table 8-14 Maximum AP discharge frequency statistics (WT n=14, HetP n=10, HetN n=12)

Comparison	ANOVA/t-test	F-test	Bartlett's	Tukey	Sig.
WT v HetP v HetN	p=0.82		0.71	p>=0.05	ns
(WT+HetP) v HetN	p=0.79	p=0.66			ns
WT v (HetP+HetN)	p=0.53	p=0.60			ns

8.2.14 Intrinsic Properties – Frequency-Current Relationships

Fig. 8-15 shows plots of mean spike frequency ±SEM against current step over the range 0pA to +250pA with a 50pA step. Data was analysed in 'R' using a one-way MANOVA to compare vectors. The data was transformed using the Yeo-Johnson power transform and passed the Anderson-Darling test for multivariate normality. The mean ± SEM best fit slope values were WT 0.136 ± 0.006Hz/pA, HetP 0.138 ± 0.003Hz/pA, HetN 0.145 ± 0.008Hz/pA. There were no significant differences across cell types or grouped data (MANOVA, $p>0.05$). Table 8-15 summarises the mean frequency ± SEM for each current step in the range 50-250pA together with the slope values ± SEM. Table 8-16 summarises the analysis.

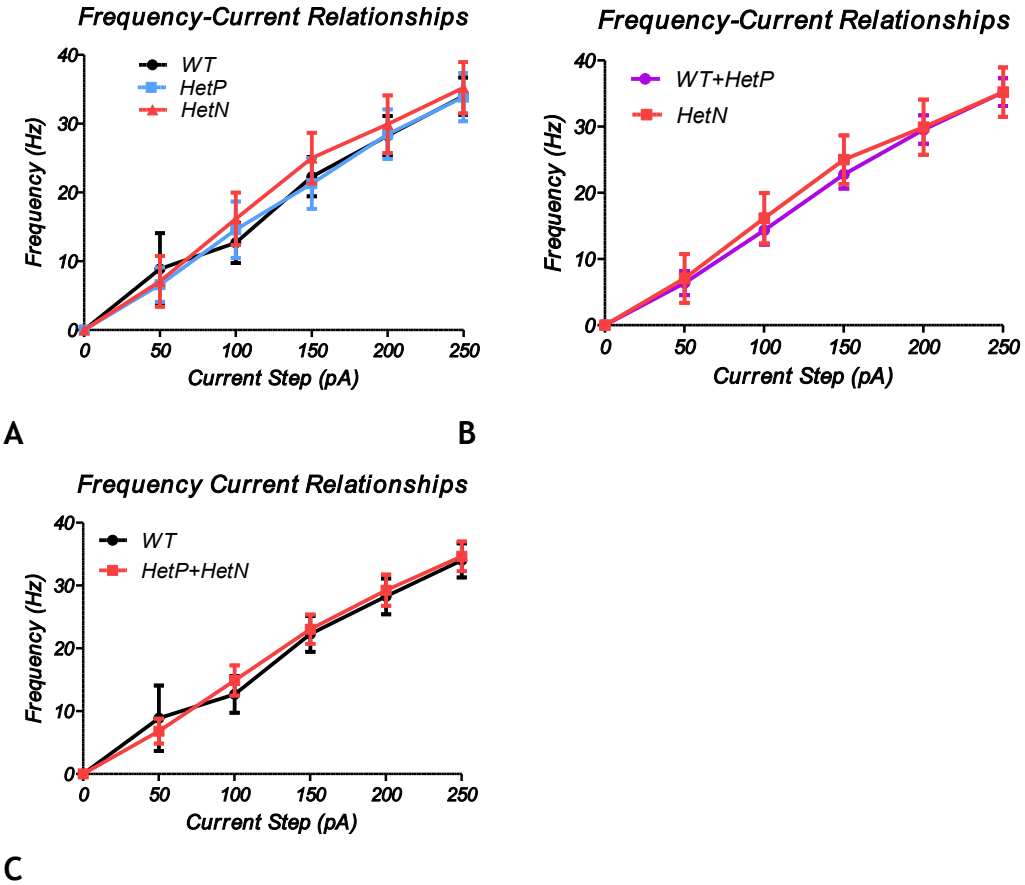

Figure 8-15 Plot of mean frequency-current relationships ±SEM for (A) each cell type and comparisons between (B) HetN and (WT+HetP) and (C) WT and (HetP+HetN). There were no significant differences between groups (MANOVA $p>0.05$ for all comparisons) (WT n=14, HetP n=10, HetN n=12)

Table 8-15 Mean frequencies per current step ± SEM plus slopes (WT n=14, HetP n=10, HetN n=12)

Step (+pA)	WT (Hz)	HetP (Hz)	HetN (Hz)
50	8.9 ± 5.2	6.6 ± 2.5	7.1 ± 3.7
100	12.7 ± 2.9	14.6 ± 4.1	16.2 ± 3.8
150	22.3 ± 2.9	21.3 ± 3.7	25.0 ± 3.7
200	28.3 ± 2.9	28.5 ± 3.6	29.9 ± 4.2
250	34.0 ± 2.7	33.9 ± 3.5	35.2 ± 3.7
Slope	0.136 ± 0.006	0.138 ± 0.003	0.145 ± 0.008

Table 8-16 Mean frequency-current statistics (WT n=14, HetP n=10, HetN n=12)

Comparison	MANOVA	A-D test	Sig.
WT v HetP v HetN	p=0.70	p=0.57	ns
(WT+HetP) v HetN	p=0.93	p=0.54	ns
WT v (HetP+HetN)	P=0.33	p=0.59	ns

8.3 Evoked Synaptic Responses – Short Term Plasticity

Synaptic deficits have previously been reported in very mildly symptomatic *Mecp2*$^{stop/y}$ mice using extracellular recording (Weng *et al*. 2011). Hence it may be possible to detect deficits in individual MeCP2-ve cells from heterozygous *Mecp2*$^{stop/+}$ females.

After recording the intrinsic responses, the short-term plasticity (STP) of the candidate cells was investigated in order to ascertain whether any differences in STP could be detected between the three cell types. Any such differences could indicate changes in the presynaptic handling of Ca^{2+} ions or changes in postsynaptic sensitivity (Zucker & Regehr, 2002) which might arise as a consequence of a deficit in MeCP2, even in presymptomatic mice. Any differences could then be used as a marker of disease pathophysiology in

heterozygous female RTT mice and the role of MeCP2 in synaptic signalling investigated further.

Some representative examples of voltage-clamp responses in individual cells can be found in Appendix 2.

8.3.1 Short-Term Plasticity – Paired Pulse Facilitation

Table 8-17 summarises the mean paired pulse facilitation ratios ±SEM for each inter-stimulus interval. Fig. 8-17 shows plots of mean paired-pulse facilitation ratios ±SEM against inter-stimulus time interval over the range 25ms to 500ms. Data was analysed in 'R' using a one-way MANOVA (Pilliai's trace statistic) to compare vectors. The data was transformed using the Yeo-Johnson power transform and passed the Anderson-Darling test for multivariate normality. There were no significant differences across cell types or grouped data (MANOVA, $p>0.05$). Table 8-18 summarises the analysis.

Table 8-17 Summary of mean ±SEM PPF ratios for each interval. (WT n=13, HetP n=10, HetN n=12)

PP Interval	WT	HetP	HetN
25ms	1.67±0.09	1.73±0.08	1.87±0.13
50ms	1.66±0.11	1.70±0.10	1.74±0.13
100ms	1.45±0.08	1.46±0.08	1.63±0.10
200ms	1.25±0.07	1.30±0.07	1.30±0.08
500ms	1.03±0.06	1.17±0.06	1.20±0.09

Table 8-18 Paired-pulse facilitation ratio statistics (WT n=13, HetP n=10, HetN n=12)

Comparison	MANOVA	Pillai	Sig.
WT v HetP v HetN	p=0.58	P=0.26	ns
(WT+HetP) v HetN	p=0.43	p=0.15	ns
WT v (HetP+HetN)	P=0.55	p=0.12	ns

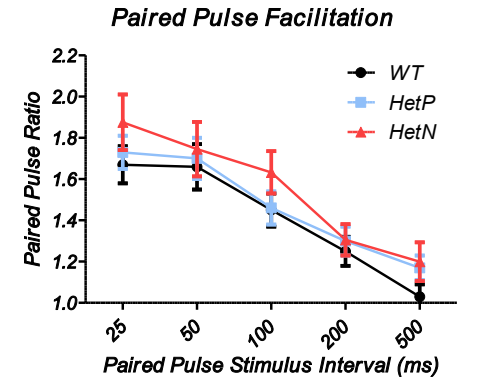

A

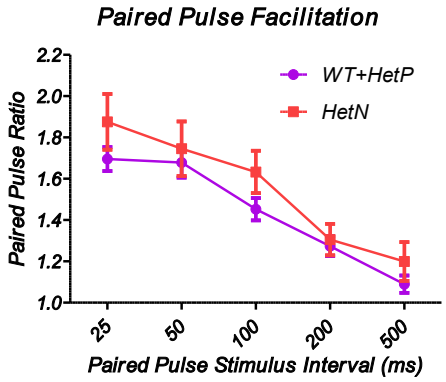

B

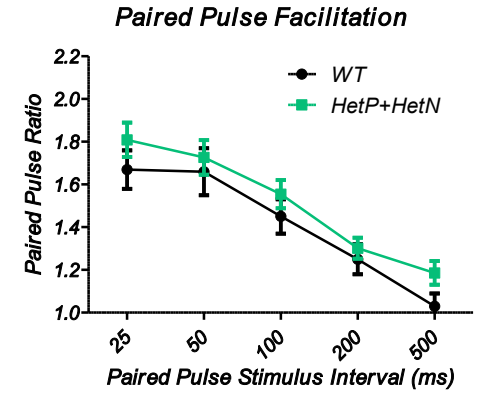

C

Figure 8-16 Plots of mean paired-pulse facilitation ratios ±SEM against inter-stimulus time interval for (A) each cell type and comparisons between (B) HetN and (WT+HetP) and (C) WT and (HetP+HetN) grouped data. There were no significant differences between groups (one-way MANOVA $p>0.05$ for all comparisons) (WT n=13, HetP n=10, HetN n=12)

8.3.2 Short-Term Plasticity - Frequency Facilitation

Tables 8-19 thru 8-22 summarise the mean normalised frequency facilitation responses ±SEM for each stimulus in a train numbered 1-10 and with a separate table for each frequency (5Hz, 10Hz, 20Hz and 40Hz).

Table 8-19 Mean values of 5Hz frequency facilitation responses normalized to first response. Values show ± SEM. WT n=13, HetN n=10, HetP n=9.

Stim. No.	WT	HetP	HetN
1	1.00	1.00	1.00
2	1.24±0.08	1.33±0.06	1.28±0.11
3	1.24±0.08	1.38±0.07	1.29±0.12
4	1.37±0.15	1.40±0.09	1.35±0.13
5	1.42±0.17	1.40±0.10	1.38±0.16
6	1.45±0.20	1.46±0.11	1.36±0.14
7	1.42±0.11	1.52±0.11	1.45±0.15
8	1.49±0.17	1.57±0.12	1.45±0.15
9	1.57±0.21	1.57±0.10	1.47±0.17
10	1.60±0.17	1.64±0.11	1.45±0.15

Table 8-20 Mean values of 10Hz frequency facilitation responses normalized to first response. Values show ± SEM. WT n=13, HetN n=10, HetP n=9.

Stim. No.	WT	HetP	HetN
1	1.00	1.00	1.00
2	1.27±0.09	1.41±0.08	1.37±0.07
3	1.32±0.10	1.60±0.08	1.47±0.11
4	1.40±0.14	1.56±0.08	1.47±0.12
5	1.45±0.19	1.58±0.08	1.46±0.12
6	1.42±0.14	1.64±0.09	1.56±0.17
7	1.50±0.18	1.64±0.10	1.52±0.14
8	1.47±0.17	1.68±0.10	1.61±0.15
9	1.58±0.21	1.66±0.10	1.58±0.15
10	1.50±0.18	1.66±0.11	1.55±0.13

Table 8-21 Mean values of 20Hz frequency facilitation responses normalized to first response. Values show ± SEM. WT n=13, HetN n=10, HetP n=9.

Stim. No.	WT	HetP	HetN
1	1.00	1.00	1.00
2	1.34±0.09	1.60±0.10	1.50±0.12
3	1.52±0.13	1.80±0.12	1.71±0.17
4	1.62±0.17	1.87±0.17	1.75±0.21
5	1.61±0.17	1.87±0.16	1.73±0.19
6	1.61±0.16	1.84±0.16	1.81±0.22
7	1.67±0.19	1.88±0.16	1.84±0.22
8	1.55±0.18	1.89±0.16	1.87±0.26
9	1.64±0.20	1.91±0.17	1.93±0.26
10	1.69±0.21	1.93±0.16	1.95±0.25

Table 8-22 Mean values of 40Hz frequency facilitation responses normalized to first response. Values show ± SEM. WT n=13, HetN n=10, HetP n=9.

Stim. No.	WT	HetP	HetN
1	1.00	1.00	1.00
2	1.62±0.11	1.65±0.07	1.54±0.09
3	1.81±0.15	1.96±0.14	1.89±0.21
4	1.97±0.21	1.98±0.17	1.95±0.27
5	2.04±0.27	2.01±0.19	2.03±0.35
6	2.03±0.25	2.01±0.20	2.19±0.37
7	2.07±0.29	2.01±0.21	2.17±0.39
8	2.22±0.32	2.03±0.22	2.30±0.46
9	2.09±0.29	2.11±0.22	2.30±0.45
10	2.03±0.26	2.16±0.24	2.29±0.42

Fig. 8-17 (A) shows plots of mean normalised 5Hz frequency facilitation responses ±SEM against stimulus number, 1-10. Fig. 8-17 (B) shows comparisons between (WT+HetP) vs. HetN and Fig. 8-x17 (C) between WT vs. (HetP+HetN). Data was analysed in 'R' using a one-way MANOVA (Pilliai's trace statistic) to compare vectors. The data was transformed using the Yeo-Johnson power transform and passed the Anderson-Darling test for multivariate normality. There were no significant differences across cell types or grouped data (MANOVA, $p>0.05$). Table 8-23 summarises the analysis.

Table 8-23 5Hz Frequency facilitation statistics (WT n=13, HetP n=10, HetN n=12)

Comparison 5Hz	MANOVA	Pillai	Sig.
WT v HetP v HetN	p=0.54	P=0.55	ns
(WT+HetP) v HetN	p=0.37	p=0.32	ns
WT v (HetP+HetN)	P=0.39	p=0.33	ns

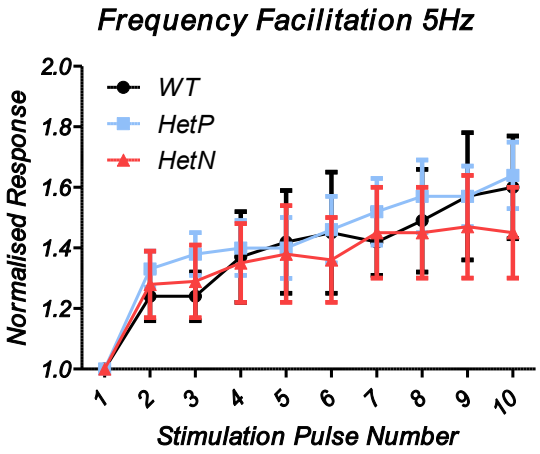

A

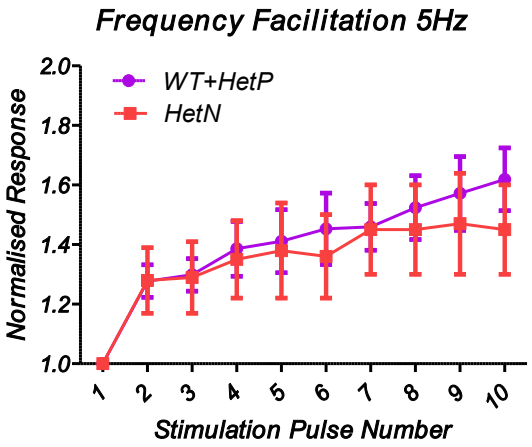

B

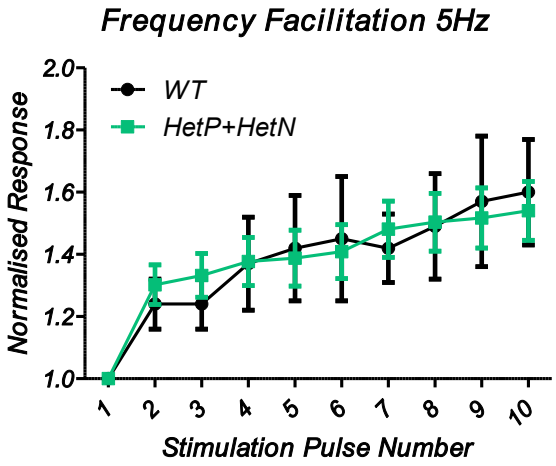

C

Figure 8-17 Plots of 5Hz mean normalised frequency facilitation responses ±SEM against stimulus number for (A) each cell type and comparisons between (B) HetN and (WT+HetP) and (C) WT and (HetP+HetN) grouped data. There were no significant differences between groups (one-way MANOVA $p>0.05$ for all comparisons) (WT n=13, HetP n=10, HetN n=12)

Fig. 8-18 (A) shows plots of mean normalised 10Hz frequency facilitation responses ±SEM against stimulus number, 1-10. Fig. 8-18 (B) shows comparisons between (WT+HetP) vs. HetN and Fig. 8-18 (C) between WT vs. (HetP+HetN). Data was analysed in 'R' using a one-way MANOVA (Pilliai's trace statistic) to

compare vectors. The data was transformed using the Yeo-Johnson power transform and passed the Anderson-Darling test for multivariate normality. There were no significant differences across cell types (MANOVA p=0.08 but the WT vs. (HetP+HetN) grouped data did indicate a significant difference (MANOVA, p=0.03). Table 8-24 summarises the analysis.

Table 8-24 10Hz Frequency facilitation statistics (WT n=13, HetP n=10, HetN n=12)

Comparison 10Hz	MANOVA	Pillai	Sig.
WT v HetP v HetN	p=0.08	P=0.81	ns
(WT+HetP) v HetN	p=0.54	p=0.27	ns
WT v (HetP+HetN)	P=0.03	p=0.52	*

The 10Hz WT/HetP/HetN comparison exhibits a low p-value (p=0.08). Inspection of the raw data reveals that the value of the mean WT vector was reduced as a consequence of the presence of two cells where the first pulse in the train was unusually large. This meant that the normalization to this first pulse produced a vector consisting of ratio values less than one. This had the effect off decreasing the overall mean WT vector. Since the affected pulse trains showed facilitation the data was not excluded. However, it is not thought that any biological significance can be attributed to the apparent statistical difference.

Fig. 8-19 (A) shows plots of mean normalised 20Hz frequency facilitation responses ±SEM against stimulus number, 1-10. Fig. 8-19 (B) shows comparisons between (WT+HetP) vs. HetN and Fig. 8-19 (C) between WT vs. (HetP+HetN). Data was analysed in 'R' using a one-way MANOVA (Pilliai's trace statistic) to compare vectors. The data was transformed using the Yeo-Johnson power transform and passed the Anderson-Darling test for multivariate normality.

There were no significant differences across cell types (MANOVA p=0.41 or between grouped data (MANOVA, p>0.05). The low p-value given by the WT v (HetP+HetN) comparison is accounted for in the same way as discussed in the 10Hz results. Table 8-25 summarises the analysis.

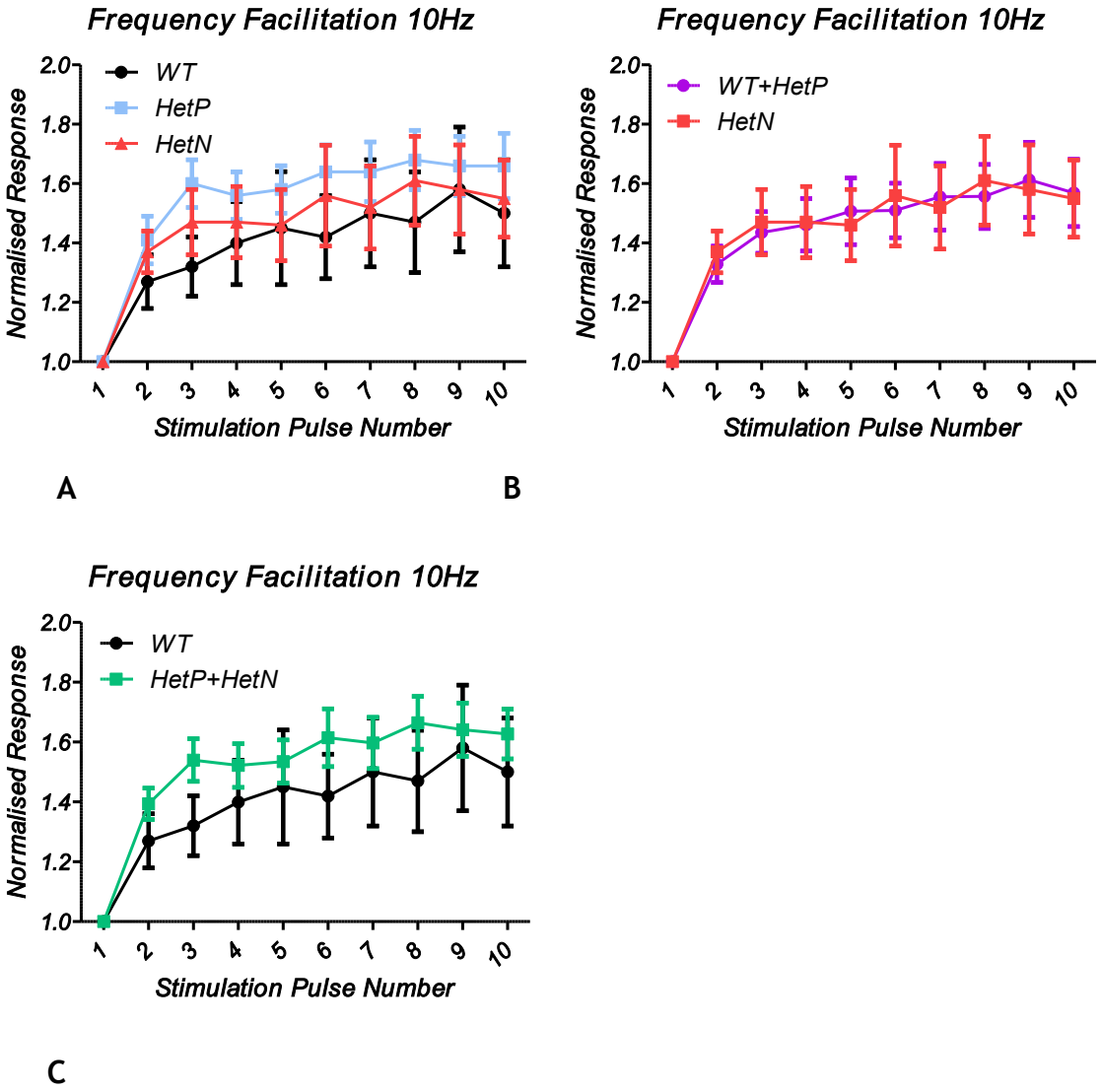

Figure 8-18 Plots of 10Hz mean normalised frequency facilitation responses ±SEM against stimulus number for (A) each cell type and comparisons between (B) HetN and (WT+HetP) and (C) WT and (HetP+HetN) grouped data. There were no significant differences in (A) or (B) (one-way MANOVA $p>0.05$ for all comparisons) but there was a significant difference between the grouped data in (C) (one-way MANOVA, $p=0.03$) (WT n=13, HetP n=10, HetN n=12)

Table 8-25 20Hz Frequency facilitation statistics (WT n=13, HetP n=10, HetN n=12)

Comparison 20Hz	MANOVA	Pillai	Sig.
WT v HetP v HetN	p=0.41	P=0.61	ns
(WT+HetP) v HetN	p=0.82	p=0.18	ns
WT v (HetP+HetN)	P=0.09	p=0.44	ns

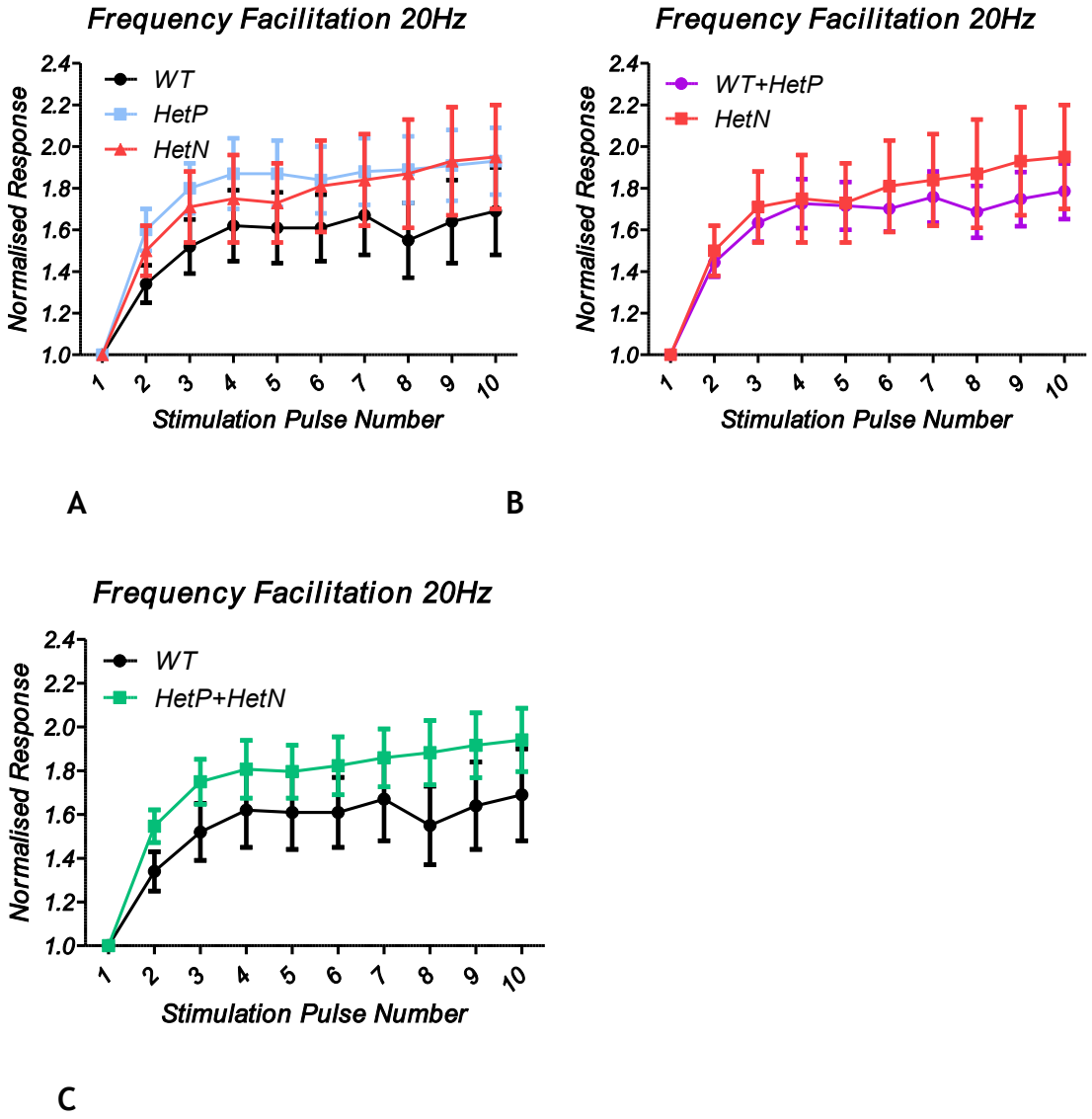

Figure 8-19 Plots of 20Hz mean normalised frequency facilitation responses ±SEM against stimulus number for (A) each cell type and comparisons between (B) HetN and (WT+HetP) and (C) WT and (HetP+HetN) grouped data. There were no significant differences (one-way MANOVA $p>0.05$ for all comparisons) but there was a low p-value for the grouped data in (C) (one-way MANOVA, $p=0.09$) (WT n=13, HetP n=10, HetN n=12)

Fig. 8-20 (A) shows plots of mean normalised 40Hz frequency facilitation responses ±SEM against stimulus number, 1-10. Fig. 8-20 (B) shows comparisons between (WT+HetP) vs. HetN and Fig. 8-20 (C) between WT vs. (HetP+HetN). Data was analysed in 'R' using a one-way MANOVA (Pilliai's trace statistic) to compare vectors. The data was transformed using the Yeo-Johnson power transform and passed the Anderson-Darling test for multivariate normality. There were no significant differences across cell types (MANOVA, p=0.42 or between grouped data (MANOVA, p>0.05). Table 8-26 summarises the analysis.

Table 8-26 40Hz Frequency facilitation statistics (WT n=13, HetP n=10, HetN n=12)

Comparison 40Hz	MANOVA	Pillai	Sig.
WT v HetP v HetN	p=0.42	P=0.60	ns
(WT+HetP) v HetN	p=0.86	p=0.17	ns
WT v (HetP+HetN)	P=0.38	p=0.32	ns

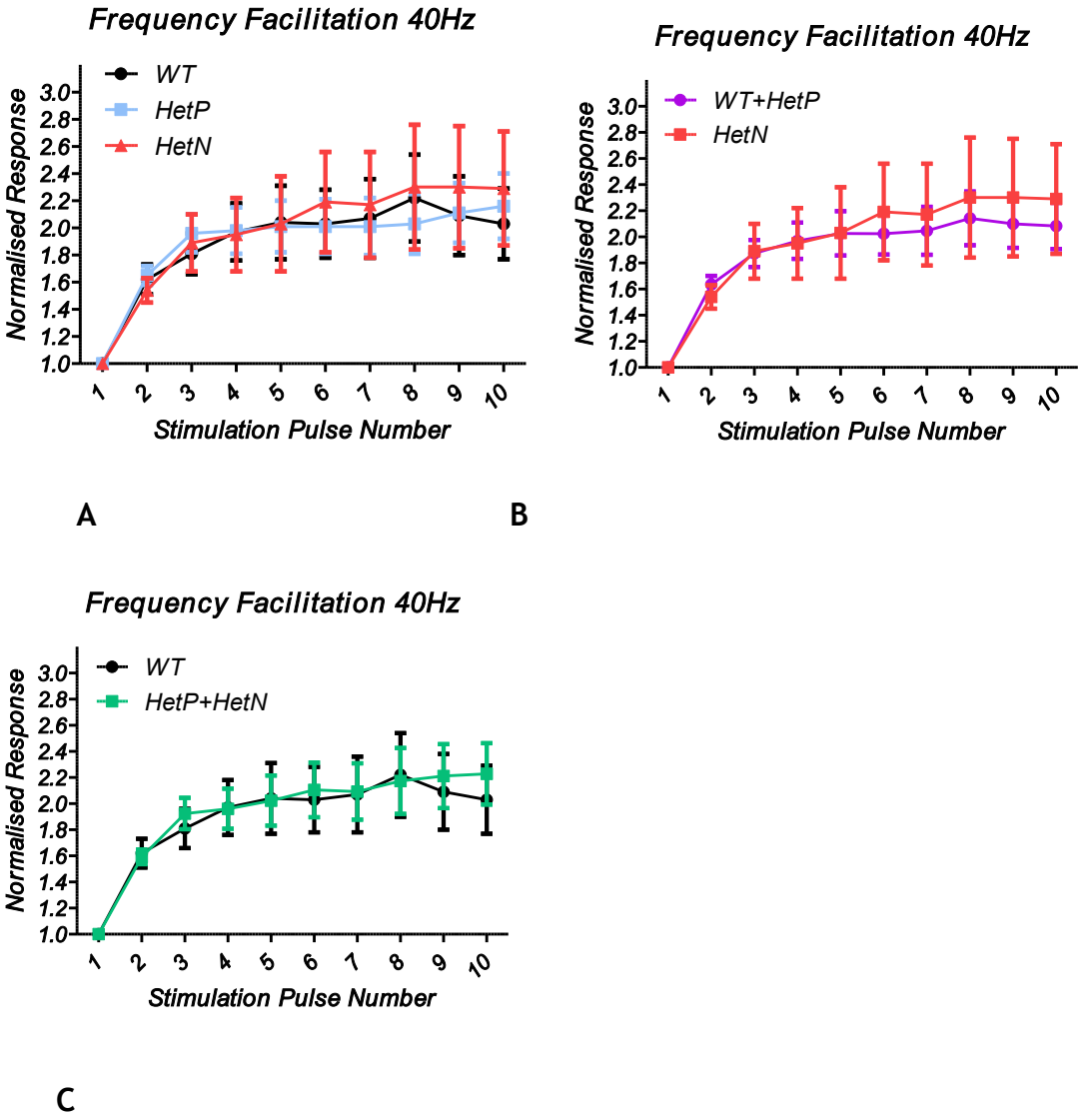

Figure 8-20 Plots of 40Hz mean normalised frequency facilitation responses ±SEM against stimulus number for (A) each cell type and comparisons between (B) HetN and (WT+HetP) and (C) WT and (HetP+HetN) grouped data. There were no significant differences (one-way MANOVA $p>0.05$ for all comparisons) (WT n=13, HetP n=10, HetN n=12)

8.4 Analysis of PPF Waveforms

8.4.1 Evoked Synaptic Waveform Postsynaptic Properties

The measurement and analysis of the evoked synaptic waveforms provides information about the postsynaptic properties of the cell being recorded and for which the MeCP2 status was known.

For each cell type the two peaks from the 25ms interval paired-pulse facilitation waveforms were analyzed in Stimfit to obtain the peak amplitude, 20-80% rise time, half-height duration, and decay time. In some cases there was difficulty with the analysis of some parameters in Stimfit because of noise or artifacts and this is reflected in a reduction in some of the reported n-numbers. The mean values ± SEM of the data is summarized in Table 8-27. Statistical analysis was performed in GraphPad Prism.

Table 8-27 Properties of evoked postsynaptic waveforms from 25ms PPF interval (WT n=11-13, HetP n=8-10, HetN n=7-9)

PSC property:	WT	HetP	HetN
1st PSC amplitude (pA)	-122.2 ± 18.5	-112.30 ± 14.51	-173.18 ± 14.8
2nd PSC amplitude (pA)	-196.15 ± 27.17	-192.71 ± 27.89	-299.06 ± 61.51
1st 20-80% rise time (ms)	1.55 ± 0.12	1.69 ± 0.15	1.49 ± 0.12
2nd 20-80% rise time (ms)	1.43 ± 0.11	1.37 ± 0.12	1.32 ± 0.12
1st Decay time constant	8.93 ± 1.30	9.72 ± 1.31	8.94 ± 1.08
2nd Decay time constant	9.61 ± 1.02	10.50 ± 1.00	7.60 ± 0.58
1st ½ height duration (ms)	8.07 ± 0.78	8.47 ± 0.60	9.03 ± 0.49
2nd ½ height duration (ms)	8.95 ± 0.75	8.71 ± 0.50	8.48 ± 0.50

8.4.2 PPF Waveforms – First Pulse Amplitude

Fig. 8-21 shows plots of the PPF first pulse amplitudes. The data set initially failed the D'Agostino and Pearson normality test. An outlier was identified in the HetN data which had a very large value of -405.90pA and this was excluded from further analysis but the data set still failed the normality test. The data set was transformed using a logarithmic algorithm and then passed the normality test. There were no significant differences between coefficients of variation. The mean values ± SEM were WT -122.2 ± 18.5pA, HetP -112.3 ± 14.5pA, HetN -150.5 ± 28.3pA. There were no significant differences between cell types (one-way ANOVA, p=0.73 with Tukey's post hoc comparisons (p>0.05) or grouped data unpaired t-tests, p>0.05). Table 8-28 summarises the analysis.

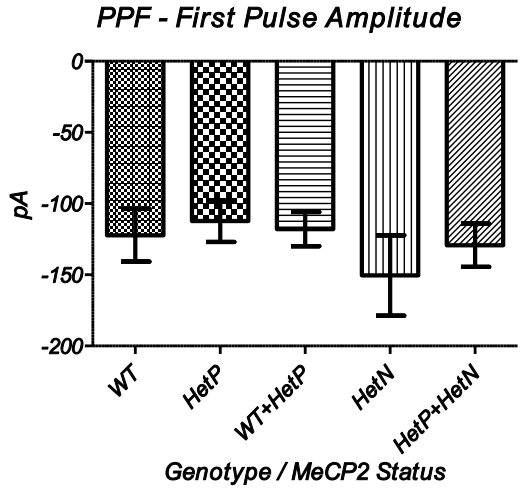

.

Figure 8-21 Plot of mean first pulse amplitudes ±SEM for each cell type and comparisons include WT+HetP and HetP+HetN. There were no significant differences between groups (p>0.05 for all comparisons) (WT n=13, HetP n=10, HetN n=8)

Table 8-28 PPF first pulse amplitude statistics (WT n=13, HetP n=10, HetN n=8)

Comparison	ANOVA /t-test	F-test	Bartlett's	Tukey	Sig.
WT v HetP v HetN	p=0.73		p=0.28	p>=0.05	ns
(WT+HetP) v HetN	p=0.42	p=0.19			ns
WT v (HetP+HetN)	P=0.70	p=0.80			ns

8.4.3 PPF Waveforms – Second Pulse Amplitude

Fig. 8-22 shows plots of the PPF second pulse amplitudes. The data set initially failed the D'Agostino and Pearson normality test. An outlier was identified in the HetN data which had a very large value of -708pA and this was excluded from further analysis. The mean values ±SEM were WT 196.1 ± 27.2pA, HetP -192.7 ± 27.9pA, HetN -247.9 ± 38.8pA. The data set was transformed using a logarithmic algorithm and then passed the normality test. There were no significant differences between coefficients of variation. There were no significant differences between cell types (one-way ANOVA, p=0.49 with Tukey's post hoc comparisons (p>0.05) or grouped data unpaired t-tests, p>0.05). Table 8-29 summarises the analysis.

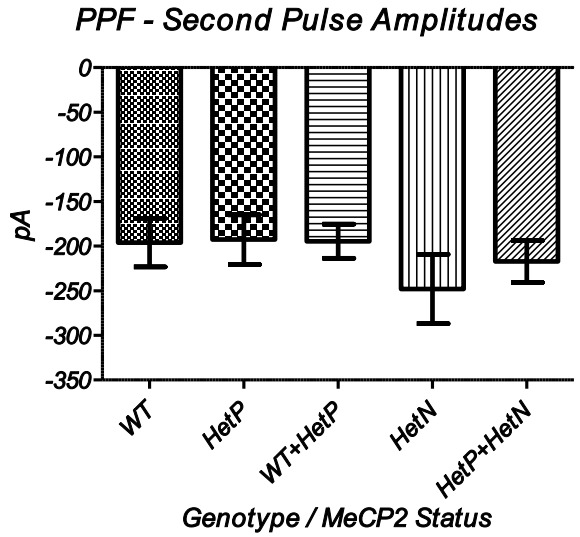

Figure 8-22 Plot of mean second pulse amplitudes ±SEM for each cell type and comparisons include WT+HetP and HetP+HetN. There were no significant differences between groups (p>0.05 for all comparisons) (WT n=13, HetP n=10, HetN n=8)

Table 8-29 PPF second pulse amplitude statistics (WT n=13, HetP n=10, HetN n=8)

Comparison	ANOVA/ t-test	F-test	Bartlett's	Tukey	Sig.
WT v HetP v HetN	p=0.49		p=0.46	p>=0.05	ns
(WT+HetP) v HetN	p=0.23	p=0.77			ns
WT v (HetP+HetN)	P=0.49	p=0.60			ns

8.4.4 PPF Waveforms – First Pulse 20-80% Rise Time

Fig. 8-23 shows plots of the PPF first pulse 20-80% rise times. The data set passed the D'Agostino and Pearson normality test and coefficients of variation were similar. The mean values ± SEM were WT 1.55 ± 0.12ms, HetP 1.69 ± 0.15ms, HetN 1.49 ± 0.12ms. There were no significant differences between cell types (one-way ANOVA, p=0.58 with Tukey's post hoc comparisons (p>0.05) or grouped data unpaired t-tests, p>0.05). Table 8-30 summarises the analysis.

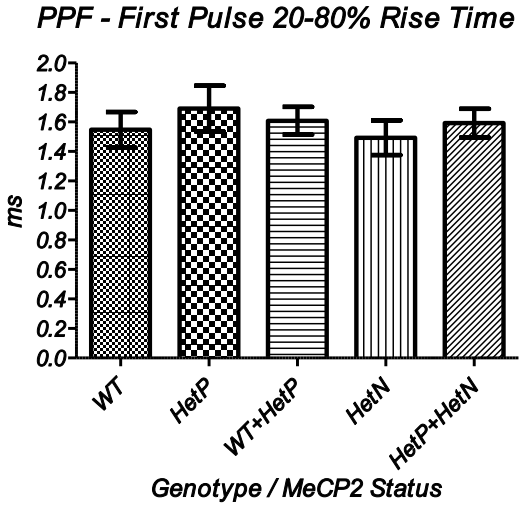

Figure 8-23 Plot of mean first pulse 20-80% rise times ±SEM for each cell type and comparisons include WT+HetP and HetP+HetN. There were no significant differences between groups (p>0.05 for all comparisons) (WT n=11, HetP n=8, HetN n=8)

Table 8-30 PPF first pulse 20-80% rise time statistics (WT n=11, HetP n=8, HetN n=8)

Comparison	ANOVA/ t-test	F-test	Bartlett's	Tukey	Sig.
WT v HetP v HetN	p=0.58		p=0.78	p>=0.05	ns
(WT+HetP) v HetN	p=0.49	p=0.59			ns
WT v (HetP+HetN)	P=0.78	p=0.90			ns

8.4.5 PPF Waveforms – Second Pulse 20-80% Rise Time

Fig. 8-24 shows plots of the PPF second pulse 20-80% rise times. The data set did not initially pass the D'Agostino and Pearson normality test and variances were different between groups. The data was therefore transformed using a logarithmic algorithm. The transformed data then passed the normality test and coefficients of variation were similar. The mean values ±SEM were WT 1.43 ± 0.11ms, HetP 1.37 ± 0.12ms, HetN 1.32 ± 0.12ms.There were no significant differences between cell types (one-way ANOVA, p=0.85 with Tukey's post hoc comparisons (p>0.05) or grouped data unpaired t-tests, p>0.05). Table 8-31 summarises the analysis.

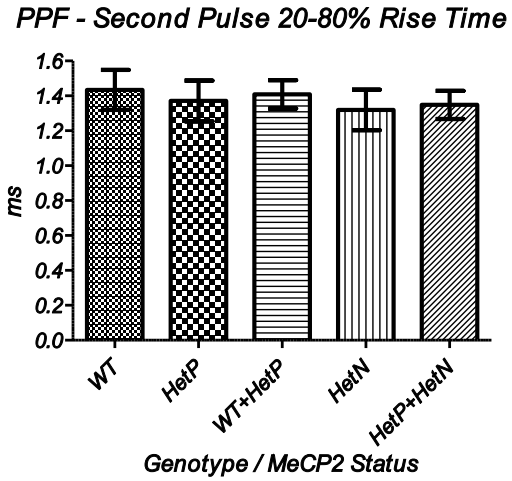

Figure 8-24 Plot of mean second pulse 20-80% rise times ±SEM for each cell type and comparisons include WT+HetP and HetP+HetN. There were no significant differences between groups (p>0.05 for all comparisons) (WT n=13, HetP n=9, HetN n=7)

Table 8-31 PPF second pulse 20-80% rise time statistics (WT n=13, HetP n=9, HetN n=7)

Comparison	ANOVA /t-test	F-test	Bartlett's	Tukey	Sig.
WT v HetP v HetN	p=0.85		p=0.77	p>=0.05	ns
(WT+HetP) v HetN	p=0.63	p=0.73			ns
WT v (HetP+HetN)	P=0.61	p=0.39			ns

8.4.6 PPF Waveforms – First Pulse Half-height Duration

Fig. 8-25 shows plots of the PPF first pulse half-height durations. The data set failed the D'Agostino and Pearson normality test and no obvious outliers could be identified. However, only the HetN data failed the test. As normality could not be achieved via a normalisation step or a transform, it was decided to use a non-parametric ANOVA (Kruskal-Wallis) with a post hoc Dunn's test. A Mann-Whitney U was used for the t-tests. The mean values ±SEM were WT 8.07 ± 0.78ms, HetP 8.5 ± 0.60ms, HetN 9.03 ± 0.49ms.There were no significant differences between cell types (one-way ANOVA, p=0.30 with Dunn's post hoc comparisons (p>0.05) or grouped data Mann-Whitney U t-tests, p>0.05). Table 8-32 summarises the analysis.

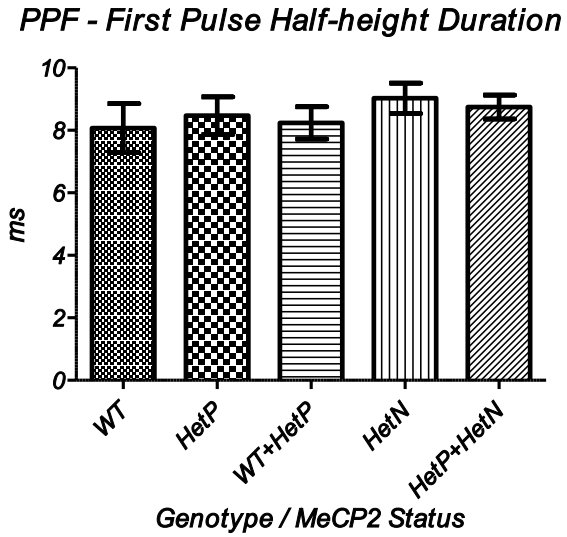

Figure 8-25 Plot of mean first pulse half-height durations ±SEM for each cell type and comparisons include WT+HetP and HetP+HetN. There were no significant differences between groups (p>0.05 for all comparisons) (WT n=13, HetP n=9, HetN n=9)

Table 8-32 PPF first pulse half-height duration statistics (WT n=13, HetP n=9, HetN n=9)

Comparison	ANOVA/t-test	Dunn's	Sig.
WT v HetP v HetN	p=0.30	p>=0.05	ns
(WT+HetP) v HetN	p=0.14		ns
WT v (HetP+HetN)	P=0.24		ns

8.4.7 PPF Waveforms – Second Pulse Half-height Duration

Fig. 8-26 shows plots of the PPF second pulse half-height durations. An usually large value of 15.68ms was identified in the WT data and excluded. The data set then passed the D'Agostino and Pearson normality test and coefficients of variation were similar. The mean values ±SEM were WT 8.39 ± 0.54ms, HetP 8.71 ± 0.50ms, HetN 8.48 ± 0.50ms.There were no significant differences between cell types (one-way ANOVA, p=0.90 with Tukey's post hoc comparisons (p>0.05) or grouped data unpaired t-tests, p>0.05).Table 8-33 summarises the analysis.

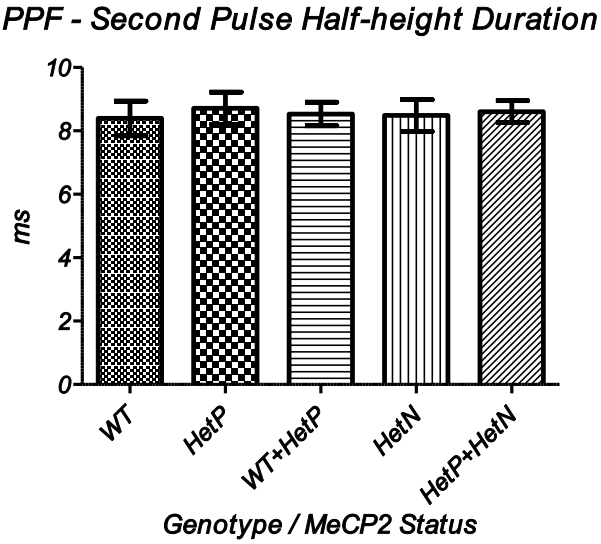

Figure 8-26 Plot of mean second pulse half-height durations ±SEM for each cell type and comparisons include WT+HetP and HetP+HetN. There were no significant differences between groups (p>0.05 for all comparisons) (WT n=13, HetP n=9, HetN n=8)

Table 8-33 PPF second pulse half-height duration statistics (WT n=13, HetP n=9, HetN n=8)

Comparison	ANOVA/t-test	F-test	Bartlett's	Tukey	Sig.
WT v HetP v HetN	p=0.90		p=0.68	p>=0.05	ns
(WT+HetP) v HetN	p=0.95	p=0.65			ns
WT v (HetP+HetN)	P=0.73	p=0.31			ns

8.4.8 PPF Waveforms – First Pulse Decay Time Constants

Fig. 8-27 shows plots of the PPF first pulse decay time constants (tau). Although the data set passed the D'Agostino and Pearson normality test there were significant differences in variance. A logarithmic transform significantly improved the variance without causing a deviation from normality. The mean values ±SEM were WT 8.93 ± 1.30ms, HetP 9.72 ± 1.31ms, HetN 8.94 ±1.08ms. There were no significant differences between cell types (one-way ANOVA, p=0.78 with Tukey's post hoc comparisons (p>0.05) or grouped data unpaired t-tests, p>0.05).Table 8-34 summarises the analysis.

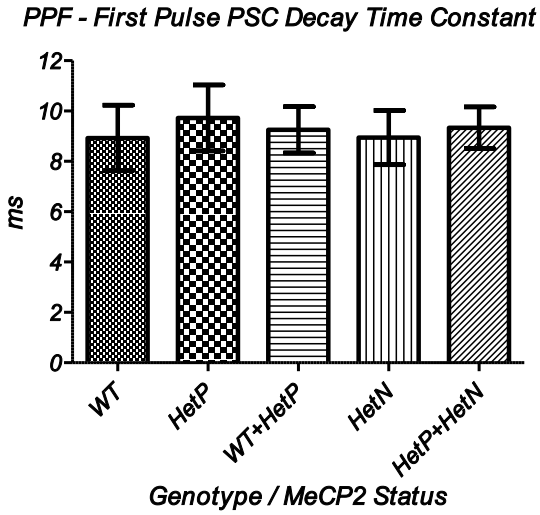

Figure 8-27 Plot of mean first pulse decay time constants ±SEM for each cell type and comparisons include WT+HetP and HetP+HetN. There were no significant differences between groups (p>0.05 for all comparisons) (WT n=12, HetP n=9, HetN n=9)

Table 8-34 PPF first pulse decay time constants statistics (WT n=12, HetP n=9, HetN n=9)

Comparison	ANOVA /t-test	F-test	Bartlett's	Tukey	Sig.
WT v HetP v HetN	p=0.78		p=0.66	p>=0.05	ns
(WT+HetP) v HetN	p=0.99	p=0.59			ns
WT v (HetP+HetN)	P=0.54	p=0.30			ns

8.4.9 PPF Waveforms – Second Pulse Decay Time Constants

Fig. 8-28 shows plots of the PPF second pulse decay time constants (tau). The WT data contained an unusually large value of 19.61ms and this was deemed an outlier and excluded. Although the data set then passed the D'Agostino and Pearson normality test there were significant differences in variance. A logarithmic transform significantly improved the variance without causing a deviation from normality. The mean values ±SEM were WT 8.78 ± 0.63ms, HetP 10.55 ± 1.00ms, HetN 7.60 ± 0.59ms. There were no significant differences between cell types (one-way ANOVA, p=0.07 with Tukey's post hoc comparisons (p>0.05) or grouped data unpaired t-tests, p>0.05). A reduced mean value for the HetN data was noted, and consequently low p-values from the ANOVA and from the (WT+HetP) vs HetN comparison. Table 8-35 summarises the analysis.

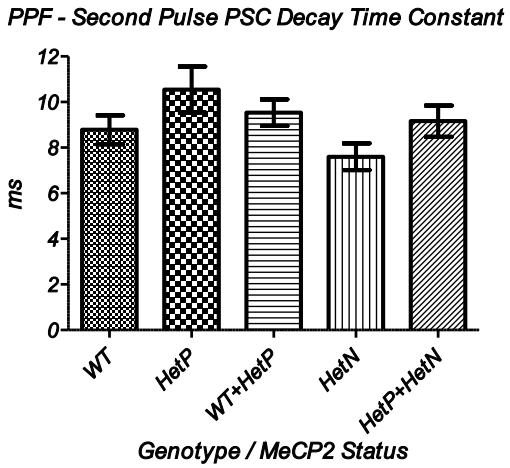

Figure 8-28 Plot of mean first pulse decay time constants ±SEM for each cell type and comparisons include WT+HetP and HetP+HetN. There were no significant differences between groups (p>0.05 for all comparisons) although the mean HetN value was reduced compared to WT and HetP (WT n=12, HetP n=9, HetN n=8).

Table 8-35 PPF second pulse decay time constants statistics (WT n=12, HetP n=9, HetN n=8)

Comparison	ANOVA /t-test	F-test	Bartlett's	Tukey	Sig.
WT v HetP v HetN	p=0.07		P=0.63	p>=0.05	ns
(WT+HetP) v HetN	p=0.08	p=0.38			ns
WT v (HetP+HetN)	P=0.78	p=0.72			ns

8.5 Immunocytochemistry Example

Fig. 8-29 shows representative example confocal images of recorded cells. Low-power images were used to confirm pyramidal morphology and position in the hippocampus. The high-power images, as shown in the figure, were used to ascertain the MeCP2 status of the recorded cells which were filled with Biocytin during recording. The Biocytin was incubated with Avidin-647 conjugate which binds with biotin allowing fluorescence imaging on the confocal microscope using excitation in the far red (637 nm) and pseudocoloured blue in the figure. MeCP2 was detected by incubating with a primary anti-MeCP2 antibody and then with an Alexa-Fluor 488 secondary, pseudocoloured bright green. Alternatively, in the case of mice bred expressing MeCP2-eGFP fusion protein, this could be visualised directly with the blue-green (488 nm) excitation. Figure 8-29 (A) shows an example of an anti-MeCP2 stained slice. MeCP2 is confined to the nucleus but there is also a degree of background fluorescence visible in the left-hand panel. Nevertheless, the merge image clearly shows the presence of MeCP2 in the recorded cell. Figure 8-29 (B) shows an example of cells expressing the MeCP2-eGFP fusion protein. In this case there is little background fluorescence. The eGFP fluorescence is absent from the merged image of the recorded cell indicating its MeCP2-ve status.

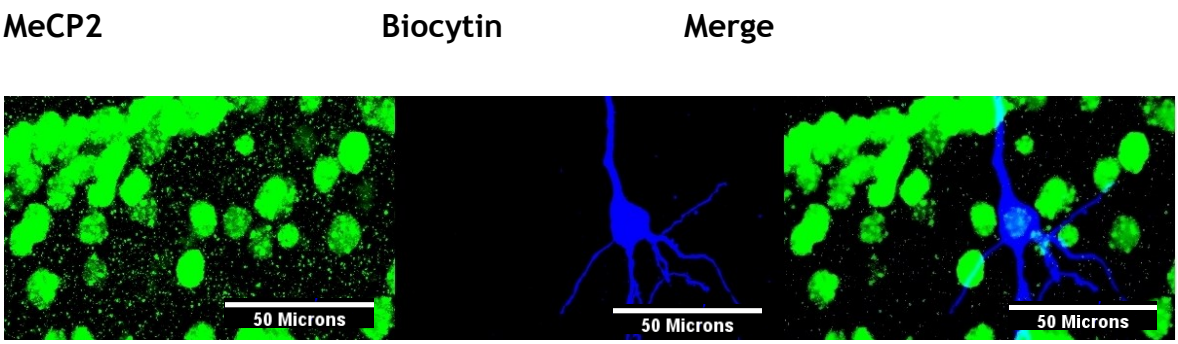

A

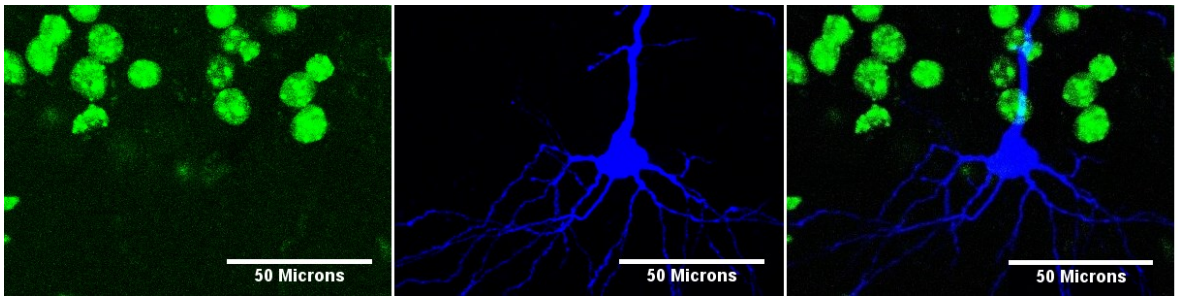

B

Figure 8-29 Confocal micrographs showing MeCP2 immunostaining of CA1 cells.

A – Micrograph showing MeCP2-immunopositive (green) nuclei in area CA1 of *Mecp2*$^{+/-}$ mouse hippocampus. Middle panel shows Biocytin-labelled (pseudocoloured blue) recorded CA1 pyramidal cell. Right panel is merged image revealing the nucleus of the recorded cell to be MeCP2-immunopositive and thus expressing the normal allele.

B – Micrograph showing Mecp2-eGFP nuclei in area CA1 of *Mecp2*$^{+/-}$ mouse hippocampus. . Middle panel shows Biocytin-labelled (pseudocoloured blue) recorded CA1 pyramidal cell. Right panel is merged image revealing the nucleus of the recorded cell to be negative for MeCP2-eGFP and thus expressing the mutant allele. (Scale bars = 50μm)

9 Discussion

9.1 No Significant Differences in either Intrinsic or Evoked Synaptic Properties between Cell Types

The main findings of this study are that there were no overt differences across a range of intrinsic biophysical properties between the different cell-types from the mice used. This was also true for the evoked postsynaptic responses. In this study no receptor antagonists were employed and consequently analysed recordings were a mixed combination of excitatory and inhibitory responses. The situation is further complicated in this study since, although the MeCP2 status of the recorded postsynaptic cell can be established, the presynaptic status cannot. This problem could be overcome in future experiments through the use of paired recordings.

Symptom onset has been timed at between 4 and 12 months in *Mecp2*$^{Stop/+}$ mice (Guy *et al*. 2007). The appearance and severity of symptoms in heterozygous RTT female mice is highly variable. The majority of 'stop' mice used in this study were in the presymptomatic age range although several were in the peri-symptomatic age range and one was in the symptomatic age range. However, no overt symptoms, such as hind-limb clasping were observed in any of the mice used. Hence it is not surprising that no significant differences were found between the different cell types. At the same time it is quite possible that differences were present but too subtle to be detected in the experiments carried out and the cohort of mice used. Such subtle differences may show up with larger sample numbers and if evoked responses were biochemically isolated in order to separate excitatory from inhibitory effects. For example, GABA receptors can be blocked using bicuculline and CGP-55845 ((2S)-3-(1S)-1-(3,4-Dichlorophenyl) ethyl amino-2-hydroxypropyl-phenylmethyl-phosphinic acid).

AMPA receptor responses can then be isolated from NMDA receptor responses by treatment of the slice with the NMDA receptor antagonist APV (2*R*)-amino-5-phosphonopentanoate). Similarly, NMDA receptor responses can be isolated from AMPA receptor responses using CNQX. Blocking was not carried out in this study mainly because of time constraints, and also the initial aims were simply to acquire baseline data with the intention of expanding on this at a later stage.

One of a few studies including heterozygous female RTT mice previously reported was by Taneja *et al*. (2009) who investigated some of the electrophysiological properties of *locus ceruleus* (LC) cells from *Mecp2*$^{tm1.1Jae}$ mice. That particular strain has a brain-specific conditional KO of *Mecp2* exon 3 (Chen *et al*. 2001). Taneja *et al*. (2009) measured properties of LC cells from Mecp2-null and from females heterozygous for *Mecp2 i.e*. MeCP2+ve and MeCP2-ve cells, and compared them to WT. Under conditions of synaptic blockade they measured the frequency-current responses of the four cell types. They found that cells from *Mecp2*-null and MeCP2-ve cells had a similar frequency-current curve slope which was greater and significantly different compared to WT and MeCP2+ve cells. That reported result differs from this study where no such difference was observed for CA1 pyramidal cells, although no synaptic blockade was employed here. However, the differences reported in LC cells could be related to the particular cell type and brain region. Also, Taneja *et al*. (2009) used mice in the age range of 35-50 days for the heterozygous females and 26-35 days for the *Mecp2*-null males. At these ages the heterozygous females would likely have been symptom-free whereas the null males would have been peri-symptomatic (Guy *et al*. 2007). In a similar study of LC neurons Zhang *et al*. (2010a) compared peak and steady-state firing rates between Mecp2-null and WT mice (aged 3-4 weeks) but found no differences. This also appears to differ from Taneja *et al*.'s results although slightly younger mice were used by Zhang *et al*. (2009).

Using extracellular LTP induction protocols on hippocampal slices Guy *et al*. (2007) found no difference in the strength of basal synaptic transmission (stimulation-response curves) between presymptomatic and symptomatic Mecp2$^{+/-}$ female mice and WT controls. Similarly, they found no difference between presymptomatic and WT females in terms of applied LTP protocols. However, LTP was significantly reduced in symptomatic females and responses were similar to *Mecp2*-null mice. LTP in rescued Mecp2$^{stop/+}$ mice was indistinguishable from WT controls. LTP protocols reflect properties of the hippocampal network in acute slices and the overall network responses could be different to that of individual cells. The lack of difference with LTP responses between WT and presymptomatic Mecp2$^{+/-}$ females agrees with the findings of this study where no significant differences in short term synaptic plasticity between MeCP2+ve and MeCP2-ve cells were observed.

10 Suggested Future Work

Belichenko *et al*. (2009a) observed differences between MeCP2+ve and MeCP2-ve cortical pyramidal cells in terms of spine density, spine morphology and dendritic morphology. Those types of differences were also observed between all heterozygous cells compared to WT. Such differences would be expected to impact on cellular and network synaptic properties. The female mice used by Belichenko et al. were aged 6-7 months and symptomatic. This suggests that future whole-cell work should focus on symptomatic female animals. However, the situation may prove to be complex. Chapleau *et al*. (2012) have reported that, at the optical level, dendritic spine density and morphology was comparable in CA1 pyramidal cells from WT and symptomatic Mecp2$^{tm1.1Jae}$ mutant male mice whereas as cells from human female RTT patients *do* exhibit lower dendritic spine density. Their result in mice would seem to conflict with other studies but Chapleau *et al*. (2012) suggest that the genetic background of experimental RTT mice strains could be an important factor contributing towards differing results. Alternatively, variance could be caused by other factors e.g. variations across individual cells caused by activity-dependent phosphorylation (Cohen *et al*. 2011). This would seem to be difficult to control.

This study has not shown any evidence of differences in cellular electrophysiological properties in the mice used. To optimise the likelihood of observing any differences between the cell types in the *Mecp2*-mosaic hippocampus, the use of a cohort of mature adult RTT female mice which have been symptom scored to ensure that they are definitely symptomatic is indicated. Then these could be compared with age-matched WT mice. This has been previously done with extracellular LTP studies which have shown deficits in symptomatic heterozygous mice. Therefore investigating symptomatic mice at the cellular level may reveal differences between MeCP2+ve and MeCP2-ve cells in the *Mecp2*-mosaic hippocampus. However, since pyramidal cells, even those located just in the CA1, are not entirely homogenous in their characteristics it may be necessary to record a much larger number of cells than has been

achieved in this study in order to smooth out variability as well as to increase power. It would be anticipated that by applying PPF whole-cell protocols to cells from symptomatic mice, any observed deficits in synaptic function would likely be related to Ca^{2+} mobilisation and/or changes in the probability of neurotransmitter release. LTP protocols can also be used at the whole-cell level (Meredith *et al*. 2003, Gray *et al*. 2007) so similar protocols could be also applied to cells from symptomatic female RTT mice. Interestingly, it has recently been reported that LTP requires several SNARE complex proteins for *postsynaptic* AMPAR delivery (Jurado et al. 2013). Therefore measuring isolated AMPA responses using an LTP protocol may prove fruitful.

If any synaptic deficits are found in symptomatic females then further future work should include isolation of excitatory and inhibitory responses using a synaptic blockade. Additionally, paired recordings should be obtained so that the MeCP2 status of the presynaptic cell can also be identified in slices from *Mecp2*$^{-/+}$ mice. This would allow the various pre- and postsynaptic combinations of MeCP2+ve and MeCP2-ve cells to be investigated.

The functional status of Mecp2-mosaic hippocampal GABAergic interneurons in RTT mice also remains to be investigated as does the potential contribution of astroglia in the *Mecp2*-mosaic hippocampus. The interplay between excitatory glutamatergic neurons and inhibitory GABAergic interneurons inevitably has an effect on E/I balance and network properties. Either an increase in glutamatergic drive or decrease in GABAergic drive could potentially lead to hyperexcitability. An E/I imbalance can lead to seizure-like events or a tendency in that direction. Using a combination of simulation and experiment Demont-Guignard et al (2012) have investigated the mechanisms which underlie epileptiform events (Fast ripples and epileptic spikes) in the CA1. They found that, in simulation, the balance between glutamatergic (NMDA and AMPA) and GABAergic transmission determined whether low-amplitude spikes, fast ripples, high-amplitude spikes, or ictal-like activity was produced. They validated their model experimentally using organotypic hippocampal slices. Also, since selective

KO of MeCP2 from GABAergic neurons results in an RTT-like phenotype measuring the intrinsic and synaptic properties of GABAergic neurons in the *Mecp2*-mosaic hippocampus is indicated.

10.1 NMDA Subunit Hypothesis

It has recently been reported that LTP at WT CA1 synapses requires both GluN2A and Glun2B NMDAR subunits. Moreover, that the transient phase of LTP (which the authors refer to as 'STP') can be pharmacologically separated into two components, with one component requiring the GluN2A subunit and another component requiring GluN2B and GluN2D (Volianskis *et al*. 2013). Clearly the NMDAR subunit situation with respect to LTP is complex. Müller et al. (2013) have measured enhanced protocol-dependent LTP but unchanged LTD in rats with induced *status ellipticus*. They measured an increased NR2B/NR2A (GluN2B/2A) ratio in epileptic tissue. This was due to an upregulation of NR2B whilst NR2A remained unchanged but increased numbers of NR2B-containing receptors may be extrasynaptic. The increased NR2B is associated with an LTP/LTD imbalance resulting in impaired learning and memory.

With reference to the differential expression of NMDA receptor subunits discussed earlier (6.4), it could be hypothesised that MeCP2-deficient pyramidal neurons in mature/symptomatic female heterozygous $Mecp2^{+/-}$ (in the CA1) might express a prevalence of the immature-associated GluN2B NMDA receptor subunits over the GluN2A subunits. This could be a potential area of study should any synaptic deficits be identified from future investigations. In which case, it would be expected that the MeCP2-deficient neurons in symptomatic mice would display altered EPSC kinetics that would be more sensitive to the presence of Ifenprodil (see "Altered Postsynaptic Kinetics" in the literature review) or the more selective Ro 25-6981. If present, this should be easier to demonstrate initially in male Mecp2-null mice. The altered kinetics would probably only be

apparent in the presence of an antagonist such as NBQX to block AMPA receptor responses. Also, it would be expected that MeCP2-deficient neurons would fail to show an increase in the NMDA EPSC following LTP but that this deficit could be ameliorated by the presence of BDNF. The ratio of GluN2A/2B subunits may vary from cell to cell, however. Conversely, it would be expected that the opposite characteristics would be observed in MeCP2+ve cells - providing there was no significant non-cell autonomous influence from surrounding MeCP2-ve cells (neurons and glia). Similarly, MeCP2-ve cells surrounded by MeCP2+ve ones could be in receipt of influence from the +ve cells, so it may be advisable to seek out isolated –ve cells for investigation. A future experiment using the protocol of Bellone & Nicoll (2007) could be used to investigate the influence of MeCP2 on synaptic properties by comparing young / presymptomatic / symptomatic heterozygous $Mecp2^{+/-}$ mice with age-matched WT controls. The relative contributions towards levels of the GluN2A and GluN2B subunits could be imaged using immunogold staining with electron microscopy following the method of (Das *et al.*, 2010). If any NMDA sub-unit related dysfunction is confirmed in heterozygous $Mecp2^{+/-}$ mice, the sub-units could indicate the location of a potential pharmacological target.

11 Conclusions

In conclusion, the results obtained in this study are comparable to most other similar studies and demonstrate that there are no significant differences in electrophysiological properties of CA1 pyramidal cells between WT, MecP2+ve and Mecp2-ve individual neurons in presymptomatic heterozygous RTT mice. The data obtained in this study provides a baseline which adds to the body of knowledge regarding RTT pathophysiology, and which can be used as a reference point for future work. The age, developmental stage and symptom status are clearly important factors – Nguyen et al. (2012) reported that induced loss of MeCP2 in either late juvenile or adult mice results in a similar symptom progression to germline mutants in respect of RTT-like symptoms in both male and female mice. Hence, it is suggested that it is the symptom status rather than absolute age which should be the criteria to use in selection of mice for future investigations.

12 Appendix 1. Clampex Recording Protocols

12.1 Current Clamp Protocol to Elicit Action Potentials

```
Protocol: C:\Documents and Settings\rig1\My Documents\Molecular
Devices\pCLAMP\Params\Aptuit\Protocol 1 (5 x 11)(-250 - +250).pro
Data File: Protocol 1 (5 x 11)(-250 - +250)
File format: ABF V2.00
Created: Feb 9, 2010, at 12:52:43.718 [03:34:34]
Created by: clampex 10.2.0.14
Modified by: clampex 10.2.0.14
Acquisition mode: episodic stimulation.
Axon binary file (integer)
Comment: n/a


Experiment type: other.
File GUID:       {C931BE3F-1757-40E6-AF6B-C1790D74003F}.

Input signal: _Ipatch (#0).    Telegraphs disabled.
Input signal: Voltagein (#1).    Telegraphs disabled.
Trial length: 11 sweeps of 1200.0 ms (24000 samples per channel).
Minimum time between run starts.
3.000 s between sweep starts.
Sampling rate:  20.00 kHz (interval 50.00 µs).

Input signals: _Ipatch (#0) and Voltagein (#1).

Signal VoltageOu (#0) holding level: 0.00 mV.
Signal CurrentOU (#1) holding level: 0.00 nA.
Signal Cmd 2 (#2) holding level: 0.00 mV.
Signal Cmd 3 (#3) holding level: 0.00 mV.

Analog Output #0
Waveform: disabled.

EPOCH                    A      B      C      D      E      F      G
H      I      J
Type                     Off    Off    Off    Off    Off    Off    Off
Off    Off    Off
Sample rate              Fast   Fast   Fast   Fast   Fast   Fast   Fast
Fast   Fast   Fast
First duration (samples) 0      0      0      0      0      0      0
0      0      0
Delta duration (samples) 0      0      0      0      0      0      0
0      0      0
First duration (ms)      0.0    0.0    0.0    0.0    0.0    0.0    0.0
0.0    0.0    0.0
Delta duration (ms)      0.0    0.0    0.0    0.0    0.0    0.0    0.0
0.0    0.0    0.0
Digital Out pattern: disabled.
Pre-sweep train: disabled.
Leak subtraction: disabled.
User list: disabled.

Analog Output #1
Waveform:
```

EPOCH	A	B	C	D	E	F	G	H	I	J
Type	Step	Step	Off	Off	Off	Off	Off	Off	Off	Off
Sample rate	Fast	Fast	Fast	Fast	Fast	Fast	Fast	Fast	Fast	Fast
First level (nA)	0	-0.25	0	0	0	0	0	0	0	0
Delta level (nA)	0	0.05	0	0	0	0	0	0	0	0
First duration (samples)	1000	10000	0	0	0	0	0	0	0	0
Delta duration (samples)	0	0	0	0	0	0	0	0	0	0
First duration (ms)	50.0	500.0	0.0	0.0	0.0	0.0	0.0	0.0	0.0	0.0
Delta duration (ms)	0.0	0.0	0.0	0.0	0.0	0.0	0.0	0.0	0.0	0.0
Train Period (samples)	0	0	0	0	0	0	0	0	0	0
Pulse Width (samples)	0	0	0	0	0	0	0	0	0	0
Train Rate (Hz)	0.00	0.00	0.00	0.00	0.00	0.00	0.00	0.00	0.00	0.00
Pulse Width (ms)	0.0	0.0	0.0	0.0	0.0	0.0	0.0	0.0	0.0	0.0

Intersweep holding: same as for signal CurrentOU (#1).

12.2 Current Clamp -10pA Pulse Protocol

Protocol: C:\Documents and Settings\rig1\My Documents\Molecular Devices\pCLAMP\Params\Aptuit\Protocol 2 1x10pA x 30.pro
Data File: Protocol 2 1x10pA x 30
File format: ABF V2.00
Created: Feb 10, 2010, at 15:08:28.390 [01:39:39]
Created by: clampex 10.2.0.14
Acquisition mode: episodic stimulation.
Axon binary file (integer)
Comment: n/a

Experiment type: other.
File GUID: {54344AF6-90E7-48C8-B56E-9306E1677FFD}.

Input signal: _Ipatch (#0). Telegraphs disabled.
Input signal: Voltagein (#1). Telegraphs disabled.
Trial length: 30 sweeps of 1000.0 ms (20000 samples per channel).
Minimum time between run starts.
3.000 s between sweep starts.
Sampling rate: 20.00 kHz (interval 50.00 µs).

Input signals: _Ipatch (#0) and Voltagein (#1).

Signal VoltageOu (#0) holding level: 0.00 mV.
Signal CurrentOU (#1) holding level: 0.00 nA.

```
Signal Cmd 2 (#2) holding level: 0.00 mV.
Signal Cmd 3 (#3) holding level: 0.00 mV.

Analog Output #0
Waveform: disabled.

EPOCH                    A      B      C      D      E      F      G
H      I      J
Type                     Off    Off    Off    Off    Off    Off    Off
Off    Off    Off
Sample rate              Fast   Fast   Fast   Fast   Fast   Fast   Fast
Fast   Fast   Fast
First duration (samples) 0      0      0      0      0      0      0
0      0      0
Delta duration (samples) 0      0      0      0      0      0      0
0      0      0
First duration (ms)      0.0    0.0    0.0    0.0    0.0    0.0    0.0
0.0    0.0    0.0
Delta duration (ms)      0.0    0.0    0.0    0.0    0.0    0.0    0.0
0.0    0.0    0.0
Digital Out pattern: disabled.
Pre-sweep train: disabled.
Leak subtraction: disabled.
User list: disabled.

Analog Output #1
Waveform:
EPOCH                    A      B      C      D      E      F      G
H      I      J
Type                     Step   Step   Off    Off    Off    Off    Off
Off    Off    Off
Sample rate              Fast   Fast   Fast   Fast   Fast   Fast   Fast
Fast   Fast   Fast
First level (nA)         0      -0.01  0      0      0      0      0
0      0      0
Delta level (nA)         0      0      0      0      0      0      0
0      0      0
First duration (samples) 1000   10000  0      0      0      0      0
0      0      0
Delta duration (samples) 0      0      0      0      0      0      0
0      0      0
First duration (ms)      50.0   500.0  0.0    0.0    0.0    0.0    0.0
0.0    0.0    0.0
Delta duration (ms)      0.0    0.0    0.0    0.0    0.0    0.0    0.0
0.0    0.0    0.0
Train Period (samples)   0      0      0      0      0      0      0
0      0      0
Pulse Width (samples)    0      0      0      0      0      0      0
0      0      0
Train Rate (Hz)          0.00   0.00   0.00   0.00   0.00   0.00   0.00
0.00   0.00   0.00
Pulse Width (ms)         0.0    0.0    0.0    0.0    0.0    0.0    0.0
0.0    0.0    0.0
Intersweep holding: same as for signal CurrentOU (#1).
```

12.3 Voltage Clamp Paired Pulse Protocol (25ms Inter-pulse Interval)

```
Protocol: C:\Documents and Settings\rig1\My Documents\Molecular
Devices\pCLAMP\Params\Aptuit\PP0.5ms Synaptic25-2.pro
Data File: PP0.5ms Synaptic25-2
File format: ABF V2.00
Created: Jan 11, 2010, at 17:58:50.453 [00:15:41]
Created by: Clampex 10.2.0.14
Acquisition mode: episodic stimulation.
Axon binary file (integer)
Comment: n/a


Experiment type: other.
File GUID:       {244CA333-FE7C-44A4-B640-4BAAB5D96FAD}.

Input signal: IN 0 (#0).    Telegraphs disabled.
Input signal: IN 1 (#1).    Telegraphs disabled.
Trial length: 1 sweep of 250.0 ms (5000 samples per channel).
Minimum time between run starts.
Minimum time between sweep starts.
Sampling rate:  20.00 kHz (interval 50.00 µs).

Input signals: IN 0 (#0) and IN 1 (#1).

Signal VoltageOu (#0) holding level: 0.00 mV.
Signal OUT 1 (#1) holding level: 0.00 V.
Signal OUT 2 (#2) holding level: 0.00 V.
Signal OUT 3 (#3) holding level: 0.00 V.

Analog Output #0
Waveform:
EPOCH                    A      B      C      D      E      F      G
H      I      J
Type                     Step   Step   Off    Off    Off    Off    Off
Off    Off    Off
Sample rate              Fast   Fast   Fast   Fast   Fast   Fast   Fast
Fast   Fast   Fast
First level (mV)         0      5      0      0      0      0      0
0      0      0
Delta level (mV)         0      0      0      0      0      0      0
0      0      0
First duration (samples) 4000   500    0      0      0      0      0
0      0      0
Delta duration (samples) 0      0      0      0      0      0      0
0      0      0
First duration (ms)      200.0  25.0   0.0    0.0    0.0    0.0    0.0
0.0    0.0    0.0
Delta duration (ms)      0.0    0.0    0.0    0.0    0.0    0.0    0.0
0.0    0.0    0.0
Train Period (samples)   0      0      0      0      0      0      0
0      0      0
Pulse Width (samples)    0      0      0      0      0      0      0
0      0      0
```

```
Train Rate (Hz)          0.00   0.00   0.00   0.00   0.00   0.00   0.00
0.00   0.00   0.00
Pulse Width (ms)         0.0    0.0    0.0    0.0    0.0    0.0    0.0
0.0    0.0    0.0
Intersweep holding: same as for signal VoltageOu (#0).

Digital Out pattern: disabled.
Pre-sweep train: disabled.
Leak subtraction: disabled.
User list: disabled.

Analog Output #1
Waveform: disabled.

EPOCH                    A      B      C      D      E      F      G
H      I      J
Type                     Off    Off    Off    Off    Off    Off    Off
Off    Off    Off
Sample rate              Fast   Fast   Fast   Fast   Fast   Fast   Fast
Fast   Fast   Fast
First duration (samples) 0      0      0      0      0      0      0
0      0      0
Delta duration (samples) 0      0      0      0      0      0      0
0      0      0
First duration (ms)      0.0    0.0    0.0    0.0    0.0    0.0    0.0
0.0    0.0    0.0
Delta duration (ms)      0.0    0.0    0.0    0.0    0.0    0.0    0.0
0.0    0.0    0.0
Pre-sweep train: disabled.
Leak subtraction: disabled.
User list: disabled.

Analog Output #2
Waveform: disabled.

EPOCH                    A      B      C      D      E      F      G
H      I      J
Type                     Off    Off    Off    Off    Off    Off    Off
Off    Off    Off
Sample rate              Fast   Fast   Fast   Fast   Fast   Fast   Fast
Fast   Fast   Fast
First duration (samples) 0      0      0      0      0      0      0
0      0      0
Delta duration (samples) 0      0      0      0      0      0      0
0      0      0
First duration (ms)      0.0    0.0    0.0    0.0    0.0    0.0    0.0
0.0    0.0    0.0
Delta duration (ms)      0.0    0.0    0.0    0.0    0.0    0.0    0.0
0.0    0.0    0.0
Pre-sweep train: disabled.
Leak subtraction: disabled.
User list: disabled.

Analog Output #3
Waveform:
EPOCH                    A      B      C      D      E      F      G
H      I      J
Type                     Step   Step   Step   Step   Off    Off    Off
Off    Off    Off
Sample rate              Fast   Fast   Fast   Fast   Fast   Fast   Fast
Fast   Fast   Fast
```

```
First level (V)           0      5      0      5      0      0      0
0      0      0
Delta level (V)           0      0      0      0      0      0      0
0      0      0
First duration (samples) 500     10     500     10     0      0      0
0      0      0
Delta duration (samples) 0       0      0      0      0      0      0
0      0      0
First duration (ms)       25.0   0.5    25.0   0.5    0.0    0.0    0.0
0.0    0.0    0.0
Delta duration (ms)       0.0    0.0    0.0    0.0    0.0    0.0    0.0
0.0    0.0    0.0
Train Period (samples)    0      0      0      0      0      0      0
0      0      0
Pulse Width (samples)     0      0      0      0      0      0      0
0      0      0
Train Rate (Hz)           0.00   0.00   0.00   0.00   0.00   0.00   0.00
0.00   0.00   0.00
Pulse Width (ms)          0.0    0.0    0.0    0.0    0.0    0.0    0.0
0.0    0.0    0.0
Intersweep holding: same as for signal OUT 3 (#3).

Pre-sweep train: disabled.
Leak subtraction: disabled.
User list: disabled.


Statistics measurements: enabled.

Channel math: disabled.
No pre-sweep train.
Auto analysis: default
```

12.4 Voltage Clamp Frequency Pulse Train Protocol (10 Pulses at 10Hz)

```
Protocol: C:\Documents and Settings\rig1\My Documents\Molecular
Devices\pCLAMP\Params\LTP_LW\Conditioning10.pro
Data File: Conditioning10
File format: ABF V2.00
Created: n/a
Created by:  pre-9.0
Acquisition mode: episodic stimulation.
Axon binary file (integer)
Comment: n/a

Experiment type: other.
File GUID:       {136FD9BB-83D5-4A22-9E1E-5C6C71C6C9B5}.

Input signal: IN 0 (#0).    Telegraphs disabled.
Trial length: 10 sweeps of 1100.0 ms (22000 samples).
Minimum time between run starts.
10.000 s between sweep starts.
Sampling rate:  20.00 kHz (interval 50.00 µs).

Input signal: IN 0 (#0).

Signal Cmd 0 (#0) holding level: 0.00 mV.
Signal Cmd 1 (#1) holding level: 0.00 mV.
Signal _Cmd 2 (#2) holding level: 0.00 mV.
Signal _Cmd 3 (#3) holding level: 0.00 mV.

Analog Output #0
Waveform:
EPOCH                    A      B      C      D      E      F      G
H      I      J
Type                     Off    Step   Off    Off    Off    Off    Off
Off    Off    Off
Sample rate              Fast   Fast   Fast   Fast   Fast   Fast   Fast
Fast   Fast   Fast
First duration (samples) 0      20000  0      0      0      0      0
0      0      0
Delta duration (samples) 0      0      0      0      0      0      0
0      0      0
First duration (ms)      0.0    1000.0 0.0    0.0    0.0    0.0    0.0
0.0    0.0    0.0
Delta duration (ms)      0.0    0.0    0.0    0.0    0.0    0.0    0.0
0.0    0.0    0.0
Digital pattern #3-0     0000   000*   0000   0000   0000   0000   0000
0000   0000   0000
Digital pattern #7-4     0000   0000   0000   0000   0000   0000   0000
0000   0000   0000   Digital train active logic: 1.

Digital Out holding: 0000; Holding value used for intersweep pattern.
Pre-sweep train: disabled.
Leak subtraction: disabled.
User list: disabled.
```

13 Appendix 2 - Representative Recordings from Single Cells

The following figures are traces or plots taken from recordings of single cells. As such the plots do not include error bars.

Fig. 13-1 shows current clamp recordings from a WT, HetP and HetN cell which have been injected with hyperpolarising and depolarising current injections over the range -250pA to +250pA with a step value of 50pA. This was the standard protocol used for all current clamp recordings. For clarity, only responses from 5 of the 11 current steps are shown with just the action potentials elicited at +250pA.

Fig. 13-2 shows plots of voltage responses against hyperpolarising current steps used to determine peak and steady state responses for each of the cell types. The slopes of the graphs reflect the non-resting input resistance of the cells from Ohm's Law, R=V/I. All the plots have good straight line fits.

Fig. 13-3 shows action potential discharge frequency against depolarising current steps over the range 0pA to +250pA. The plots show that there is some variability for individual cells.

Fig. 13-4 are plots of calculated paired-pulse facilitation ratios over the inter-stimulus interval range of 25ms – 500ms for individual cells of each type. The general pattern of reduction in ratio with increasing interval is similar for each cell.

Fig. 13-5 shows plots of measured voltage clamp responses to trains of 10 stimuli at frequencies in the range 5Hz to 40Hz for each cell type. Responses are normalised to the first response in the train. Patterns can be quite variable for individual cells but all show facilitation.

Figs. 13-6 and 13.7 are representative example traces of frequency facilitation from single cells. Fig. 13-6 are traces recorded at a stimulus frequency of 40Hz for each cell type. Fig. 13-7 shows the responses to 5Hz, 10Hz, 20Hz and 40Hz stimuli for a single WT cell.

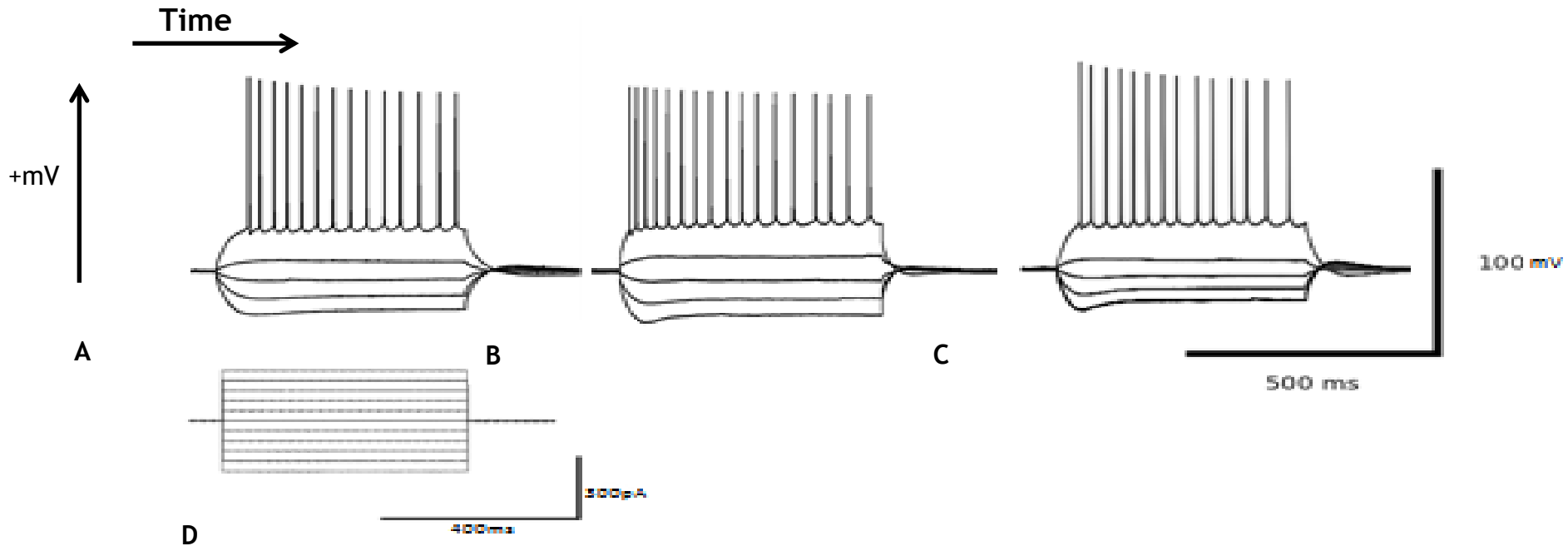

Figure 13-1 Representative examples of recorded current clamp traces

Responses to injected hyperpolarising and depolarising current pulses (-250 to +250pA, 50pA step, 500ms pulse width). For clarity, only responses to 5 out of 11 injected pulses are shown. A) From a heterozygous MeCP2+ve cell, B) From a heterozygous MeCP2-ve cell, and C) From a WT cell. D shows a set of 11 injected current pulses. Recordings are from individual cells i.e. n=1 in each case.

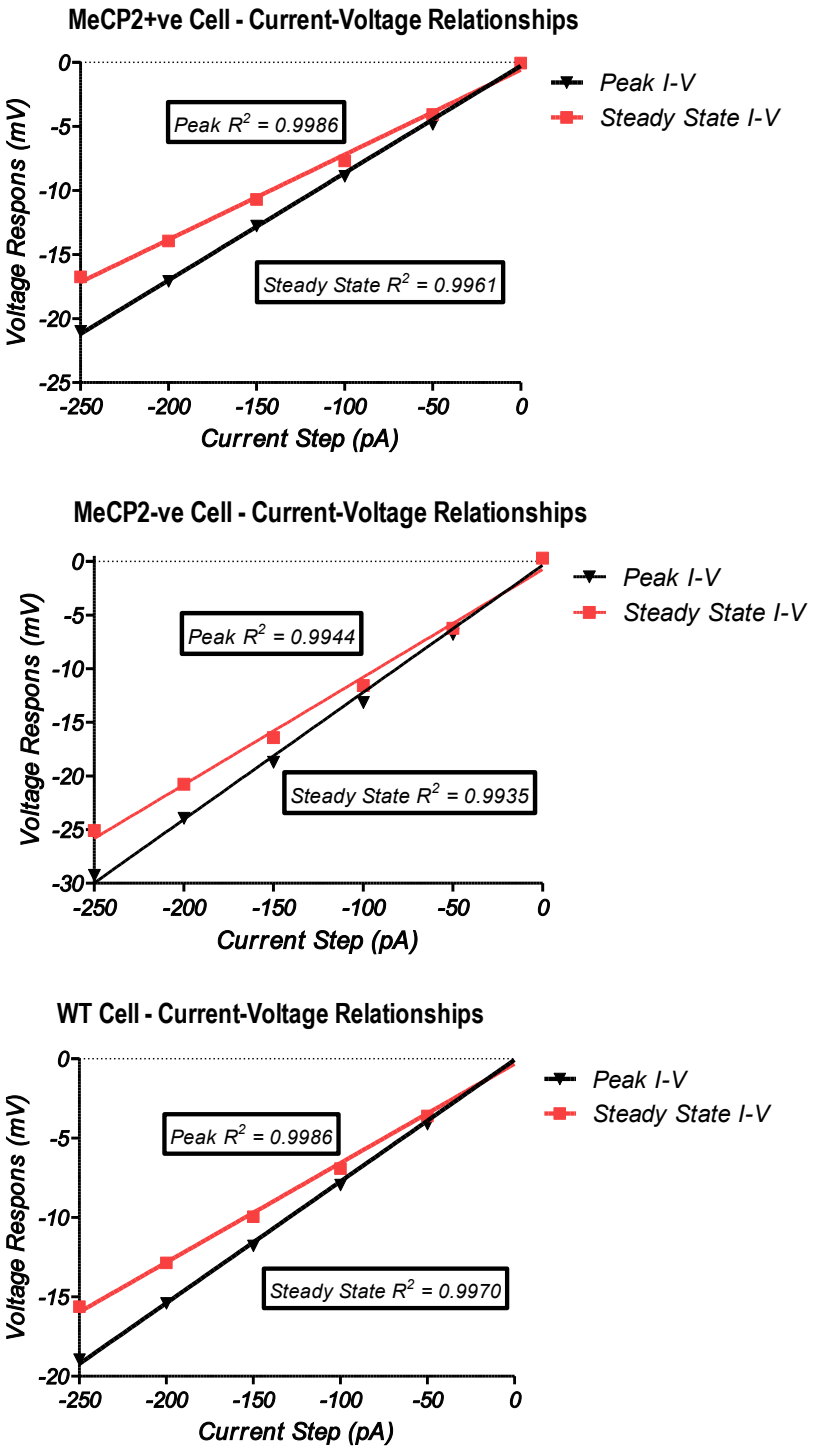

Figure 13-2 Representative examples of current-voltage relationships. Plots show voltage responses to hyperpolarising current injections in the range 0 to -250pA for examples of individual cells. Peak and steady-state voltages are plotted on the same graphs. Lines are linear regression plots with R^2 values which reflect a good fit to straight line. Data are from individual cells i.e. n=1 in each case.

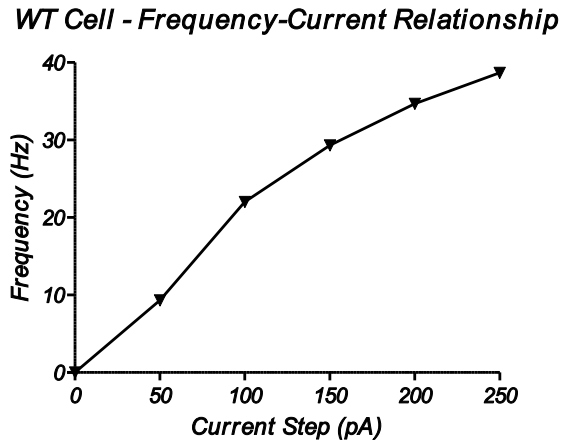

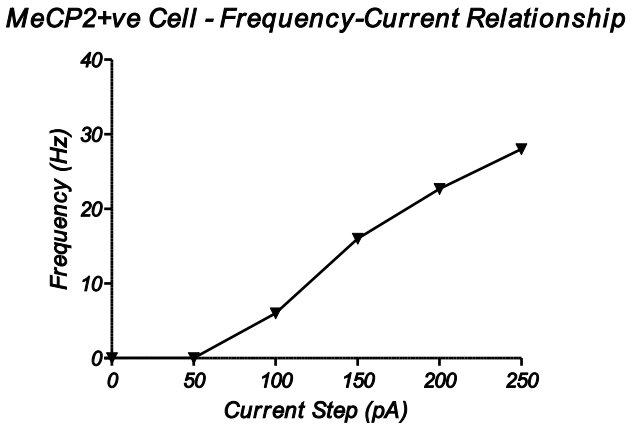

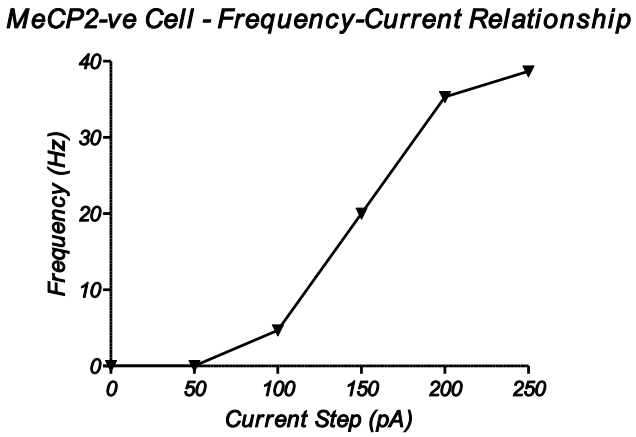

Figure 13-3 Representative examples of frequency-current relationships . Plots are action potential firing rates against depolarising injected current steps in the range 0-250pA, step 50pA for individual example cells. Data are from individual cells i.e. n=1 in each case.

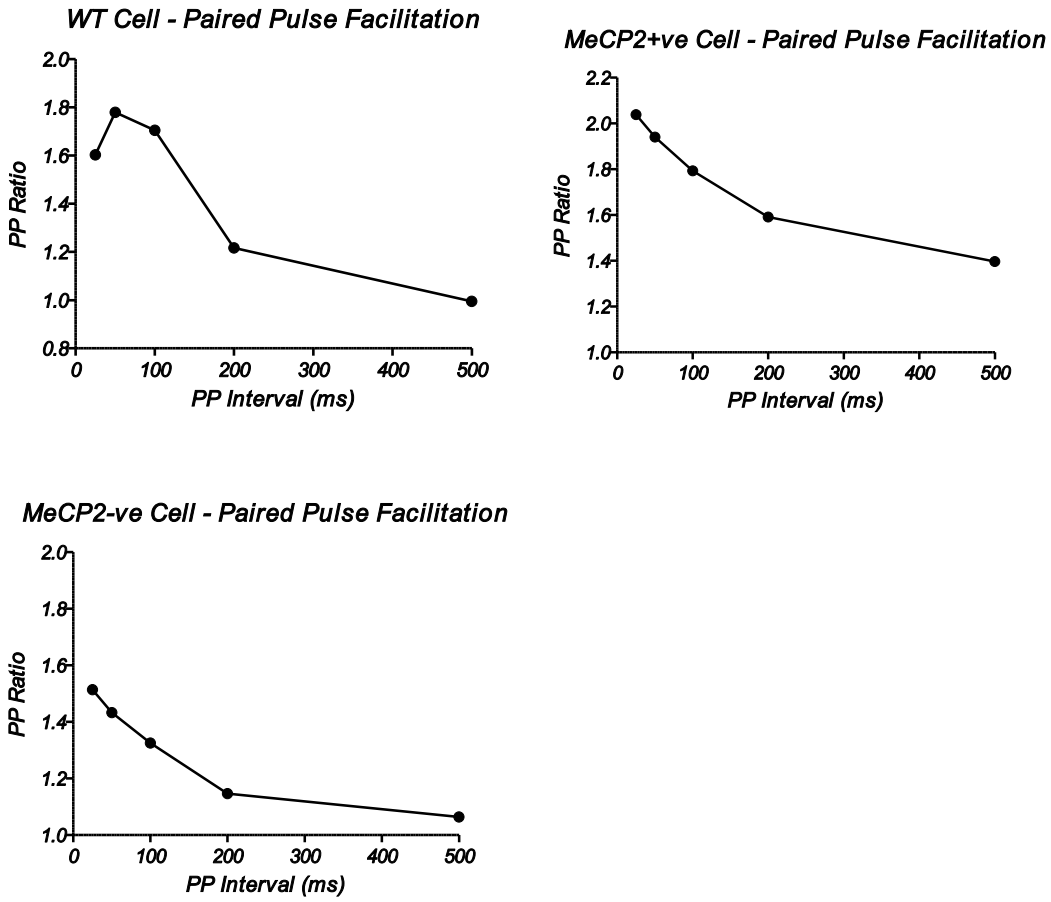

Figure 13-4 Examples of paired-pulse facilitation ratios against stimulus intervals. Paired-pulse ratios are plotted against stimulus interval for interstimulus times of 25, 50, 100, 200 and 500 ms for each of WT, MeCP2-ve and MeCP2+ve cells. The data shows how the paired-pulse ratio tends to 1 with increasing interstimulus intervals. Data are from individual cells i.e. n=1 in each case.

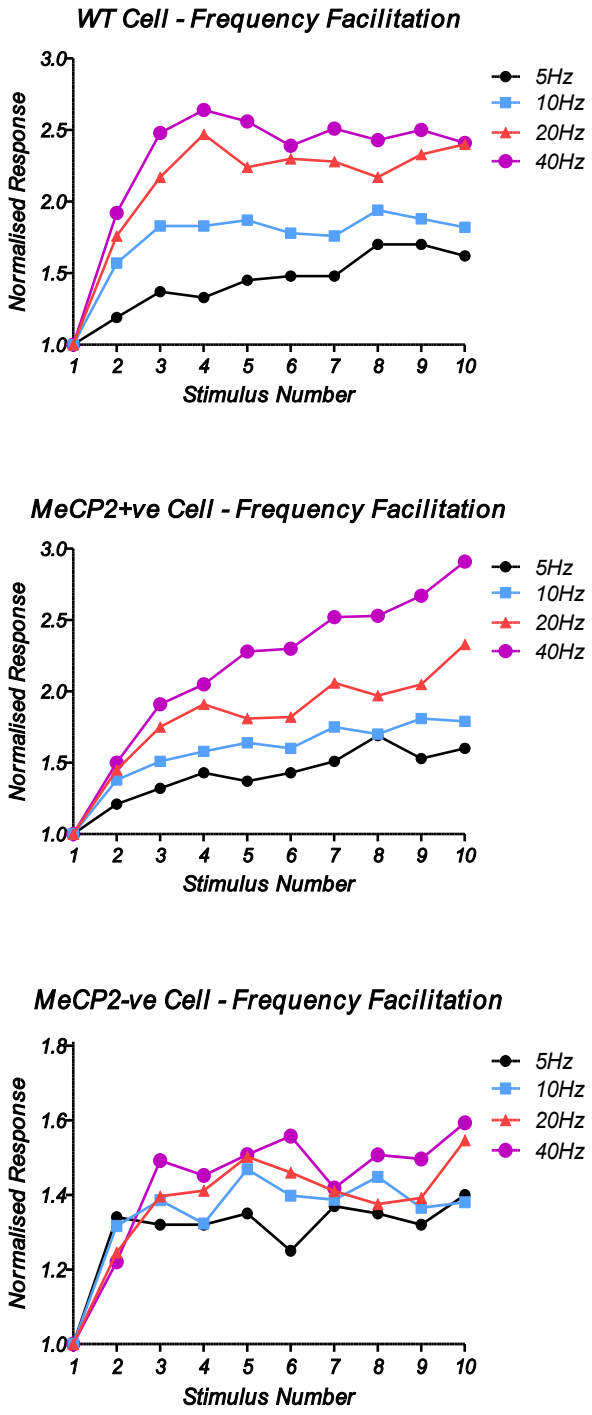

Figure 13-5 Examples of normalized frequency facilitation responses to trains of 10 stimuli at frequencies in the range 5-40Hz. Plots show mean normalized responses against stimulus number at frequencies of 5, 10,20 and 40Hz for each of WT, MeCP2+ve and MeCP2-ve cells. Response amplitudes were normalised to the response of the first stimulus. Data are from individual cells i.e. n=1 in each case.

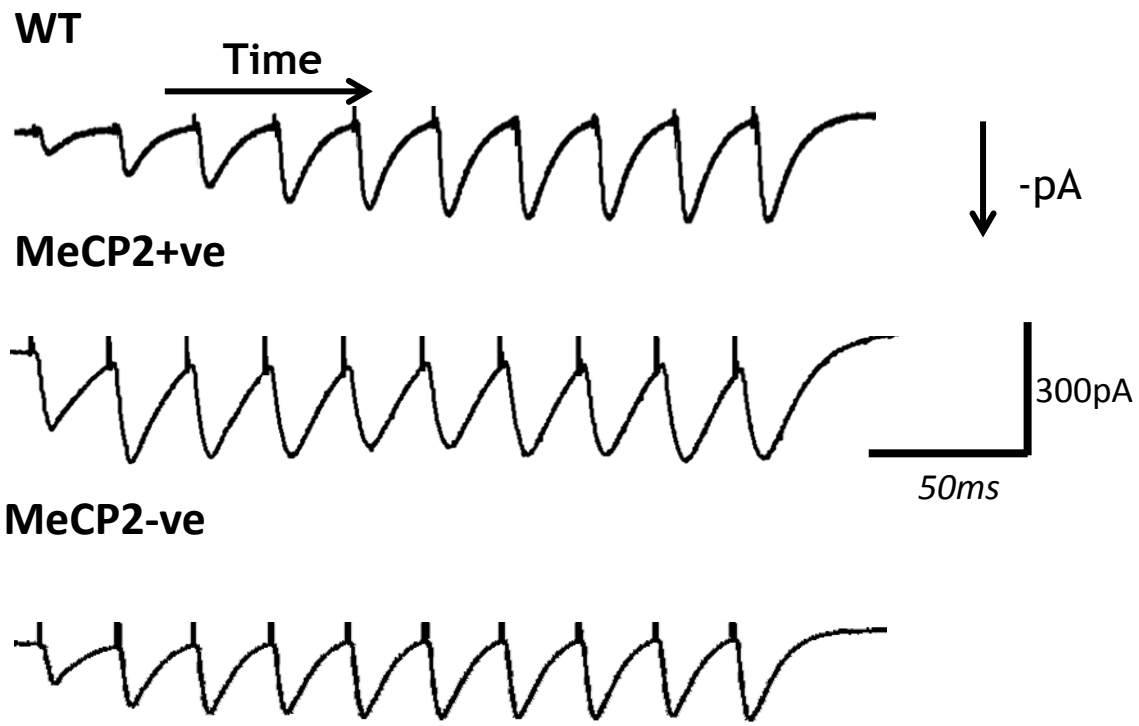

Figure 13-6 Examples of 40Hz Frequency Facilitation Traces. Stimulus artefacts have been cropped for clarity. Recordings are from individual cells i.e. n= 1 for each trace and averaged across 10 traces within Stimfit.

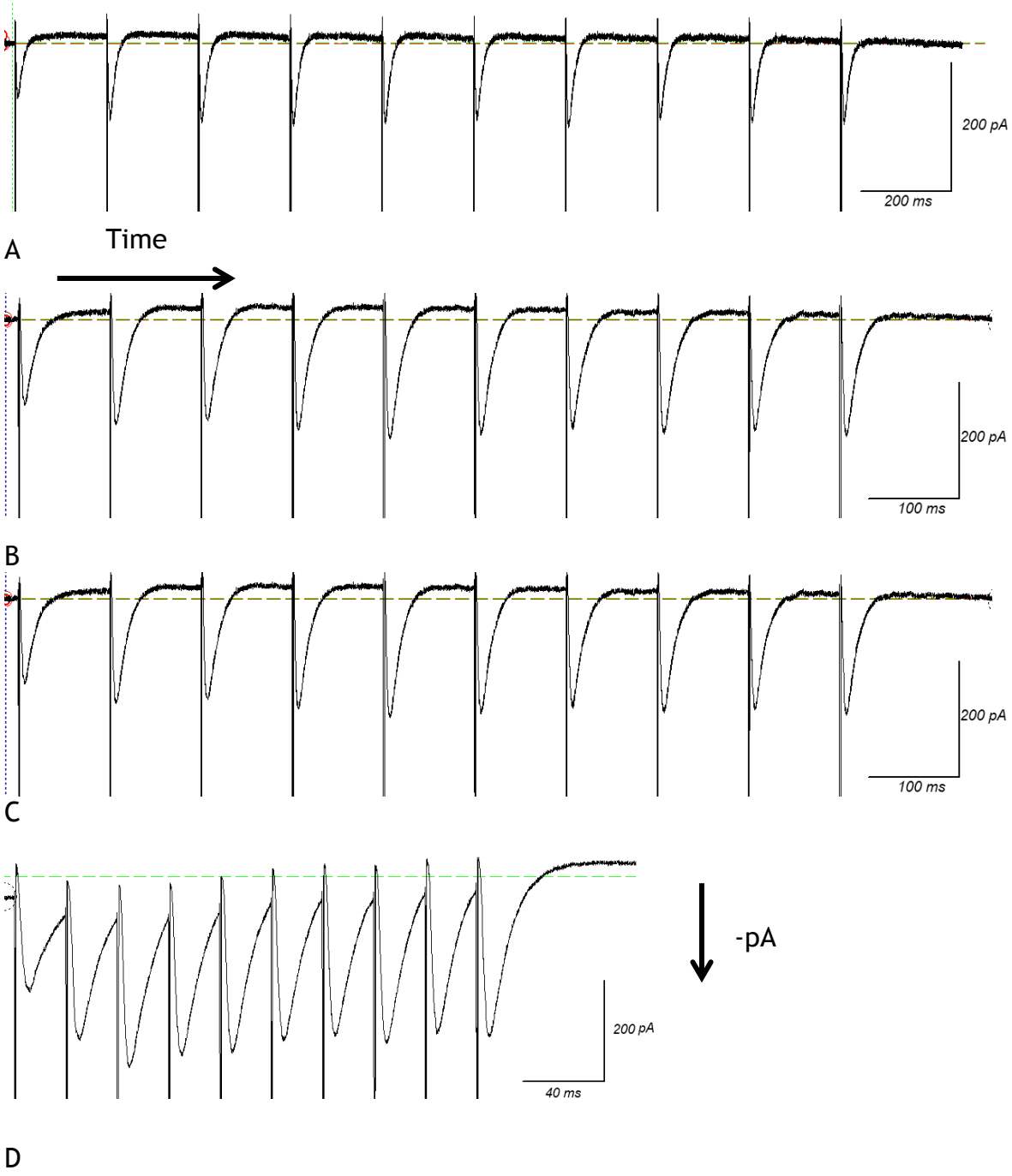

Figure 13-7 Example traces of frequency facilitation recordings (WT cell). Traces show responses from trains of 10 stimulation pulses. Stimulation frequencies were A – 5Hz, B – 10Hz, C- 20Hz, D – 40Hz. Each is the average of 10 traces with a 10 second gap between recordings. Patterns of facilitation are similar to those reported by Sun *et al.* (2005) for WT rat CA1 pyramidal cells. Recordings are from the same individual WT cell i.e. n= 1 for each trace.

14 Reference List

Abdala AP, Dutschmann M, Bissonnette JM, Paton JF (2010). Correction of respiratory disorders in a mouse model of Rett syndrome. *Proc Natl Acad Sci U S A* **107**, 18208-18213.

Adachi M, Autry AE, Covington HE, III, Monteggia LM (2009). MeCP2-mediated transcription repression in the basolateral amygdala may underlie heightened anxiety in a mouse model of Rett syndrome. *J Neurosci* **29**, 4218-4227.

Alvarez-Saavedra M, Carrasco L, Sura-Trueba S, Demarchi A, V, Walz K, Neto JX, Young JI (2010). Elevated expression of MeCP2 in cardiac and skeletal tissues is detrimental for normal development. *Hum Mol Genet* **19**, 2177-2190.

Ambros-Ingerson J & Holmes WR (2005). Analysis and comparison of morphological reconstructions of hippocampal field CA1 pyramidal cells. *Hippocampus* **15**, 302-315.

Amir RE, Van den Veyver IB, Wan M, Tran CQ, Francke U, Zoghbi HY (1999). Rett syndrome is caused by mutations in X-linked MECP2, encoding methyl-CpG-binding protein 2. *Nat Genet* **23**, 185-188.

Andersen P, Silfvenius H, Sundberg SH, Sveen O (1980). A comparison of distal and proximal dendritic synapses on CA1 pyramids in guinea-pig hippocampal slices in vitro. *J Physiol* **307**, 273-299.

Andersen P, Morris R, Amaral D, Bliss T, O'Keefe J (2007). *The Hippocampus Book*. Oxford University Press, New York.

Asaka Y, Jugloff DG, Zhang L, Eubanks JH, Fitzsimonds RM (2006). Hippocampal synaptic plasticity is impaired in the Mecp2-null mouse model of Rett syndrome. *Neurobiol Dis* **21**, 217-227.

Atallah BV & Scanziani M. (2009). Instantaneous modulation of gamma oscillation frequency by balancing excitation with inhibition. *Neuron* **62,** 566-77.

Ballas N, Lioy DT, Grunseich C, Mandel G (2009). Non-cell autonomous influence of MeCP2-deficient glia on neuronal dendritic morphology. *Nat Neurosci* **12**, 311-317.

Bannister NJ & Larkman AU (1995a). Dendritic morphology of CA1 pyramidal neurones from the rat hippocampus: I. Branching patterns. *J Comp Neurol* **360**, 150-160.

Bannister NJ & Larkman AU (1995b). Dendritic morphology of CA1 pyramidal neurones from the rat hippocampus: II. Spine distributions. *J Comp Neurol* **360**, 161-171.

Baroncelli L, Braschi C, Spolidoro M, Begenisic T, Maffei L, Sale A (2011). Brain plasticity and disease: a matter of inhibition. *Neural Plast* **2011**, 286073.

Bebbington A, Anderson A, Ravine D, Fyfe S, Pineda M, de KN, Ben-Zeev B, Yatawara N, Percy A, Kaufmann WE, Leonard H (2008). Investigating genotype-phenotype relationships in Rett syndrome using an international data set. *Neurology* **70**, 868-875.

Bekkers JM & Clements JD (1999). Quantal amplitude and quantal variance of strontium-induced asynchronous EPSCs in rat dentate granule neurons. *J Physiol* **516** (Pt 1), 227-248.

Bekkers JM & Stevens CF (1991). Excitatory and inhibitory autaptic currents in isolated hippocampal neurons maintained in cell culture. *Proc Natl Acad Sci U S A* **88**, 7834-7838.

Belichenko NP, Belichenko PV, Mobley WC (2009a). Evidence for both neuronal cell autonomous and nonautonomous effects of methyl-CpG-binding protein 2 in the cerebral cortex of female mice with Mecp2 mutation. *Neurobiol Dis* **34**, 71-77.

Belichenko PV, Wright EE, Belichenko NP, Masliah E, Li HH, Mobley WC, Francke U (2009b). Widespread changes in dendritic and axonal morphology in Mecp2-mutant mouse models of Rett syndrome: evidence for disruption of neuronal networks. *J Comp Neurol* **514**, 240-258.

Bellone C & Nicoll RA (2007). Rapid bidirectional switching of synaptic NMDA receptors. *Neuron* **55**, 779-785.

Bischofberger J, Engel D, Li L, Geiger JR, Jonas P (2006). Patch-clamp recording from mossy fiber terminals in hippocampal slices. *Nat Protoc* **1**, 2075-2081.

Blue ME, Kaufmann WE, Bressler J, Eyring C, O'driscoll C, Naidu S, Johnston MV (2011). Temporal and regional alterations in NMDA receptor expression in Mecp2-null mice. *Anat Rec (Hoboken)* **294**, 1624-1634.

Bourne JN & Harris KM (2012). Nanoscale analysis of structural synaptic plasticity. *Curr Opin Neurobiol*. **22**, 372–382

Braunschweig D, Simcox T, Samaco RC, LaSalle JM (2004). X-Chromosome inactivation ratios affect wild-type MeCP2 expression within mosaic Rett syndrome and Mecp2-/+ mouse brain. *Hum Mol Genet* **13**, 1275-1286.

Brown DR (1999). Neurons depend on astrocytes in a coculture system for protection from glutamate toxicity. *Mol Cell Neurosci* **13**, 379-389.

Calfa G, Hablitz JJ, Pozzo-Miller L (2011a). Network hyperexcitability in hippocampal slices from Mecp2 mutant mice revealed by voltage-sensitive dye imaging. *J Neurophysiol* **105**, 1768-1784.

Calfa G, Percy AK, Pozzo-Miller L (2011b). Experimental models of Rett syndrome based on Mecp2 dysfunction. *Exp Biol Med (Maywood)* **236**, 3-19.

Chao HT, Chen H, Samaco RC, Xue M, Chahrour M, Yoo J, Neul JL, Gong S, Lu HC, Heintz N, Ekker M, Rubenstein JL, Noebels JL, Rosenmund C, Zoghbi HY (2010). Dysfunction in GABA signalling mediates autism-like stereotypies and Rett syndrome phenotypes. *Nature* **468**, 263-269.

Chao HT, Zoghbi HY, Rosenmund C (2007). MeCP2 controls excitatory synaptic strength by regulating glutamatergic synapse number. *Neuron* **56**, 58-65.

Chapleau CA, Boggio EM, Calfa G, Percy AK, Giustetto M, Pozzo-Miller L (2012) Hippocampal CA1 Pyramidal Neurons of Mecp2 Mutant Mice Show a Dendritic Spine Phenotype Only in the Presymptomatic Stage. *Neural Plast*. **2012**, Article ID 976164, 1-9.

Chen RZ, Akbarian S, Tudor M, Rudolf Jaenisch R (2001) Deficiency of methyl-CpG binding protein-2 in CNS neurons results in a Rett-like phenotype in mice. *Nature Genetics* **27**, 327 - 331

Chevaleyre V & Siegelbaum SA (2010). Strong CA2 pyramidal neuron synapses define a powerful disynaptic cortico-hippocampal loop. *Neuron* **66**, 560-572.

Clark KA, Randall AD, Collingridge GL (1994). A comparison of paired-pulsed facilitation of AMPA and NMDA receptor-mediated excitatory postsynaptic currents in the hippocampus. *Exp Brain Res* **101**, 272-278.

Cohen S, Gabel HW, Hemberg M, Hutchinson AN, Sadacca LA, Ebert DH, Harmin DA, Greenberg RS, Verdine VK, Zhou Z, Wetsel WC, West AE, Greenberg ME (2011). Genome-wide activity-dependent MeCP2 phosphorylation regulates nervous system development and function. *Neuron* **72**, 72-85.

Collins AL, Levenson JM, Vilaythong AP, Richman R, Armstrong DL, Noebels JL, David SJ, Zoghbi HY (2004). Mild overexpression of MeCP2 causes a progressive neurological disorder in mice. *Hum Mol Genet* **13**, 2679-2689.

Cull-Candy S, Brickley S, Farrant M (2001). NMDA receptor subunits: diversity, development and disease. *Curr Opin Neurobiol*. **11** 327-35.

Dahlhaus R, Hines RM, Eadie BD, Kannangara TS, Hines DJ, Brown CE, Christie BR, El-Husseini A (2010). Overexpression of the cell adhesion protein neuroligin-1 induces learning deficits and impairs synaptic plasticity by altering the ratio of excitation to inhibition in the hippocampus. *Hippocampus* **20**, 305-322.

Dalton GL, Wu DC, Wang YT, Floresco SB, Phillips AG (2012). NMDA GluN2A and GluN2B receptors play separate roles in the induction of LTP and LTD in the amygdala and in the acquisition and extinction of conditioned fear. *Neuropharmacology* **62**, 797-806

Dani VS, Chang Q, Maffei A, Turrigiano GG, Jaenisch R, Nelson SB (2005). Reduced cortical activity due to a shift in the balance between excitation and inhibition in a mouse model of Rett syndrome. *Proc Natl Acad Sci U S A* **102**, 12560-12565.

Dani VS & Nelson SB (2009). Intact long-term potentiation but reduced connectivity between neocortical layer 5 pyramidal neurons in a mouse model of Rett syndrome. *J Neurosci* **29**, 11263-11270.

Das P, Zerda R, Alvarez FJ, Tietz EI (2010). Immunogold electron microscopic evidence of differential regulation of GluN1, GluN2A, and GluN2B, NMDA-type glutamate receptor subunits in rat hippocampal CA1 synapses during benzodiazepine withdrawal. *J Comp Neurol* **518**, 4311-4328.

Demont-Guignard S, Benquet P, Gerber U, Biraben A, Martin B, Wendling F (2012). Distinct hyperexcitability mechanisms underlie fast ripples and epileptic spikes. *Ann Neurol*. **71** 342-352.

Deng P & Xu ZC (2011). Contribution of Ih to neuronal damage in the hippocampus after traumatic brain injury in rats. *J Neurotrauma* **28**, 1173-1183.

Derecki NC, Cronk JC, Kipnis J (2013). The role of microglia in brain maintenance: implications for Rett syndrome. *Trends in immunology* **34**, 144-150

Dorsett D (2007). Roles of the sister chromatid cohesion apparatus in gene expression, development, and human syndromes. *Chromosoma* **116**, 1-13.

Economo MN & White JA (2012). Membrane properties and the balance between excitation and inhibition control gamma-frequency oscillations arising from feedback inhibition. *PLoS Comput Biol.***8**(1) 1-20.

Engert F & Bonhoeffer T (1999). Dendritic spine changes associated with hippocampal long-term synaptic plasticity. *Nature* **399**, 66-70.

Fernandez F & Garner CC (2007). Over-inhibition: a model for developmental intellectual disability. *Trends Neurosci* **30**, 497-503.

Fioravante D & Regehr WG (2011). Short-term forms of presynaptic plasticity. *Curr Opin Neurobiol* **21**, 269-274.

Franks KM, Stevens CF, Sejnowski TJ (2003). Independent sources of quantal variability at single glutamatergic synapses. *J Neurosci* **23**, 3186-3195.

Fuks F, Hurd PJ, Wolf D, Nan X, Bird AP, Kouzarides T (2003). The methyl-CpG-binding protein MeCP2 links DNA methylation to histone methylation. *J Biol Chem* **278**, 4035-4040.

Fukuda T, Itoh M, Ichikawa T, Washiyama K, Goto Y (2005). Delayed maturation of neuronal architecture and synaptogenesis in cerebral cortex of Mecp2-deficient mice. *J Neuropathol Exp Neurol* **64**, 537-544.

Gantz SC, Ford CP, Neve KA, Williams JT (2011). Loss of Mecp2 in substantia nigra dopamine neurons compromises the nigrostriatal pathway. *J Neurosci* **31**, 12629-12637.

Gasparini S & Magee JC (2006). State-dependent dendritic computation in hippocampal CA1 pyramidal neurons. *J Neurosci* **26**, 2088-2100.

Gianakopoulos PJ, Zhang Y, Pencea N, Orlic-Milacic M, Mittal K, Windpassinger C, White SJ, Kroisel PM, Chow EW, Saunders CJ, Minassian BA, Vincent JB (2012). Mutations in MECP2 exon 1 in classical rett patients disrupt MECP2_e1 transcription, but not transcription of MECP2_e2. *Am J Med Genet B Neuropsychiatr Genet* **159B**, 210-216.

Ginhoux F, Greter M, Leboeuf M, Nandi S, See P, Gokhan S, Mehler MF, Conway SJ, Ng LG, E. Stanley R, Samokhvalov IM, Merad M (2010). Fate Mapping Analysis Reveals That Adult Microglia Derive from Primitive Macrophages. *Science* **330**, 841-845.

Gray EE, Fink AE, Sariñana J, Vissel B, O'Dell TJ. (2007) Long-term potentiation in the hippocampal CA1 region does not require insertion and activation of GluR2-lacking AMPA receptors. *J Neurophysiol* **98**, 2488–2492.

Gu N, Vervaeke K, Storm JF (2007). BK potassium channels facilitate high-frequency firing and cause early spike frequency adaptation in rat CA1 hippocampal pyramidal cells. *J Physiol* **580**, 859-882.

Guan T, Qian Y, Tang X, Huang M, Huang L, Li Y, Sun H (2011). Maslinic acid, a natural inhibitor of glycogen phosphorylase, reduces cerebral ischemic injury in hyperglycemic rats by GLT-1 up-regulation. *J Neurosci Res* **89**, 1829-1839.

Gupta S, Kim SY, Artis S, Molfese DL, Schumacher A, Sweatt JD, Paylor RE, Lubin FD (2010). Histone methylation regulates memory formation. *J Neurosci* **30**, 3589-3599.

Guy J, Cheval H, Selfridge J, Bird A (2011). The role of MeCP2 in the brain. *Annu Rev Cell Dev Biol* **27**, 631-652.

Guy J, Gan J, Selfridge J, Cobb S, Bird A (2007). Reversal of neurological defects in a mouse model of Rett syndrome. *Science* **315**, 1143-1147.

Guy J, Hendrich B, Holmes M, Martin JE, Bird A (2001). A mouse Mecp2-null mutation causes neurological symptoms that mimic Rett syndrome. *Nat Genet* **27**, 322-326.

Harris KM, Jensen FE, Tsao B (1992). Three-dimensional structure of dendritic spines and synapses in rat hippocampus (CA1) at postnatal day 15 and adult ages: implications for the maturation of synaptic physiology and long-term potentiation. *J Neurosci* **12**, 2685-2705.

Henle F, Dehmel M, Leemhuis J, Fischer C, Meyer DK (2011). Role of GluN2A and GluN2B subunits in the formation of filopodia and secondary dendrites in cultured hippocampal neurons. *Naunyn Schmiedebergs Arch Pharmacol*.

Hines RM, Wu L, Hines DJ, Steenland H, Mansour S, Dahlhaus R, Singaraja RR, Cao X, Sammler E, Hormuzdi SG, Zhuo M, El-Husseini A (2008). Synaptic imbalance, stereotypies, and impaired social interactions in mice with altered neuroligin 2 expression. *J Neurosci* **28**, 6055-6067.

Hutchinson AN, Deng JV, Aryal DK, Wetsel WC, West AE (2012). Differential Regulation of MeCP2 Phosphorylation in the CNS by Dopamine and Serotonin. *Neuropsychopharmacology* **37**, 321-337.

Ikeda K, Yanagawa Y, Bekkers JM (2008). Distinctive quantal properties of neurotransmission at excitatory and inhibitory autapses revealed using variance-mean analysis. *J Neurosci* **28**, 13563-13573.

Isoda K, Morimoto M, Matsui F, Hasegawa T, Tozawa T, Morioka S, Chiyonobu T, Nishimura A, Yoshimoto K, Hosoi H (2010). Postnatal changes in serotonergic innervation to the hippocampus of methyl-CpG-binding protein 2-null mice. *Neuroscience* **165**, 1254-1260.

Itoh M, Ide S, Takashima S, Kudo S, Nomura Y, Segawa M, Kubota T, Mori H, Tanaka S, Horie H, Tanabe Y, Goto Y (2007). Methyl CpG-binding protein 2 (a mutation of which causes Rett syndrome) directly regulates insulin-like growth factor binding protein 3 in mouse and human brains. *J Neuropathol Exp Neurol* **66**, 117-123.

Jian L, Nagarajan L, de Klerk N, Ravine D, Bower C, Anderson A, Williamson S, Christodoulou J, Leonard H (2006). Predictors of seizure onset in Rett syndrome. J Pediatr. **149**(4), 542-547.

Jinno S (2011). Regional and laminar differences in antigen profiles and spatial distributions of astrocytes in the mouse hippocampus, with reference to aging. *Neuroscience* **180**, 41-52.

Jones PL, Veenstra GJ, Wade PA, Vermaak D, Kass SU, Landsberger N, Strouboulis J, Wolffe AP (1998). Methylated DNA and MeCP2 recruit histone deacetylase to repress transcription. *Nat Genet* **19**, 187-191.

Jurado S, Goswami D, Zhang Y, Molina AJ, Südhof TC, Malenka RC. (2013). LTP Requires a Unique Postsynaptic SNARE Fusion Machinery. *Neuron* **77**, 542-58.

Kaczorowski CC, Disterhoft J, Spruston N (2007). Stability and plasticity of intrinsic membrane properties in hippocampal CA1 pyramidal neurons: effects of internal anions. *J Physiol* **578**, 799-818.

Katz Y, Menon V, Nicholson DA, Geinisman Y, Kath WL, Spruston N (2009). Synapse distribution suggests a two-stage model of dendritic integration in CA1 pyramidal neurons. *Neuron* **63**, 171-177.

Kerr B, Soto CJ, Saez M, Abrams A, Walz K, Young JI (2012). Transgenic complementation of MeCP2 deficiency: phenotypic rescue of Mecp2-null mice by isoform-specific transgenes. *Eur J Hum Genet* **20**, 69-76.

Kifayathullah LA, Arunachalam JP, Bodda C, Agbemenyah HY, Laccone FA, Mannan AU (2010). MeCP2 mutant protein is expressed in astrocytes as well as in neurons and localizes in the nucleus. *Cytogenet Genome Res* **129**, 290-297.

Kishi N & Macklis JD (2004). MECP2 is progressively expressed in post-migratory neurons and is involved in neuronal maturation rather than cell fate decisions. *Mol Cell Neurosci* **27**, 306-321.

Kishi N & Macklis JD (2010). MeCP2 functions largely cell-autonomously, but also non-cell-autonomously, in neuronal maturation and dendritic arborization of cortical pyramidal neurons. *Exp Neurol* **222**, 51-58.

Klemmer P, Meredith RM, Holmgren CD, Klychnikov OI, Stahl-Zeng J, Loos M, van der Schors RC, Wortel J, de WH, Spijker S, Rotaru DC, Mansvelder HD, Smit AB, Li KW (2011). Proteomics, ultrastructure, and physiology of hippocampal synapses in a fragile X syndrome mouse model reveal presynaptic phenotype. *J Biol Chem* **286**, 25495-25504.

Kline DD, Ogier M, Kunze DL, Katz DM (2010). Exogenous brain-derived neurotrophic factor rescues synaptic dysfunction in Mecp2-null mice. *J Neurosci* **30**, 5303-5310.

Konur S, Rabinowitz D, Fenstermaker VL, Yuste R (2003). Systematic regulation of spine sizes and densities in pyramidal neurons. *J Neurobiol* **56**, 95-112.

Kumar A, Thinschmidt JS, Foster TC, King MA (2007). Aging effects on the limits and stability of long-term synaptic potentiation and depression in rat hippocampal area CA1. *J Neurophysiol*. **98**, 594-601.

Lee S, Kim W, Ham BJ, Chen W, Bear MF, Yoon BJ (2008). Activity-dependent NR2B expression is mediated by MeCP2-dependent epigenetic regulation. *Biochem Biophys Res Commun* **377**, 930-934.

Lewis DA, Curley AA, Glausier JR, Volk DW (2012). Cortical parvalbumin interneurons and cognitive dysfunction in schizophrenia. *Trends Neurosci* **35**, 57-67.

Lewis JD, Meehan RR, Henzel WJ, Maurer-Fogy I, Jeppesen P, Klein F, Bird A (1992). Purification, sequence, and cellular localization of a novel chromosomal protein that binds to methylated DNA. *Cell* **69**, 905-914.

Li H, Zhong X, Chau KF, Williams EC, Chang Q (2011a). Loss of activity-induced phosphorylation of MeCP2 enhances synaptogenesis, LTP and spatial memory. *Nat Neurosci* **14**, 1001-1008.

Li HB, Jackson MF, Yang K, Trepanier C, Salter MW, Orser BA, Macdonald JF (2011b). Plasticity of synaptic GluN receptors is required for the Src-dependent induction of long-term potentiation at CA3-CA1 synapses. *Hippocampus* **21**, 1053-1061.

Li WC, Soffe SR, Roberts A (2004). A direct comparison of whole cell patch and sharp electrodes by simultaneous recording from single spinal neurons in frog tadpoles. *J Neurophysiol* **92**, 380-386.

Lintas C, Sacco R, Persico AM (2012). Genome-wide expression studies in Autism spectrum disorder, Rett syndrome, and Down syndrome. *Neurobiol Dis* **45**, 57-68.

Lioy DT, Garg SK, Monaghan CE, Raber J, Foust KD, Kaspar BK, Hirrlinger PG, Kirchhoff F, Bissonnette JM, Ballas N, Mandel G (2011). A role for glia in the progression of Rett's syndrome. *Nature* **475**, 497-500.

Liu J & Krantz ID (2009). Cornelia de Lange syndrome, cohesin, and beyond. *Clin Genet* **76**, 303-314.

Lopantsev V, Both M, Draguhn A (2009). Rapid plasticity at inhibitory and excitatory synapses in the hippocampus induced by ictal epileptiform discharges. *Eur J Neurosci* **29**, 1153-1164.

Maccaferri G (2011). Microcircuit-specific processing in the hippocampus. *J Physiol* **589**, 1873-1874.

Maccaferri G, Mangoni M, Lazzari A, DiFrancesco D (1993). Properties of the hyperpolarization-activated current in rat hippocampal CA1 pyramidal cells. *J Neurophysiol* **69**, 2129-2136.

Maccaferri G & McBain CJ (1995). Passive propagation of LTD to stratum oriens-alveus inhibitory neurons modulates the temporoammonic input to the hippocampal CA1 region. *Neuron* **15**, 137-145.

Maezawa I & Jin LW (2010). Rett syndrome microglia damage dendrites and synapses by the elevated release of glutamate. *J Neurosci* **30**, 5346-5356.

Maezawa I, Swanberg S, Harvey D, Lasalle JM, Jin LW (2009). Rett syndrome astrocytes are abnormal and spread MeCP2 deficiency through gap junctions. *J Neurosci* **29**, 5051-5061.

Maliszewska-Cyna E, Bawa D, Eubanks JH (2010). Diminished prevalence but preserved synaptic distribution of N-methyl-D-aspartate receptor subunits in the methyl CpG binding protein 2(MeCP2)-null mouse brain. *Neuroscience* **168**, 624-632.

Marchetto MC, Carromeu C, Acab A, Yu D, Yeo GW, Mu Y, Chen G, Gage FH, Muotri AR (2010). A model for neural development and treatment of Rett syndrome using human induced pluripotent stem cells. *Cell* **143**, 527-539.

Markham JA, McKian KP, Stroup TS, Juraska JM (2005). Sexually dimorphic aging of dendritic morphology in CA1 of hippocampus. *Hippocampus* **15**, 97-103.

Martinowich K, Hattori D, Wu H, Fouse S, He F, Hu Y, Fan G, Sun YE (2003). DNA methylation-related chromatin remodeling in activity-dependent BDNF gene regulation. *Science* **302**, 890-893.

Matthews EA, Linardakis JM, Disterhoft JF (2009). The fast and slow afterhyperpolarizations are differentially modulated in hippocampal neurons by aging and learning. *J Neurosci* **29**, 4750-4755.

McGraw CM, Samaco RC, Zoghbi HY (2011). Adult neural function requires MeCP2. *Science* **333**, 186.

McLeod F, Ganley R, Williams L, Selfridge J, Bird A, Cobb S R (2013). Reduced seizure threshold and altered network oscillatory properties in a mouse model of Rett syndrome. *Neuroscience* **231**, 195-205.

Medrihan L, Tantalaki E, Aramuni G, Sargsyan V, Dudanova I, Missler M, Zhang W (2008). Early defects of GABAergic synapses in the brain stem of a MeCP2 mouse model of Rett syndrome. *J Neurophysiol* **99**, 112-121.

Meehan RR, Lewis JD, Bird AP (1992). Characterization of MeCP2, a vertebrate DNA binding protein with affinity for methylated DNA. *Nucleic Acids Res* **20**, 5085-5092.

Megias M, Emri Z, Freund TF, Gulyas AI (2001). Total number and distribution of inhibitory and excitatory synapses on hippocampal CA1 pyramidal cells. *Neuroscience* **102**, 527-540.

Mehler MF & Purpura DP (2009). Autism, fever, epigenetics and the locus coeruleus. *Brain Res Rev* **59**, 388-392.

Meredith RM, Floyer-Lea AM, Paulsen O. (2003). Maturation of long-term potentiation induction rules in rodent hippocampus: role of GABAergic inhibition. *J Neurosci* **35**, 11142-11146

Metcalf BM, Mullaney BC, Johnston MV, Blue ME (2006). Temporal shift in methyl-CpG binding protein 2 expression in a mouse model of Rett syndrome. *Neuroscience* **139**, 1449-1460.

Minkeviciene R, Banerjee P, Tanila H (2004). Memantine improves spatial learning in a transgenic mouse model of Alzheimer's disease. *J Pharmacol Exp Ther* **311**, 677-682.

Minkeviciene R, Banerjee P, Tanila H (2008). Cognition-enhancing and anxiolytic effects of memantine. *Neuropharmacology* **54**, 1079-1085.

Mizuseki K, Diba K, Pastalkova E, Buzsaki G (2011). Hippocampal CA1 pyramidal cells form functionally distinct sublayers. *Nat Neurosci* **14**, 1174-1181.

Mochida S, Few AP, Scheuer T, Catterall WA (2008). Regulation of presynaptic Ca(V)2.1 channels by Ca2+ sensor proteins mediates short-term synaptic plasticity. *Neuron* **57**, 210-216.

Moore SJ, Throesch BT, Murphy GG (2011). Of mice and intrinsic excitability: genetic background affects the size of the postburst afterhyperpolarization in CA1 pyramidal neurons. *J Neurophysiol* **106**, 1570-1580.

Moretti P, Levenson JM, Battaglia F, Atkinson R, Teague R, Antalffy B, Armstrong D, Arancio O, Sweatt JD, Zoghbi HY (2006). Learning and memory and synaptic plasticity are impaired in a mouse model of Rett syndrome. *J Neurosci* **26**, 319-327.

Mori-Kawakami F, Kobayashi K, Takahashi T (2003). Developmental decrease in synaptic facilitation at the mouse hippocampal mossy fibre synapse. *J Physiol* **553**, 37-48.

Müller L, Tokay T, Porath K, Köhling R, Kirschstein T (2013) Enhanced NMDA receptor-dependent LTP in the epileptic CA1 area via upregulation of NR2B. *Neurobiol Dis* [Epub ahead of print]

Na ES, Nelson ED, Adachi M, Autry AE, Mahgoub MA, Kavalali ET Monteggia LM. (2012). A mouse model for MeCP2 duplication syndrome: MeCP2 overexpression impairs learning and memory and synaptic transmission. J Neurosci. **32,** 3109-17

Nakamura NH & McEwen BS (2005). Changes in interneuronal phenotypes regulated by estradiol in the adult rat hippocampus: a potential role for neuropeptide Y. *Neuroscience* **136**, 357-369.

Naylor DE (2010). Glutamate and GABA in the balance: convergent pathways sustain seizures during status epilepticus. *Epilepsia* **51 (**Suppl 3), 106-109.

Neher, E & Sakmann, B (1992). The Patch Clamp Technique. *Sci Am* **266**, 44-51.

Nelson ED, Bal M, Kavalali ET, Monteggia LM (2011). Selective impact of MeCP2 and associated histone deacetylases on the dynamics of evoked excitatory neurotransmission. *J Neurophysiol* **106**, 193-201.

Nelson ED, Kavalali ET, Monteggia LM (2006). MeCP2-dependent transcriptional repression regulates excitatory neurotransmission. *Curr Biol* **16**, 710-716.

Neul JL, Kaufmann WE, Glaze DG, Christodoulou J, Clarke AJ, Bahi-Buisson N, Leonard H, Bailey ME, Schanen NC, Zappella M, Renieri A, Huppke P, Percy AK (2010). Rett syndrome: revised diagnostic criteria and nomenclature. *Ann Neurol* **68**, 944-950.

Nguyen MVC, Du F, Felice CA, Shan X, Nigam A, Mandel G, Robinson JK , Ballas N (2012). MeCP2 Is Critical for Maintaining Mature Neuronal Networks and Global Brain Anatomy during Late Stages of Postnatal Brain Development and in the Mature Adult Brain. *J Neurosci* **32**, 10021-10034.

Nicholson DA, Trana R, Katz Y, Kath WL, Spruston N, Geinisman Y (2006). Distance-dependent differences in synapse number and AMPA receptor expression in hippocampal CA1 pyramidal neurons. *Neuron* **50**, 431-442.

Nikitina T, Ghosh RP, Horowitz-Scherer RA, Hansen JC, Grigoryev SA, Woodcock CL (2007). MeCP2-chromatin interactions include the formation of chromatosome-like structures and are altered in mutations causing Rett syndrome. *J Biol Chem* **282**, 28237-28245.

Nyakas C, Granic I, Halmy LG, Banerjee P, Luiten PG (2011). The basal forebrain cholinergic system in aging and dementia. Rescuing cholinergic neurons from neurotoxic amyloid-beta42 with memantine. *Behav Brain Res* **221**, 594-603.

Paoletti P, Neyton J (2007). NMDA receptor subunits: function and pharmacology. *Curr Opin Pharmacol* **7**, 39-47

Parsons CG, Stoffler A, Danysz W (2007). Memantine: a NMDA receptor antagonist that improves memory by restoration of homeostasis in the glutamatergic system--too little activation is bad, too much is even worse. *Neuropharmacology* **53**, 699-723.

Pavlov I, Scimemi A, Savtchenko L, Kullmann DM, Walker MC (2011). I(h)-mediated depolarization enhances the temporal precision of neuronal integration. *Nat Commun* **2**, 199.

Peng BW, Justice JA, Zhang K, Li JX, He XH, Sanchez RM (2011). Gabapentin promotes inhibition by enhancing hyperpolarization-activated cation currents and spontaneous firing in hippocampal CA1 interneurons. *Neurosci Lett* **494**, 19-23.

Piskorowski RA & Chevaleyre V (2012). Synaptic integration by different dendritic compartments of hippocampal CA1 and CA2 pyramidal neurons. *Cell Mol Life Sci* **69**, 75-88.

Platkiewicz J & Brette R (2010). A threshold equation for action potential initiation. *PLoS Comput Biol*, 6(7): e1000850. doi:10.1371/journal.pcbi.1000850

Platkiewicz J & Brette R (2011). Impact of fast sodium channel inactivation on spike threshold dynamics and synaptic integration. *PLoS Comput Biol*, 7(5): e1001129. doi:10.1371/journal.pcbi.1001129

Psoni S, Sofocleous C, Traeger-Synodinos J, Kitsiou-Tzeli S, Kanavakis E, Fryssira-Kanioura H (2011). MECP2 mutations and clinical correlations in Greek children with Rett syndrome and associated neurodevelopmental disorders. *Brain Dev.* **34,** 487-495

Qian Y, Guan T, Tang X, Huang L, Huang M, Li Y, Sun H, Yu R, Zhang F (2011). Astrocytic glutamate transporter-dependent neuroprotection against glutamate toxicity: an in vitro study of maslinic acid. *Eur J Pharmacol* **651**, 59-65.

Qiu Z & Cheng J (2010). The role of calcium-dependent gene expression in autism spectrum disorders: lessons from MeCP2, Ube3a and beyond. *Neurosignals* **18**, 72-81.

Raizis AM, Saleem M, MacKay R, George PM (2009). Spectrum of MECP2 mutations in New Zealand Rett syndrome patients. *N Z Med J* **122**, 21-28.

Rammes G, Rupprecht R, Ferrari U, Zieglgansberger W, Parsons CG (2001). The N-methyl-D-aspartate receptor channel blockers memantine, MRZ 2/579 and other amino-alkyl-cyclohexanes antagonise 5-HT(3) receptor currents in cultured HEK-293 and N1E-115 cell systems in a non-competitive manner. *Neurosci Lett* **306**, 81-84.

Ramocki MB, Tavyev YJ, Peters SU (2010). The MECP2 duplication syndrome. *Am J Med Genet A* **152A**, 1079-1088.

Remy S, Csicsvari J, Beck H (2009). Activity-dependent control of neuronal output by local and global dendritic spike attenuation. *Neuron* **61**, 906-916.

Richwine AF, Parkin AO, Buchanan JB, Chen J, Markham JA, Juraska JM, Johnson RW (2008). Architectural changes to CA1 pyramidal neurons in adult and aged mice after peripheral immune stimulation. *Psychoneuroendocrinology* **33**, 1369-1377.

Robinson L, Guy J, McKay L, Brockett E, Spike RC, Selfridge J, De Sousa D, Merusi C, Riedel G, Bird A, Cobb SR. (2012) Morphological and functional reversal of phenotypes in a mouse model of Rett syndrome. *Brain* **135,** 2699-2710

Rotman Z, Deng PY, Klyachko VA (2011). Short-term plasticity optimizes synaptic information transmission. *J Neurosci* **31**, 14800-14809.

Routh BN, Johnston D, Harris K, Chitwood RA (2009). Anatomical and electrophysiological comparison of CA1 pyramidal neurons of the rat and mouse. *J Neurophysiol* **102**, 2288-2302.

Roux JC, Panayotis N, Dura E, Villard L (2010). Progressive noradrenergic deficits in the locus coeruleus of Mecp2 deficient mice. *J Neurosci Res* **88**, 1500-1509.

Sah P & Bekkers JM (1996). Apical dendritic location of slow afterhyperpolarization current in hippocampal pyramidal neurons: implications for the integration of long-term potentiation. *J Neurosci* **16**, 4537-4542.

Samaco RC, Mandel-Brehm C, Chao HT, Ward CS, Fyffe-Maricich SL, Ren J, Hyland K, Thaller C, Maricich SM, Humphreys P, Greer JJ, Percy A, Glaze DG, Zoghbi HY, Neul JL (2009). Loss of MeCP2 in aminergic neurons causes cell-autonomous defects in neurotransmitter synthesis and specific behavioral abnormalities. *Proc Natl Acad Sci U S A* **106**, 21966-21971.

Santos M, Summavielle T, Teixeira-Castro A, Silva-Fernandes A, Duarte-Silva S, Marques F, Martins L, Dierssen M, Oliveira P, Sousa N, Maciel P (2010). Monoamine deficits in the brain of methyl-CpG binding protein 2 null mice suggest the involvement of the cerebral cortex in early stages of Rett syndrome. *Neuroscience* **170**, 453-467.

Sargent PB, Saviane C, Nielsen TA, DiGregorio DA, Silver RA (2005). Rapid vesicular release, quantal variability, and spillover contribute to the precision and reliability of transmission at a glomerular synapse. *J Neurosci* **25**, 8173-8187.

Saunders CJ, Minassian BE, Chow EW, Zhao W, Vincent JB (2009). Novel exon 1 mutations in MECP2 implicate isoform MeCP2_e1 in classical Rett syndrome. *Am J Med Genet Part A* **149A**, 1019-1023.

Scharfman HE (2007). The CA3 "backprojection" to the dentate gyrus. *Prog Brain Res* **163**, 627-637.

Schulz R, Kirschstein T, Brehme H, Porath K, Mikkat U, Kohling R (2012). Network excitability in a model of chronic temporal lobe epilepsy critically depends on SK channel-mediated AHP currents. *Neurobiol Dis* **45**, 337-347.

Seeman P, Caruso C, Lasaga M (2008). Memantine agonist action at dopamine D2High receptors. *Synapse* **62**, 149-153.

Sekerli M, Del Negro CA, Lee RH, Butera RJ (2004). Estimating action potential thresholds from neuronal time-series: new metrics and evaluation of methodologies. *IEEE Trans Biomed Eng* **51**, 1665-1672.

Shahbazian M, Young J, Yuva-Paylor L, Spencer C, Antalffy B, Noebels J, Armstrong D, Paylor R, Zoghbi H (2002a). Mice with truncated MeCP2 recapitulate many Rett syndrome features and display hyperacetylation of histone H3. *Neuron* **35**, 243-254.

Shahbazian MD, Antalffy B, Armstrong DL, Zoghbi HY (2002b). Insight into Rett syndrome: MeCP2 levels display tissue- and cell-specific differences and correlate with neuronal maturation. *Hum Mol Genet* **11**, 115-124.

Shelbourne P, Coote E, Dadak S, Cobb SR. (2007). Normal electrical properties of hippocampal neurons modelling early Huntington disease pathogenesis. *Brain Res.***1139**, 226-234

Singleton MK, Gonzales ML, Leung KN, Yasui DH, Schroeder DI, Dunaway K, Lasalle JM (2011). MeCP2 is required for global heterochromatic and nucleolar changes during activity-dependent neuronal maturation. *Neurobiol Dis* **43**, 190-200.

Skene PJ, Illingworth RS, Webb S, Kerr AR, James KD, Turner DJ, Andrews R, Bird AP (2010). Neuronal MeCP2 is expressed at near histone-octamer levels and globally alters the chromatin state. *Mol Cell* **37**, 457-468.

Smrt RD, Pfeiffer RL, Zhao X (2011). Age-dependent expression of MeCP2 in a heterozygous mosaic mouse model. *Hum Mol Genet* **20**, 1834-1843.

Sorra KE & Harris KM (1993). Occurrence and three-dimensional structure of multiple synapses between individual radiatum axons and their target pyramidal cells in hippocampal area CA1. *J Neurosci* **13**, 3736-3748.

Spruston N (2008). Pyramidal neurons: dendritic structure and synaptic integration. *Nat Rev Neurosci* **9**, 206-221.

Staff NP, Jung HY, Thiagarajan T, Yao M, Spruston N (2000). Resting and active properties of pyramidal neurons in subiculum and CA1 of rat hippocampus. *J Neurophysiol* **84**, 2398-2408.

Storm JF (1987). Action potential repolarization and a fast after-hyperpolarization in rat hippocampal pyramidal cells. *J Physiol* **385**, 733-759.

Stricker C, Field AC, Redman SJ (1996). Changes in quantal parameters of EPSCs in rat CA1 neurones in vitro after the induction of long-term potentiation. *J Physiol* **490** (Pt 2), 443-454.

Stuart GJ, Dodt H-U, Sackmann B (1993). Patch-clamp recordings from the soma and dendrites of neurons in brain slices using infrared video microscopy. *Pflugers Arch.* **423**, 511-8.

Sun HY, Lyons SA, Dobrunz LE (2005). Mechanisms of target-cell specific short-term plasticity at Schaffer collateral synapses onto interneurones versus pyramidal cells in juvenile rats. *J Physiol* **568**, 815-840.

Swann JW, Le JT, Lee CL (2007). Recurrent Seizures and the Molecular Maturation of Hippocampal and Neocortical Glutamatergic Synapses. *Dev Neurosci* **29**, 168-178.

Szilagyi T, Orban-Kis K, Horvath E, Metz J, Pap Z, Pavai Z (2011). Morphological identification of neuron types in the rat hippocampus. *Rom J Morphol Embryol* **52**, 15-20.

Taneja P, Ogier M, Brooks-Harris G, Schmid DA, Katz DM, Nelson SB (2009). Pathophysiology of locus ceruleus neurons in a mouse model of Rett syndrome. *J Neurosci* **29**, 12187-12195.

Tao J, Hu K, Chang Q, Wu H, Sherman NE, Martinowich K, Klose RJ, Schanen C, Jaenisch R, Wang W, Sun YE (2009). Phosphorylation of MeCP2 at Serine 80 regulates its chromatin association and neurological function. *Proc Natl Acad Sci USA* **106**, 4882-4887.

Tombaugh GC, Rowe WB, Rose GM (2005). The slow afterhyperpolarization in hippocampal CA1 neurons covaries with spatial learning ability in aged Fisher 344 rats. *J Neurosci* **25**, 2609-2616.

Tyzio R, Ivanov A, Bernard C, Holmes GL, Ben-Ari Y, Khazipov R (2003). Membrane potential of CA3 hippocampal pyramidal cells during postnatal development. *J Neurophysiol* **90**, 2964-2972.

Van Esch, H (2012) MECP2 Duplication Syndrome. *Mol Syndromol* **2,** 128-136

Viemari JC, Roux JC, Tryba AK, Saywell V, Burnet H, Peña F, Zanella S, Bévengut M, Barthelemy-Requin M, Herzing LB, Moncla A, Mancini J, Ramirez JM, Villard L, Hilaire G. 2005) Mecp2 deficiency disrupts norepinephrine and respiratory systems in mice. *J Neurosci*. **25** 11521-11530

Vilain A, Apiou F, Vogt N, Dutrillaux B, Malfoy B (1996). Assignment of the gene for methyl-CpG-binding protein 2 (MECP2) to human chromosome band Xq28 by in situ hybridization. *Cytogenet Cell Genet* **74**, 293-294.

Volianskis A, Bannister N, Collett VJ, Irvine MW, Monaghan DT, Fitzjohn SM, Jensen MS, Jane DE, Collingridge GL (2013). Different NMDA receptor subtypes mediate induction of long-term potentiation and two forms of short-term potentiation at CA1 synapses in rat hippocampus in vitro. *J Physiol* **591**, 955-972

Waters J & Helmchen F (2006). Background synaptic activity is sparse in neocortex. *J Neurosci* **26**, 8267-8277.

Watson CM, Pelka GJ, Radziewic T, Shahbazian MD, Christodoulou J, Williamson SL, Tam PP (2005). Reduced proportion of Purkinje cells expressing paternally derived mutant Mecp2308 allele in female mouse cerebellum is not due to a skewed primary pattern of X-chromosome inactivation. *Hum Mol Genet* **14**, 1851-1861.

Weng SM, McLeod F, Bailey ME, Cobb SR (2011). Synaptic plasticity deficits in an experimental model of rett syndrome: long-term potentiation saturation and its pharmacological reversal. *Neuroscience* **180**, 314-321.

Wood L, Gray NW, Zhou Z, Greenberg ME, Shepherd GM (2009). Synaptic circuit abnormalities of motor-frontal layer 2/3 pyramidal neurons in an RNA interference model of methyl-CpG-binding protein 2 deficiency. *J Neurosci* **29**, 12440-12448.

Wood L & Shepherd GM (2010). Synaptic circuit abnormalities of motor-frontal layer 2/3 pyramidal neurons in a mutant mouse model of Rett syndrome. *Neurobiol Dis* **38**, 281-287.

Xu C, Cui C, Alkon DL (2009). Age-dependent enhancement of inhibitory synaptic transmission in CA1 pyramidal neurons via GluR5 kainate receptors. *Hippocampus* **19**, 706-717.

Yizhar O, Fenno LE, Prigge M, Schneider F, Davidson TJ, O'Shea DJ, Sohal VS, Goshen I, Finkelstein J, Paz JT, Stehfest K, Fudim R, Ramakrishnan C, Huguenard JR, Hegemann P, Deisseroth K (2011). Neocortical excitation/inhibition balance in information processing and social dysfunction. *Nature* **477**, 171-178.

Young JI & Zoghbi HY (2004). X-chromosome inactivation patterns are unbalanced and affect the phenotypic outcome in a mouse model of rett syndrome. *Am J Hum Genet* **74**, 511-520.

Zaniboni M, Cacciani F, Groppi M (2005). Effect of input resistance voltage-dependency on DC estimate of membrane capacitance in cardiac myocytes. *Biophys J* **89**, 2170-2181.

Zhang L, He J, Jugloff DG, Eubanks JH (2008). The MeCP2-null mouse hippocampus displays altered basal inhibitory rhythms and is prone to hyperexcitability. *Hippocampus* **18**, 294-309.

Zhang X, Cui N, Wu Z, Su J, Tadepalli JS, Sekizar S, Jiang C (2010a). Intrinsic membrane properties of locus coeruleus neurons in Mecp2-null mice. *Am J Physiol Cell Physiol* **298**, C635-C646.

Zhang ZW, Zak JD, Liu H (2010b). MeCP2 is required for normal development of GABAergic circuits in the thalamus. *J Neurophysiol* **103**, 2470-2481.

Zhou Z, Hong EJ, Cohen S, Zhao WN, Ho HY, Schmidt L, Chen WG, Lin Y, Savner E, Griffith EC, Hu L, Steen JA, Weitz CJ, Greenberg ME (2006). Brain-specific phosphorylation of MeCP2 regulates activity-dependent Bdnf transcription, dendritic growth, and spine maturation. *Neuron* **52**, 255-269.

Zucker RS & Regehr WG (2002). Short-term synaptic plasticity. *Annu Rev Physiol* **64**, 355-405.